Atom Preparation and Rydberg Excitation of Rubidium Atoms

Julia Gamper

Masterarbeit in Physik
angefertigt im Institut für Angewandte Physik

vorgelegt der
Mathematisch-Naturwissenschaftlichen Fakultät
der
Rheinischen Friedrich-Wilhelms-Universität
Bonn

Oktober 2024

I hereby declare that this thesis was formulated by myself and that no sources or tools other than those cited were used.

Bonn, 25.10.2024
Date

Julia Sanz
Signature

1. Supervisor: Prof. Dr. Sebastian Hofferberth
2. Supervisor: Prof. Dr. Daqing Wang

Contents

CHAPTER 1

Introduction

The field of quantum technology has advanced rapidly in recent years [1], with the promise to solve problems beyond the capabilities of classical computers in the fields of optimization problems [2], machine learning [3] and cryptography [4, 5], among others [6]. Quantum computing is an integral part of quantum technology and has gained significant attention [1, 7]. Many different platforms for quantum computing are actively being researched, for example superconducting qubits [8] and Rydberg atoms [9, 10], having different advantages [11, 12].

Recently, hybrid systems that combine different quantum platforms [13, 14], designed to benefit from both their respective advantages, have emerged [6, 15]. Hybrid systems are a promising candidate for different applications, including quantum information transfer because they typically operate across different frequency regimes [6]. Microwave-to-optical platforms in particular are a favourable approach for interconnecting quantum platforms [16, 17] as most long distance information transfer relies on optical frequencies [18, 19] and one of the leading platforms for quantum computing, namely superconducting qubits [8], operate in the microwave regime [11]. Superconducting qubits exhibit fast high-fidelity gate operations [14, 20], tunable coupling of qubits [21] and strong coupling to external fields [20].

One way of bridging the microwave and optical frequency range is using Rydberg states of ultracold atoms because of their electric dipole transitions over a large range of the electromagnetic spectrum [10, 22]. Couplings between the ground state and the Rydberg state can be done with optical photons [23], whereas Rydberg-Rydberg transitions are in the microwave regime [23, 24]. To couple ultracold Rydberg atoms and superconducting qubits, a mediator is necessary [20, 25]. Electromechanical oscillators can enable such a coupling between the two platforms [20]. A hybrid system combining Rydberg atoms and an electromechanical oscillator would allow utilizing both the fast high-fidelity gate operations from super conducting qubits [14, 20] and the large scalability [26, 27], long coherence times [23] and optical control and read-out [28] via the Rydberg atom platform. Electromechanical oscillators also serve as a promising choice for quantum memory [29], due to their long coherence times [14], high achievable quality factors [30] and the potential scalability given by their small size [20].

The Hybrid Quantum Optics experiment in the Nonlinear Quantum Optics group of Sebastian Hofferberth aims to interface Rydberg atoms with a high quality factor electromechanical oscillator on an atom chip. To minimize thermal occupation before performing the coherent exchange of microwave photons [30], the experiment will be conducted in a closed-cycle cryostat. The experiment was

approached from two sides - the electromechanical oscillator on an atom chip and the cold atom preparation together with excitation and detection of Rydberg atoms. With the first generation chip being designed and fabricated [31], two-photon Rydberg excitation of Rubidium has to be implemented, which is the goal of this thesis. At the time of this thesis, the cryostat was not yet part of the setup. However, the implementation of Rydberg excitation was conducted while keeping the requirements of the cryostat in mind.

The thesis is structured as follows. In Chapter 2 the two chamber setup of the experiment is presented and the laser system needed for cold atom preparation and Rydberg excitation is introduced. To be able to perform Rydberg excitation, the Rubidium atoms must be prepared and transported to the region where the experiment is conducted. As a two chamber design was chosen, multiple preparation steps need to be taken. In Chapter 3 the experimental sequence used for preparing the Rubidium atoms as well as the optimization of cold atom preparation is described. Afterwards, Rydberg excitation and detection is covered in Chapter 4. For this, the implementation of Rydberg excitation is introduced in detail. Additionally, two detection schemes are discussed. Few photon transmission spectroscopy is set up and characterized, which makes it possible to characterize the atom cloud and perform measurements in Electromagnetically Induced Transparency conditions with Rydberg atoms [32, 33] and therefore enables optical readout. One further detection scheme, that is implemented, is the ionization of Rydberg atoms and the subsequent detection of the ions. This provides information about the number of remaining Rydberg atoms after conducting an experiment. Chapter 5 concludes the thesis with an outlook on the next steps of optimization on the side of ultracold Rydberg atoms.

CHAPTER 2

Hybrid quantum optics experiment

In the Hybrid Quantum Optics (HQO) experiment we plan to interface Rydberg atoms with an electromechanical oscillator to cool one vibrational mode of the latter to its quantum mechanical ground state.

Rydberg atoms are atoms which are excited to a high principal quantum number n. Besides being a great candidate for hybrid systems, which we will take advantage of in this experiment, Rydberg atoms have a variety of features with are used in many fields e.g. quantum computing [9, 10]. Due to their high principal quantum number n, large coherence times [23] and interactions over a longe distances due to their large dipole moments [23] are possible. This will enable interactions with an electromechanical oscillator at distances of in the order of 10 µm.

While the experiment needs to be tackled from both sides - the atom chip with the electromechanical oscillator and the Rydberg atoms - my focus will be on the latter. This includes the cold atom preparation to make it possible for the atoms to eventually conduct the experiment with the prepared atoms at the wanted position. In addition, the Rydberg excitation as well as the detection has to be implemented. In our experiment, we aim for a Rydberg state of $n = 68$ or $n = 86$. This is the case since the first generation chip, that was designed by Leon Sadowski, has a resonator whose frequency matches the 68S $\rightarrow$ 68P transition [31]. A higher harmonic mode of the resonator would then coincide with 86S $\rightarrow$ 86P.

The experimental setup needed to conduct the creation of Rydberg atoms will be explained in more detail in this chapter.

First, I will introduce the experimental setup needed to enable the Rydberg atom side of the experiment in Section 2.1, especially talking about individual design decisions. Subsequently, the laser locking scheme and the use of the individual lasers are briefly explained in Section 2.2 as they are a crucial component for making the experiment possible. Finally, I will introduce the computer control sequence in Section 2.3 as it is an important tool to perform individual measurements which were conducted as part of this thesis.

2.1 Experimental setup

In this section, I will give an overview of the experimental setup used to enable the interaction of Rydberg atoms with an electromechanical oscillator in a cryostat.

In order to make it possible to cool one oscillation mode of the oscillator to its quantum mechanical ground state, some requirements have to be met.

- A cryogenic environment at 4 K is needed to make sure one has a small phonon number to start with because only then it is possible to cool one vibrational mode of the electromechanical oscillator to the ground state.
- The vacuum needs to be good enough for the lifetime of the atoms being sufficient for the interaction to take place.
- The atoms need to be prepared close to the chip region and excited to the Rydberg state.

In Fig. 2.1 one can see a CAD file of the whole experimental setup which meets the requirements mentioned above. Here, the system is divided into two parts. The purple part is the setup where the experiment is conducted which will be described in more detail in the following and in blue one can see the cryostat which is needed to achieve the temperature of 4 K which is required in the experiment. With this being set up, the first requirement is met.

In this experiment, a two-chamber design was chosen because the atom preparation, which requires high laser power, should be as far away from the cryostat as possible to ensure that it does not heat up

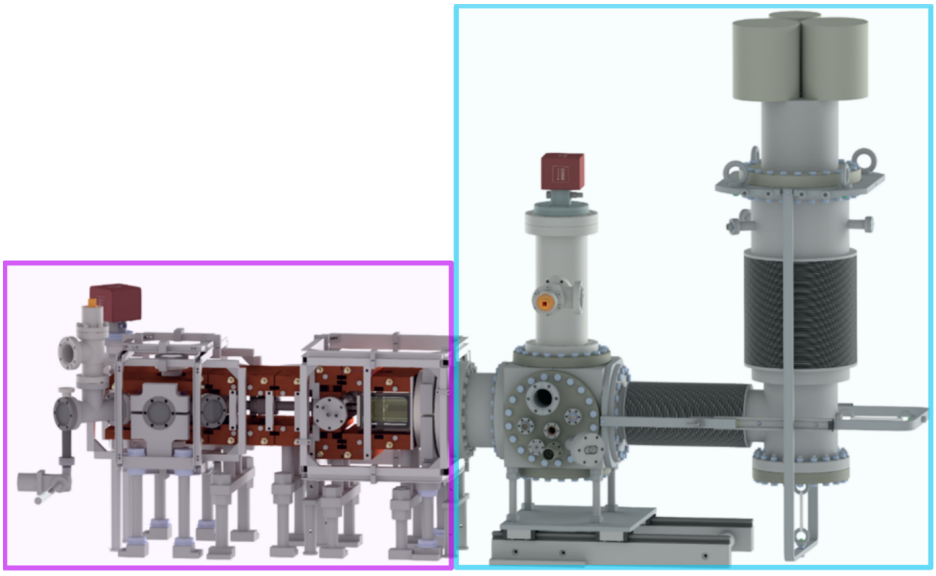

Figure 2.1: CAD picture of the complete experimental setup used in the HQO experiment. The left hand side (marked in purple) is the setup used for cold atom preparation and Rydberg excitation and is already set up in the experiment. The right hand side (marked in blue) is a drawing of the closed-cycle cryostat which will be included into the setup in the future enabling experiments at cryogenic temperatures. For now, only the left side of the setup is set up but all decisions on the experiment are made such that it is compatible with the future cryogenic setup.

the cryogenic region. There is also another advantage to having two chambers, which is the ability to have different pressures in each chamber. By using a differential pump tube, it is possible to achieve a much better vacuum in the Science chamber (chamber at cryogenic temperatures where the experiment is conducted) than in the magneto optical trap (MOT) chamber (chamber where the Rubidium atoms are loaded and trapped). This makes it possible to load the atoms from Rubidium background gas (from a broken Rubidium ampulla which is adjusted with a valve) but still have a good vacuum at the experimental region. Also, it is expected that the vacuum will be improved when having cryogenic temperatures.

The cryostat (built by CryoVac) shown on the right in Fig. 2.1 will provide the cryogenic environment needed to cool down the atom chip. It is a closed-cycle cryostat which is cooled in two stages achieving a temperature of 4 K. It also has a translation state with which the atom chip can be placed in the correct position inside the glass cell. During this thesis, the cryostat is not yet part of the experimental setup and therefore all steps done happen in the room-temperature version of the setup (i.e. only the left part marked in purple in Fig. 2.1). Nonetheless, all decisions made are done keeping the final, cryogenic setup in mind.

The last requirement that has to be met is the sufficiently large atom number at the position where the experiment will take place. To make this possible, different experimental steps from the atom loading all the way to transporting them to the final region have to be implemented which will be described in the following. In Fig. 2.2(a) one can see the experimental setup as a CAD drawing up to the point where the cryostat will be attached and in Fig. 2.2(b) one can see the actual experimental setup.

The atoms are loaded and trapped in the MOT chamber and then transported from the MOT chamber (marked in red) into the Science chamber (marked in green) via the magnetic transport (marked in orange in Fig. 2.2(b)). In this experiment a magnetic transport was chosen instead of an optical transport as this minimizes heating through laser power in the cryogenic region to ensure a temperature of roughly 4 K. The magnetic transport was designed by Cedric Wind, based on the design by Greiner et al. [34]. The atoms are transported over 45 cm to the Science chamber.

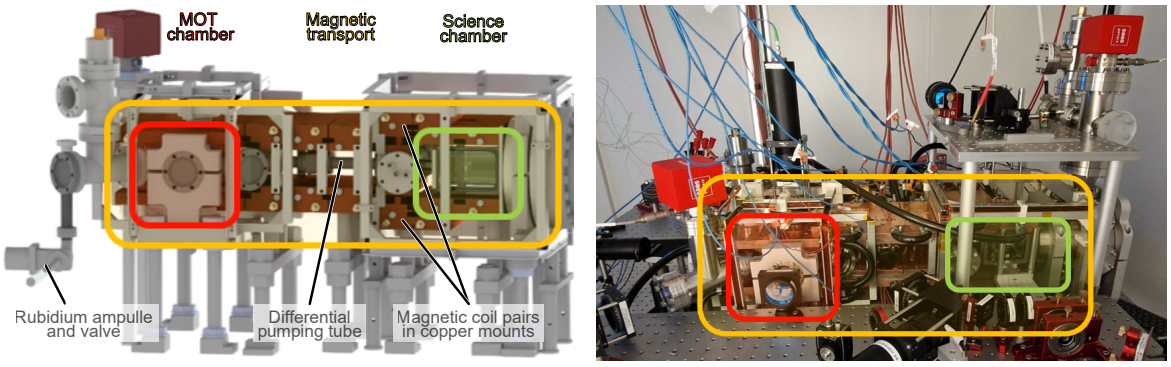

(a) (b)

Figure 2.2: Experimental setup schematic **(a)** which is the left part of the whole setup visible in Fig. 2.1 and actual setup **(b)**. Marked with red one can see the chamber for the MOT where the atoms are loaded, in orange the magnetic transport is marked and in green one can see the Science chamber where the experiments are taking place.

To achieve a sufficiently high number of atoms in the final position in the Science chamber, multiple different steps from loading the atoms, trapping and transporting them to finally trap them at the wanted position have to be implemented. All this can be found in more detail in Chapter 3.

In the last step, the atoms are trapped in the Science chamber at the position where Rydberg excitation can be conducted. The Science chamber is a self-built glass cell with one connection to the magnetic transport for the atoms to arrive and an additional flange where the cryostat will be attached. On the other four sides - top, bottom, front and back - large optical access provided by coated glass windows is apparent. The cell consists of a titanium frame and N-BK7 glass windows in the form of rectangular plates with thickness of 6 mm glued together with vacuum-compatible epoxy glue (EPO-TEK H77), which was carried out by Johanna Popp in her master thesis [35]. This is the chamber into which the cryo-shields and the atom chip will be inserted to perform the experiment mentioned above.

For the experiment, Rydberg excitation and the atom chip need to be in the Science chamber. The Rydberg excitation can be found in Chapter 4. After exciting the atoms in the Science chamber to the Rydberg state, they can either be detected via transmission spectroscopy using Single Photon Counter Modules (SPCMs) in Section 4.2 or with ionization detection as mentioned in Section 4.3.

2.2 Lasers

In this section I will give a brief introduction to the laser system required for cold atom preparation and Rydberg excitation in this experiment. The purpose of this laser table is to lock the lasers to the required transition frequency with a certain linewidth and to prepare the light so that it can be used for its specific purpose on the experimental table. The linewidth of the laser must be sufficient for its purpose. For example, the Rydberg lasers need a linewidth smaller than the energy shift between Rydberg atoms caused by the blockade effect. To achieve this, the lasers must be locked to a stable reference source. In the following, the laser setup will be explained in more detail. A schematic of the complete laser setup for the 780 nm lasers can be found in the appendix in Fig. A.1, in this chapter only specific parts are shown to explain the main use of the system.

First, a digitally controllable diode laser (from Toptica, Digital Laser Controller) called DLpro1 is locked to an external Ultra Low Expansion (ULE) cavity using the Pound-Drever-Hall (PDH) method [36, 37], which was done by Valerie Mauth in her bachelor thesis [38]. The optics used are illustrated in Fig. 2.3.

The frequency of the laser is modulated with a fiber EOM (from EOSpace) and coupled into the external cavity to generate an error signal which is fed back to the laser via a PID controller. More details on the exact procedure and the electronics used can be found in my bachelor thesis [39]. The

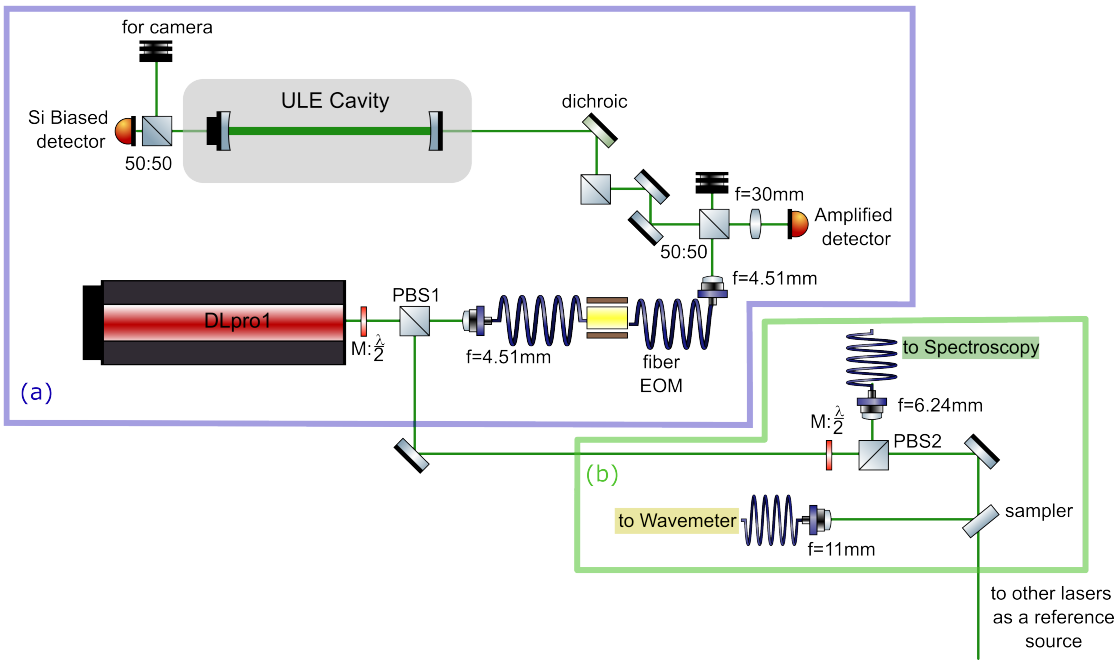

Figure 2.3: Schematic of the optics used for frequency locking of DLpro1 and preparing it as a reference sorce for additional laser locks. The light transmitted through the first polarizing beam splitter (PBS1) is coupled into an EOM fiber and locked to an ultra low expansion (ULE) cavity using the Pound-Drever-Hall method which can be seen in **(a)** in the purple box. The light reflected from the first PBS (PBS1) is used for verifying the wavelength (illustrated in green in **(b)**) by coupling a fraction of the light to a spectroscopy (reflected at PBS2) and to a wavemeter (reflected at a beam sampler). The largest fraction of the light (bottom right) is used as a reference source for locking other lasers.

frequency is also monitored using Doppler-free Rubidium spectroscopy and a wavemeter. After locking the laser, it is used as a reference source for other lasers needed in the experiment, which will be discussed below. Also an additional laser at 960 nm (from Toptica) is locked to the same cavity with a PDH locking scheme implemented by Samuel Germer in his bachelor thesis [40] (which is not explicitly shown in Fig. 2.3 but in Fig. A.1). This laser consists of a 960 nm seed laser and a second harmonic generation cavity that generates light at 480 nm. The light is guided to the experimental table in the same way as for the lasers at 780 nm, which are described in more detail below.

After frequency-locking DLpro1, it can be used as a reference frequency which makes it possible to lock other lasers at 780 nm relative to it with a certain frequency offset, realized with a so-called "Offset-Lock". With this, one does not need multiple ULE cavities (it is only possible to lock two lasers of the same wavelength to one cavity by using different polarization) as one can use an already locked laser as a new reference. This is shown schematically for DLpro3 in Fig. 2.4.
Here, the light from DLpro3 is superimposed on a photodiode with the light from DLpro1, and this detected beat signal is used to generate a phase lock using a phase frequency discriminator (ADF4007 High Frequency Divider/PLL Synthesizer from Analog Devices). Further details on the electronics can be found in my bachelor thesis [39] and further information on optimizing these locks can be found in the bachelor thesis of Valerie Mauth [38]. The light from the laser used for the experiment is split into two main arms by a half-wave plate (HWP) and a polarizing beam splitter (PBS), allowing one laser to be used for two different purposes at the same time. As the PBS only transmits horizontally linearly polarised light and reflects vertically linearly polarised light, the HWP can be used later to

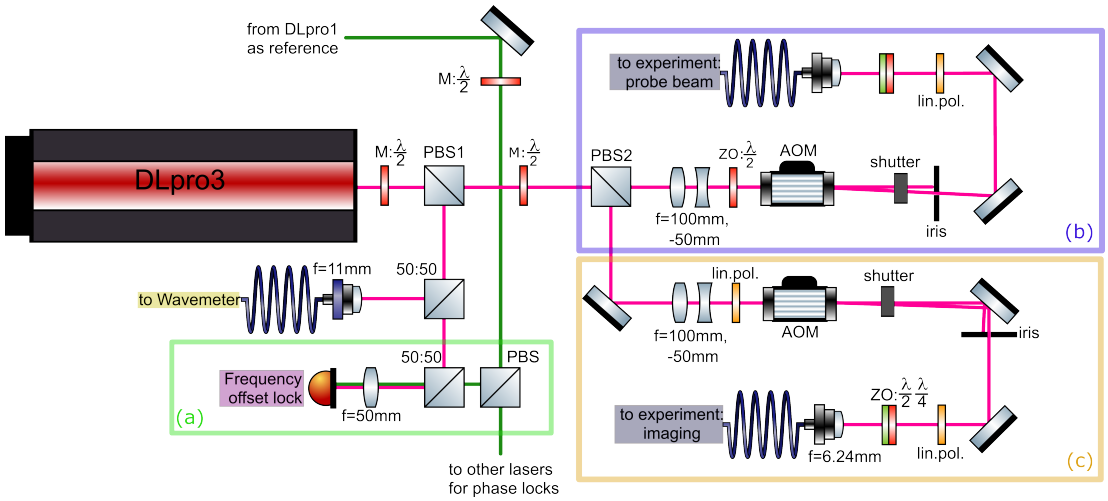

Figure 2.4: Schematic representation of the optics used to lock the frequency of DLpro3 (as an example for all other lasers at 780 nm) and to prepare it for the experiment. For frequency stabilizing the laser, the light of the reference laser DLpro1 is superimposed with the light of the laser to be locked, here DLpro3, and the beat signal detected with the photodiode is used to generate an error signal for locking the laser (visualized in **(a)** in green). On PBS2 the laser light is split into two equivalent arms (shown in purple **(b)** and orange **(c)**). First, the light is focussed onto an accousto optical modulator (AOM) which serves as an optical switch and then the light is coupled into the optical fiber which guides the light to the experiment. Waveplates in front of the AOM and the fiber (red and green) as well as linear polarizers (orange) are used to match the polarization axis of the AOM and fiber. A mechanical shutter (grey) is used to guarantee the complete turn-off of the light in the case of residual light after the AOM.

adjust the required power ratio in the experiment. The light is then coupled into an Acousto-Optic Modulator (AOM) and its first order is coupled into a single mode fiber that carries the light to the experiment. The AOM produces a frequency shift of 80 MHz, which must be compensated for in the frequency locks. There is also a mechanical shutter in the beam path to really shut off the light if necessary, as the AOM sometimes still has a certain amount of first-order power even when it is switched off. The combination of HWP and quarter wave plate (QWP) in front of the fiber together with the HWP or linear polariser (in between the telescope for matching the beam size with the size of the AOM crystal) and the AOM are used for minimizing polarization drifts after the fiber. This was done by matching the polarization axis of the light with the polarization axis of the AOM and the fiber using a polarization analyzer (from Schäfer+Kirchhoff). The laser is also coupled to a wavelength meter which can be used to check the wavelength.

This phase-locking scheme and light preparation demonstrated for the laser DLpro3 also applies to all other lasers at 780 nm. The following Table 2.1 lists the uses of each laser and its locking point and in Fig. 2.5(a) one can see the respective transitions in Rubidium ^{87}Rb.

As most of the preparation and optimization steps which will be performed in the following depend on the atomic transitions of the atomic species used, I will briefly introduce the element used. The element used in this experiment is Rubidium, which is an alkali atom and has a relatively simple hyperfine structure. The natural abundance is 27.83% ^{87}Rb and 72.17% ^{85}Rb [41, 42]. In this experiment we use ^{87}Rb because e.g. evaporative cooling is more efficient [43] compared to the other isotope. The level structure of ^{87}Rb for the ground state to the excited state can be seen in Fig. 2.5(a) and the level scheme für Rydberg excitation is illustrated in Fig. 2.5(b), as well as the transitions needed that are also listed in Table 2.1.

The exact use is discussed in more detail in Chapter 3 where the characterization and optimization of cold atom preparation is talked about in more detail.

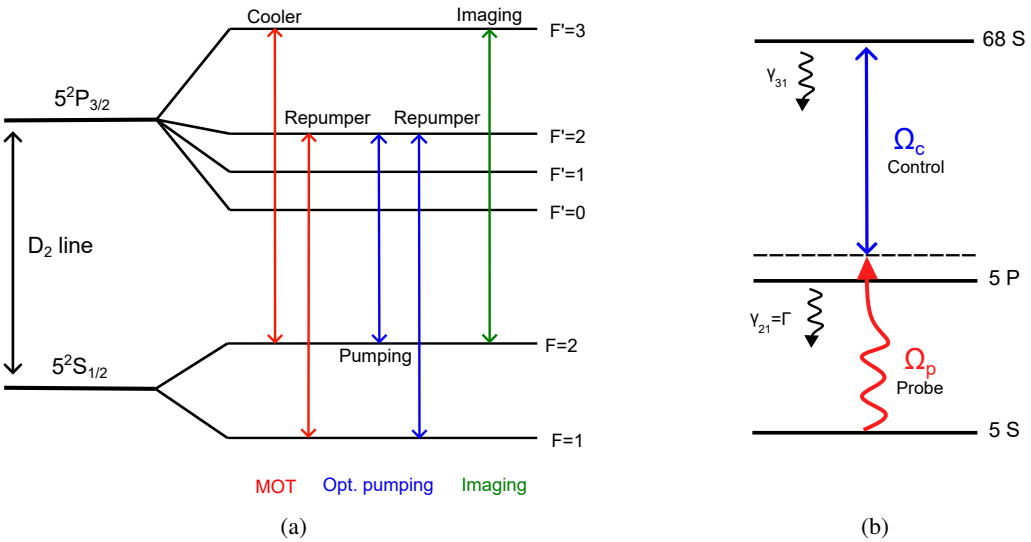

Figure 2.5: Rubidium level structure of the D2-line of ^{87}Rb based on [44] together with the usage of the different transitions in **(a)**. In **(b)** the level scheme used for off-resonant 2-photon excitation is illustrated with Ω_p corresponding to the probe and Ω_c the control coupling strength and γ being decays. The lasers for the respective transitions are mentioned in Table 2.1.

Table 2.1: Name of the respective laser, its usage and the frequency position relative to the reference laser DLpro1 where 80 MHz modulated by the AOM into first order are already taken into account. Since for some lasers the light is split into two main paths on a polarizing beam splitter right after a half wave plate and they are also used for different purposes, they are named accordingly with "transmitted" and "reflected". The laser at 480 nm is also included here, but is locked independently to the external cavity.

Laser name	Usage	transition	$\Delta\nu$ to DLpro1
DLpro1	reference laser	^{85}Rb F=$(3 \rightarrow 3, 4)$	0 MHz
DLpro2	MOT Repumper (transmitted) optical pumping Repumper (reflected)	^{87}Rb F=$(1 \rightarrow 2)$	5 421 MHz
TApro1	Cooler (main output) MOT imaging (side output)	^{87}Rb F=$(2 \rightarrow 3)$	-1 146 MHz
DLpro3	Rydberg probe (transmitted) SC imaging (reflected)	^{87}Rb F=$(2 \rightarrow 3)$	-1 146 MHz
DLpro4	optical pumping	^{87}Rb F=$(2 \rightarrow 2)$	-1 413 MHz
TA-SHGpro1	Rydberg control	^{87}Rb 5S $\rightarrow n = 68$	independent lock

2.3 Experimental sequence introduction

The experimental sequence implemented is controlled with a computer control software which talks to the individual devices needed in the experiment. This section will serve as a brief overview to explain how measurements are performed and how to understand their visualization which will be used to explain measurements done later.

The experiment cycle contains two main parts: The first part is the fixed waiting time between cycles which is used to initialize all devices and it is also the time during which the variables are saved to the data base. This makes it possible to change variables in between measurement cycles to perform scans. The second part is the duration of the sequence which is determined by the ADwin-Pro II sequence length. At this point the individual steps for one measurement are integrated. And this is the part that is visualized to explain the experiment that is performed in more detail.

ADwin-Pro, which has digital and analogue output channels that can be timed precisely, is used for triggering devices and providing control voltage. The digital channels, providing outputs of 0 V and 5 V, are used as a trigger signal for devices such as cameras, AOMs and power supplies to turn them on or off depending on what is needed. Analogue channels provide voltages from 0 V to 10 V. It is also possible to jump them, ramp from one specific value to another or to upload values from an external file. These control voltages can be used to e.g. change the power of lasers or the current through magnetic coils (and with this change the gradient of the magnetic field) depending on the applied control voltage.

In Fig. 2.6 one example of a visualization of a sequence is illustrated. The physical background of that sequence will be discussed in Section 3.2 in more detail. Here I mainly want to stress what exactly is visualized and how this needs to be understood. The applied control voltage for the specific devices is plotted as a function of the time in the experiment. At the top, one can see the analogue channels and at the bottom the digital channels. To set the laser power (green) or the magnetic field current (red) to the desired output, an analogue control voltage signal from 0 V to 10 V is applied resulting in the desired output. For the laser powers a control voltage of 10 V corresponds to an output power of 100% (1 V would correspond to 10%). For the magnetic coil current, the control voltage is applied to the Power Supply Units (PSUs) such that the current corresponds to the magnetic field that one sets in the computer control. The digital channels are used to trigger different devices. In this case here, the AOM is triggered to turn on the light and the camera is triggered to take a picture.

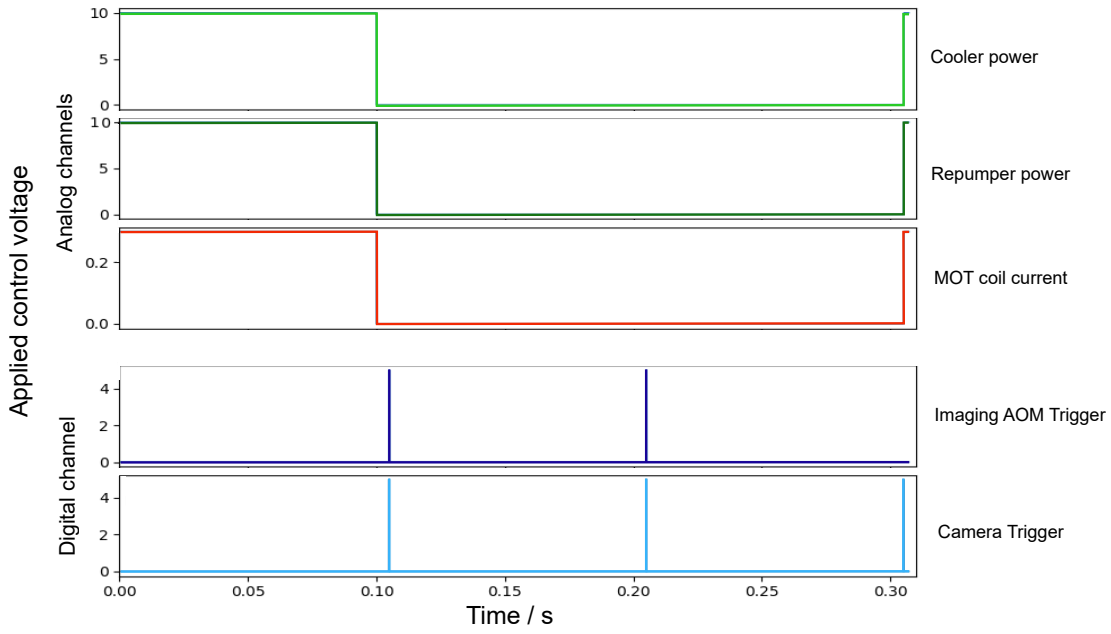

Figure 2.6: Example for an experimental sequence visualization, here in the case of a MOT loading sequence. One can see the applied control voltage from the computer control to the respective devices as a function of time. The laser power (green) and current for the coils (red) are controlled with an analogue control voltage signal from 0 V to 10 V resulting in the desired output power for the laser and output current from the power supply to the magnetic coils. For the laser powers a control voltage of 10 V corresponds to an output power of 100% and (1 V would correspond to 10%), for the coil current the output power is set such that it corresponds to the magnetic field gradient one can set in the computer control. Additionally, there is also the option for triggering devices by using the digital outputs which can either provide 0 V or 5 V. Here, this is illustrated as a trigger signal for the camera (dark blue) to take pictures and for the AOM (light blue) to turn on the laser light for imaging.

CHAPTER 3

Cold atom preparation sequence

In the HQO experiment, the main experiments will take place in a cryogenic Science chamber region. To ensure that there is no laser-induced heating from the high power MOT lasers in the vicinity of the cryostat, a two-chamber design has been chosen. One other benefit being the differential pressure in the two chambers. This means that the atoms will be loaded fast and prepared in a different location from where the actual experiment with better vacuum will take place. Several different steps to load and prepare a large number of atoms for the experiment have to be implemented.

This chapter focuses on the steps required to ensure a sufficiently large number of atoms in the science region to be able to perform the Rydberg excitation with a high optical density in the Science chamber.

First, the complete experimental sequence implemented will be introduced in Section 3.1 to serve as an overview of what needs to be done and optimized. Then, the individual steps will be explained in the respective section, the main focus being the optimization of the individual steps resulting in a high number of atoms at the position where the experiment will be conduced. This steps include loading the atoms from background gas in a MOT in Section 3.3, followed by cooling the atoms further using optical molasses which is described in Section 3.4 in more detail to better trap them in the magnetic trap. For magnetic trapping, which is discussed in Section 3.6, the atoms have to be in the correct state. This is achieved by optical pumping (see Section 3.5). Then, the atoms are magnetically trapped and transported over a 45 cm path to the Science chamber (see Section 3.8) in 1.5 s where they are kept in the final magnetic trap, where the experiment will be conducted.

It was also tried to implement MOT compression into the sequence for a better transfer of the atoms from the MOT to the magnetic trap. However, this was not successful which is discussed in more detail in Appendix B.

3.1 Experimental sequence overview

In this section, an overview of the experimental sequence is introduced. The individual parts are explained in more detail later in the respective sections.

Because of the two-chamber design, multiple steps have to be implemented to make it possible to prepare the Rubidium atoms and transport them to the position where the experiment is taking place.

A schematic of the steps needed to achieve sufficiently large number of atoms in the science region to perform the Rydberg excitation with a high optical density is illustrated in Fig. 3.1.

First, the atoms are loaded from background gas in a MOT (illustrated in yellow). The goal of this step is to load as many atoms as possible in 1 s, which is the time in between measurement cycles. Next, optical molasses is used to further cool the Rubidium atoms to make trapping them magnetically easier. This step takes place for about 5 ms. Here, one wants to reduce the temperature of the atoms without decreasing the number of atoms. To be able to trap the atoms magnetically (illustrated in light blue), it is needed to prepare the atoms in the correct state to be able to trap them. This is achieved by optically pumping the atoms for 20 µs (red). Next, the atoms are magnetically trapped (light blue) and then transported (dark blue) from the MOT chamber to the Science chamber, which is where the experiment will be conducted. In the final position, the atoms are kept in the final magnetic trap (purple).

The goal of this sequence is to maximize the atom number at the final position, where the experiment will be conducted. To optimize the individual steps, absorption imaging (illustrated in grey) is used. Two imaging systems are implemented. The imaging system in the MOT chamber makes it possible to optimize MOT loading, optical molasses, optical pumping and magnetic trapping in the MOT chamber while the imaging setup in the Science chamber makes it possible to optimize the magnetic transport and the final cloud position. Each preparation of atoms takes approximately 2.55 s until the Rydberg excitation is performed. The experiment with Rydberg excitation applied can vary in time depending on what is being measured (adding between 100 µs and ~ 100 ms depending on how many measurements are performed in succession). This makes it possible to run several measurement loops in a reasonably short time to collect data.

All the individual steps will be explained in the following sections in more detail.

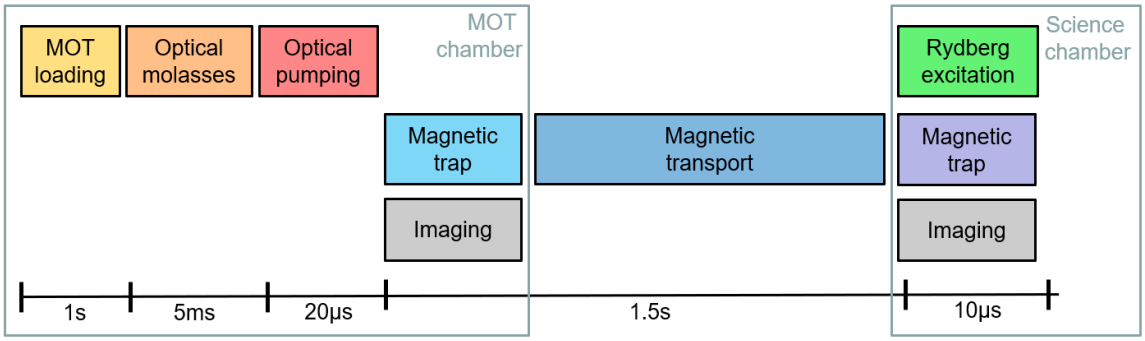

Figure 3.1: Schematic of the steps required to prepare cold Rubidium atoms for the experiment. First, the atoms are loaded and trapped using a MOT and cooled using the optical molasses method. After preparing the states with optical pumping, the atoms are trapped and transported to the region where the experiment takes place (here indicated by a Rydberg excitation). For all characterization and optimization, absorption imaging was used (illustrated in gray).

3.2 Absorption imaging in the MOT chamber

This section deals with the imaging system used in the MOT region. Absorption imaging allows for the determination of the atom number and temperature of the atom cloud. It is the tool I used to characterize and optimize the different atom preparation steps in the MOT chamber. In this experiment, absorption imaging (see Section 3.2.1) is used as the main imaging tool. Before it can be used for optimization, it needs to be characterized and optimized itself, as described in Section 3.2.2. To characterize and optimize the imaging setup, atoms are loaded and trapped using the MOT, which is described in more detail in Section 3.3. Since the imaging system will also be used to characterize and optimize the MOT, I will first explain how the imaging works here.

3.2.1 Absorption Imaging

General absorption imaging involves shining resonant light on the atoms, which is absorbed, and then detecting the shadow of the atoms (i.e., where the light is missing). From this shadow image, the spatial distribution of the atoms can be extracted. A detailed description can be found in [45] and I will present a summary of the relevant formulas in the following. To determine the optical density of the atoms, three images are taken in succession. First a picture with the shadow image of the atoms $I_{\text{atoms}}(x, y)$, then a picture of the laser beam without atoms $I_{\text{laser}}(x, y)$ and a background measurement without atoms and laser light $I_{\text{bg}}(x, y)$, where $x,\ y$ is the x and y direction, both perpendicular to the laser beam. The transmission $T(x, y)$ through an atom cloud can be described by

$$T(x, y) = \frac{I(x, y, z = L)}{I(x, y, z = 0)} = e^{-\int_0^L n(x,y,z)\sigma dz}, \tag{3.1}$$

using the Beer-Lambert law, where $n(x, y, z)$ is the density of the cloud in three dimensions, $I(x, y, z = 0)$ is the light intensity before and $I(x, y, z = L)$ after the cloud, $\int_0^L n(x, y, z)dz$ is the two-dimensional column density, and $\sigma = \frac{3\lambda^2}{2\pi}$ being the cross section for the closed cycle transition $|F = 2,\ m_{\text{F}} = 2\rangle \rightarrow |F' = 3,\ m_{\text{F}'} = 3\rangle$ of ^{87}Rb [46]. Rewriting this, one can find the column density to be

$$n(x, y) = -\frac{1}{\sigma} \ln\left(T(x, y)\right) = -\ln\left(\frac{I_{\text{atoms}}(x, y) - I_{\text{bg}}(x, y)}{I_{\text{laser}}(x, y) - I_{\text{bg}}(x, y)}\right) \frac{1}{\sigma}. \tag{3.2}$$

From these images the atom number can then be determined by summing $n(x, y)$ over all pixels.

The temperature can be extracted by performing a time of flight (TOF) measurement. This is done by varying the free fall time of the atoms before the images are taken. Depending on the initial velocity of the atoms this results in a different expansion of the atom cloud. Assuming that the spatial distribution of the atoms can be described by a Gaussian (for more details see [45]), one can fit a Gaussian to the sum of the optical density along the two axes, take the mean and determine the width given by

$$\sigma(t) = \sqrt{\frac{k_{\text{B}}T}{m}t^2 + \sigma_0}, \tag{3.3}$$

where k_{B} is the Boltzmann constant, T is the temperature of the atom cloud, σ_0 is the initial cloud size and t is the free fall time of the atoms. This is also described in more detail in [47]. One example for such a measurement can be seen in Fig. 3.2. Here, the summed optical density along one axis (in

Fig. 3.2(a) along the z-axis and in Fig. 3.2(b) along the y-axis, which are the axes perpendicular to the laser beam in the lab coordinate system) is plotted as a function of the pixels in the camera (by taking the size of pixels into account, this can be expressed in absolute sizes). By fitting a Gaussian function, the width σ can be determined. Performing this measurement for multiple TOF times t, it is possible to determine the temperature of the cloud with Eq. (3.3) for both axes. As the cloud is roughly circular in the MOT chamber, the average of both axes can be taken. This approach is used in the following to determine the temperature from absorption images taken.

So far, the mathematical treatment has only been applied to resonant imaging beams. However, if the optical density of the atom cloud is too high, the light is so strongly attenuated that almost all photons hitting the cloud are absorbed even further away from the cloud center and almost no photons reach the camera. The shadow image on the camera is then dominated by camera noise preventing a proper determination of the atom number. This is the case in our experiment when trying to resonantly image the atoms when loading the MOT for 1 s. To counteract this and still be able to detect the atoms properly, one has to change the detuning of the imaging beam and image off-resonant. Mathematically, this means that the refractive index now has a non-zero real part (shown in Eq. (3.4)), which leads to a phase shift of the imaging beam from the atom cloud. This so-called lensing effect has been studied experimentally in e.g. [48]. This can be written with the susceptibility as

$$\mathrm{Re}(\chi) = \mathrm{Re}\left(1 + \frac{\sigma_0 n\lambda}{4\pi}\left[-\frac{\frac{2\delta}{\Gamma}}{1+\frac{4\delta^2}{\Gamma^2}} + i\frac{1}{1+\frac{4\delta^2}{\Gamma^2}}\right]\right) = 1 - \frac{3n\lambda^3}{8\pi}\frac{\frac{2\delta}{\Gamma}}{1+4\frac{\delta^2}{\Gamma^2}}, \tag{3.4}$$

where Γ is the linewidth, λ is the wavelength, $\sigma_0 = \frac{3\lambda^2}{2\pi}$ is the resonant cross section and δ is the detuning [49]. For zero detuning the real part vanishes, while for blue detuning ($\delta > 0$) the light diverges and for red detuning ($\delta < 0$) the light is focused, as also discussed in [46]. In this case one has to make sure that the cloud is larger than the smallest object detectable within the deflection angle with the optics. Since the atom cloud in this experiment is large (in the order of 1 cm), it can still be

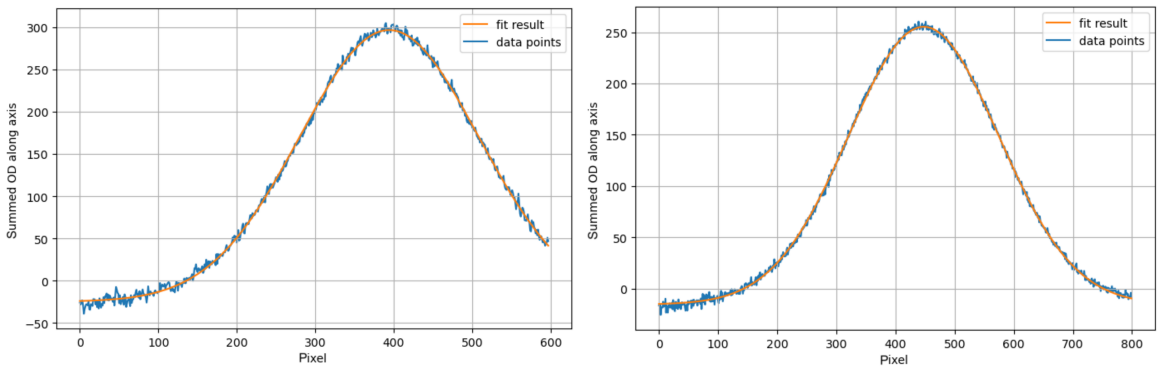

(a) (b)

Figure 3.2: Summed optical density (OD) along z-axis **(a)** and along y-axis **(b)** (in our lab coordinate system, both axes being perpendicular to the imaging beam axis) as a function of pixel of the camera. These traces are fitted with a Gaussian function from which one can determine the width of the atom cloud. By performing this for multiple Time Of Flights (TOF) t, one can determine the temperature of the atom cloud using Eq. (3.3).

measured using quantitative absorption imaging. A more detailed discussion can be found in [46].

3.2.2 Characterization and optimization of the setup

In this section, I will give a short introduction to the used imaging system, followed by a characterization and optimization of the setup. After the atoms are trapped in the MOT, the magnetic field gradient as well as the lasers are turned off before absorption imaging is applied.

A schematic of the imaging setup is shown in Fig. 3.3 (for more details on the implementation in the experiment, see the bachelor thesis of Valerie Mauth [38]). The imaging beam is provided by the side arm of the TApro1. The light is post-polarised after the fiber with a PBS (i.e. polarization corrected if it is not perfectly linearly polarised after the fiber) and then circularly polarised with a QWP, passed through the chamber and detected by a CCD camera (pco.pixelfly 1.4 USB from 2024 Excelitas Technologies Corp.) after a 0.5× magnifying telescope.

The sequence used for optimizing the absorption imaging in the MOT chamber is illustrated in Fig. 3.4. First, the MOT is loaded by turning on the Cooler laser and Repumper laser. In Fig. 3.4 this is visualized via the applied control voltage resulting in the respective power output. Also, the MOT coils are turned on to be able to trap the atoms in the MOT. After switching off the lasers and the magnetic field, a bias field is applied in the x-direction (B_x), which serves as the quantization axis for imaging, and then the three images are acquired (visualized as the trigger signal for the imaging light in dark blue and the camera in light blue in Fig. 3.4) - first with atoms, then with laser light and without atoms, and then an image without atoms and light. Before taking the first image, the atoms are in free fall for a TOF of 10 ms for all measurements present in this section (if not stated otherwise). This is done to make sure the atom cloud can be described by a Gaussian distribution and the duration was chosen such that it guarantees that the magnetic fields are turned off. With Eq. (3.2) it is then possible to determine the atom number.

After loading the atoms and turning off the laser light and magnetic field, one first needs to apply a bias field to create the quantization axis for imaging, which in this case is chosen to be $B_x = 2\,\mathrm{G}$ (in the lab coordinate system, which is along the imaging axis), and then scan the

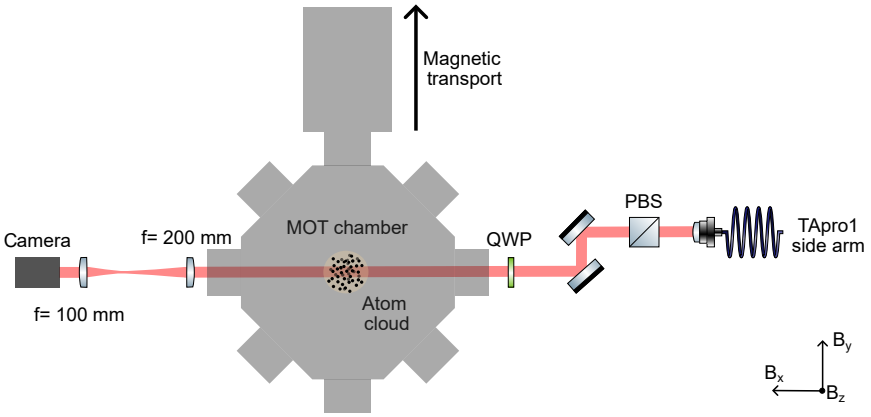

Figure 3.3: Schematic of the absorption imaging setup for the MOT chamber. The light from the TApro1 side output is polarization filtered with a PBS and circularly polarised with a QWP. After shining light onto the atoms, the light is detected on a CCD camera after a magnifying telescope of 0.5×.

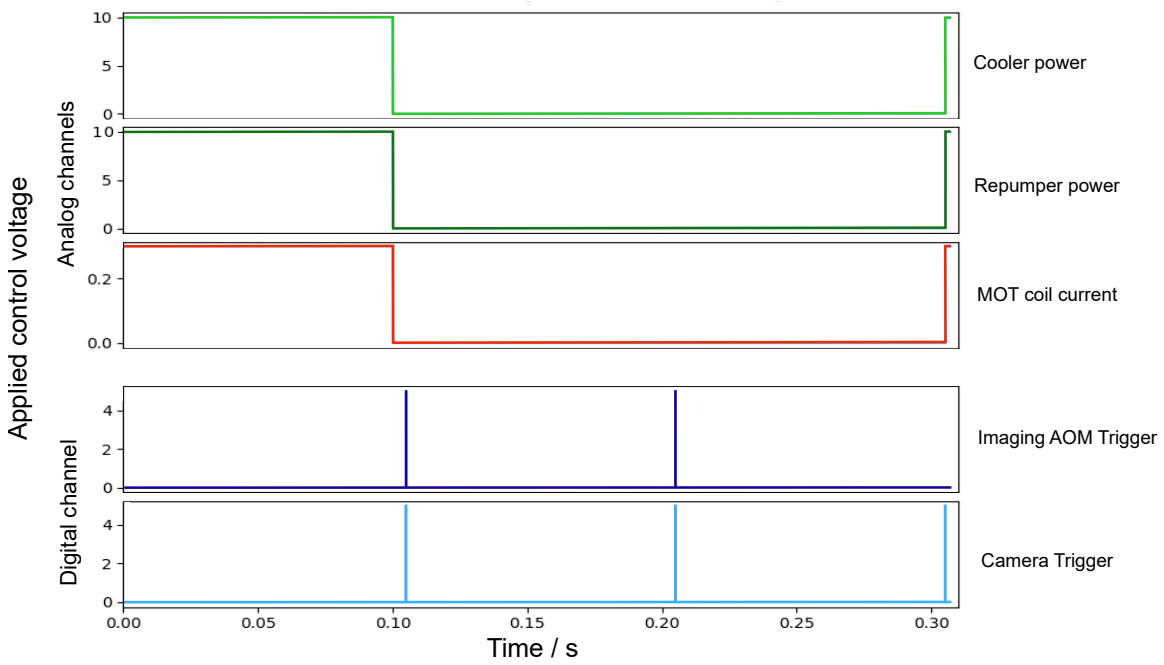

Figure 3.4: Sequence presenting the key parameters of the absorption imaging setup for the MOT chamber (see Section 3.1 for a more general explanation of the computer control sequences). Here, the applied control voltage to the devices needed is illustrated as a function of time. The main parameters for the the MOT loading are the MOT laser powers and the MOT coil current which are controlled by analogue output channels which makes it possible to set them to specific values. Here, the Cooler laser (light green) and Repumper laser (dark green) are each set to 10 V which corresponds to the highest available output power. The MOT coil current is set such that the magnetic field gradient is in the order of 10 G/cm. After the loading of the MOT, the lasers and MOT coils are turned off (by setting the control voltage to zero) and then the imaging is performed. This is realized by triggering (using the digital outputs) the light for the imaging beam (dark blue) and the camera (light blue). For the first picture taken with the camera, the atoms are still present, for the second picture the atoms are gone and only the imaging light is recorded and for the third picture a background measurement is taken.

imaging detuning to ensure that the light is resonant with the closed-cycle imaging transition of ^{87}Rb $|F = 2, m_F = 2\rangle \rightarrow |F' = 3, m'_F = 3\rangle$.

The imaging laser frequency needs to be optimized so that the detuning matches the desired transition. One would expect the detuning to be shifted due to the Zeeman shift caused by the applied bias field, which can be found to be

$$\begin{aligned}\Delta E_{\text{imag}} &= \Big(\underbrace{g_{\text{F}'}\mu_{\text{B}}}_{=0.93\,\text{MHz/G}} m_{\text{F}'} - \underbrace{g_{\text{F}}\mu_{\text{B}}}_{=0.7\,\text{MHz/G}} m_{\text{F}} \Big) \cdot B \\ &= (0.93\,\text{MHz/G} \cdot 3 - 0.7\,\text{MHz/G} \cdot 2) \cdot 2\,\text{G} \\ &= 2.78\,\text{MHz}\,,\end{aligned} \tag{3.5}$$

with $g_{\text{F}'}\mu_{\text{B}} = 0.93\,\text{MHz/G}$ for $F' = 3$ and $g_{\text{F}}\mu_{\text{B}} = 0.7\,\text{MHz/G}$ for $F = 2$ taken from [42]. Here, g_{F} is the Landé g-factor, μ_{B} the Bohr magneton and m_{F} the magnetic quantum number. This is done by scanning the detuning of the imaging laser and evaluating the atom number, assuming that the

detuning would be at 0 MHz, as shown in Fig. 3.5(a). The optimum detuning found (maximum absorption and therefore highest calculated atom number) is set as the new offset (here: 3.1 MHz), as this is our new zero detuning point. This is in the same order of magnitude as one would expect due to the Zeeman effect in Eq. (3.5). Derivations might be caused by additional field components (like the earth magnetic field, the slowly decaying field of the MOT coils or caused by eddy currents) which are not entirely eliminated by the set bias field. To check that the detuning offset is set correctly, another detuning search is performed, but this time with the new zero detuning offset already corrected. One would expect the atom number to be constant across different detuning values, as these are compensated for in the calculation of the atom number. In Fig. 3.5(b) one can see that the offset has been set correctly. The value stays roughly the same over a span of 20 MHz. The trend to higher atom numbers for detunings that are further from resonance can be explained by not taking the Doppler broadening or lensing effect into account when correcting for the detuning.

All the measurements shown so far have been made with short loading times of 300 ms, which corresponds to an atom number in the order of 10^8. However, we aim for higher atom numbers in the experiment. Therefore, in most cases a loading time of 1 s is used, corresponding to up to 10^9 atoms with an OD too high to be imaged with the imaging laser being on resonance. This is the case because the light is attenuated so much that the shadow images is dominated by camera noise and with this it is not possible to determine the number of atoms. This is why the cloud is imaged off-resonant instead.

When imaging off-resonant, one has to take into account the previous considerations of lensing

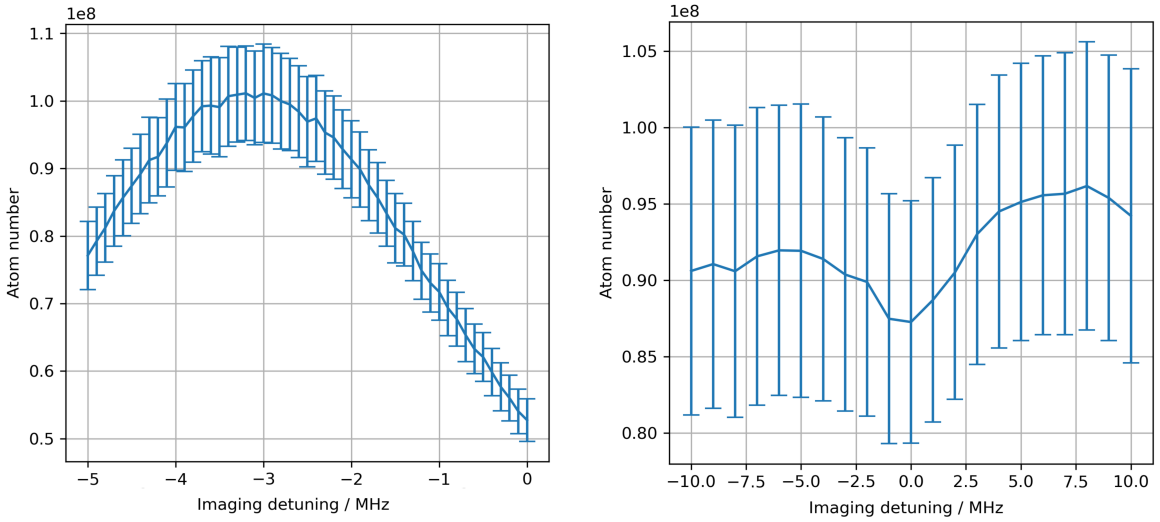

(a) (b)

Figure 3.5: Atom number as a function of the detuning of the imaging laser beam. **(a)** shows the atom number that is calculated from absorption images assuming that the detuning is 0 MHz for all points to see the influence of the scan. One can see the average of seven measurement cycles. An optimum at around 3.1 MHz is visible. In **(b)** the atom number is calculated for each detuning while performing the scan, taking into account the newly found offset from **(a)**. An average over 11 measurement cycles is displayed. The calculated atom number is the same for each detuning when taking the theoretical correction into account. The maximum atom number in **(b)** is smaller since the measurements were performed at different days with slightly different Rubidium pressure in the MOT chamber.

effects, i.e. the different effects for blue detuned and red detuned imaging, as shown in Eq. (3.4). The main goal of the imaging is, however, to use it as a tool to optimize the different atom preparation steps such that the atom number is as high as possible where quantitative uncertainties do not play a crucial role. Independent of the imaging detuning, a higher number of atoms should correspond to a higher number of atoms measured with absorption imaging. A more detailed estimation of the real atom number by combining on-resonant absorption imaging and fluorescence imaging is given in Section 3.3.2 as here the lensing effect does not play are role and does not need to be compensated for.

To test if higher atom numbers correspond to a higher measured number of atoms for both, resonant and off-resonant imaging, this was measured in the following. The number of atoms was varied by loading the MOT for different times (longer loading time corresponds to more atoms being trapped) and then absorption imaging was performed for resonant imaging light in Fig. 3.6(a) and for off-resonant (here: 10 MHz) imaging light in Fig. 3.6(b). In both cases one can see that longer loading times corresponding to a larger atom number also leads to a higher measured atom number. This makes it a valuable tool for optimizing the individual steps in the MOT chamber.

For all optimizations in the MOT chamber, the imaging is set to resonance for small atom numbers and the imaging detuning is set to 10 MHz for large atom numbers.

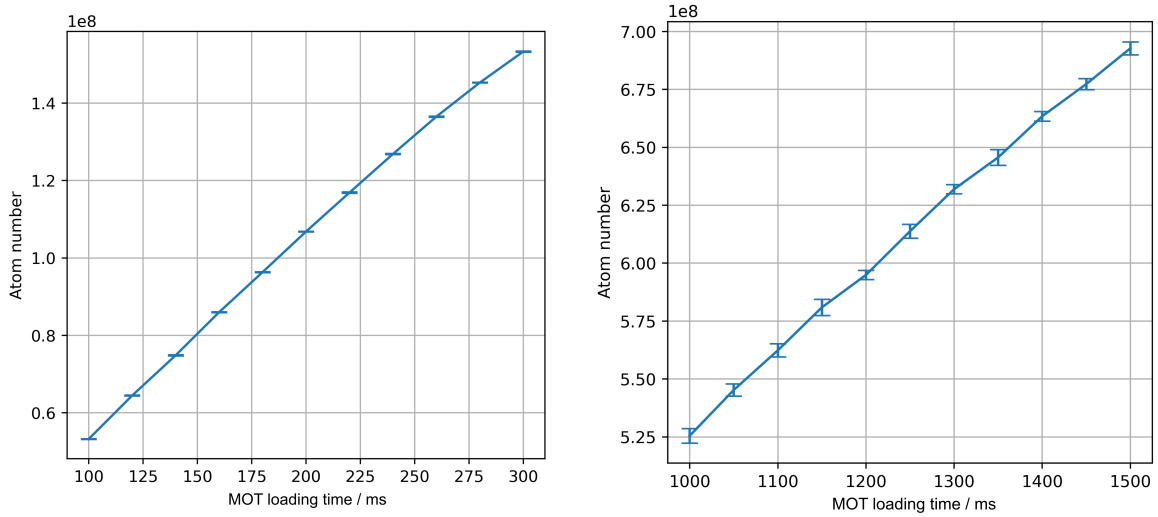

(a) (b)

Figure 3.6: Atom number as a function of MOT loading time for **(a)** resonant absorption imaging and **(b)** off-resonant absorption imaging averaged over 10 measurement cycles each. As loading for longer corresponds to a higher number of Rubidium atoms, one can see that no matter if the imaging was resonant or off-resonant, higher number of atoms corresponds to a higher atom number determined with the imaging setup. This makes it a valuable tool for optimizing for high atom numbers even when using off-resonant imaging light.

3.3 Loading and trapping of Rubidium atoms

In this section, the first step of the cold atom preparation required for the experiment is discussed in more detail, namely the loading and trapping of the Rubidium atoms from the background gas. Here, it is crucial to have a high atom number to start with as the next steps will only lead to a decrease of atoms and one wants to ensure a high atom number for the later experiments. First, the working principle of a magneto optical trap is discussed in Section 3.3.1. The experimental realisation in the HQO experiment as well as the optimization steps are then discussed in more detail in Section 3.3.2.

3.3.1 Magneto optical trap (MOT)

In this experiment, the MOT is used to cool and trap neutral Rubidium atoms as a first step in the cold atom preparation required to perform the desired experiments.

A key concept used here is laser cooling of neutral atoms, described in more detail in [50, 51]. It takes advantage of the conservation of momentum. When an atom is illuminated with laser light resonant with an atomic transition, the photon is absorbed and its momentum $\vec{p} = \hbar\vec{k}$ (where $\vec{k} = \frac{2\pi}{\lambda}$ is the wave vector, λ is the wavelength) is transferred to the atom. This momentum kick leads to a recoil in the direction of the photon. The direction of the spontaneous decay after absorption is random, which means that on average there is no momentum change induced by this process. This results in a net momentum change only given by photon absorption.

To ensure that the atoms are cooled, which means that their velocity is reduced (i.e. only atoms moving towards the laser beam experience the momentum transfer), one needs to use Doppler cooling. As the atoms propagate along the optical axis of the laser beam, they see a shift in the frequency of the laser beam due to the Doppler effect. This results in a cooling force for an atom (treated as a two-level system) in one dimension, which can be described by the scattering force

$$F_{\text{scatt}} = \hbar k \frac{\Gamma}{2} \frac{I/I_{\text{sat}}}{1 + I/I_{\text{sat}} + 4\delta^2/\Gamma^2}\,, \tag{3.6}$$

where Γ is the natural linewidth of the atomic transition, I is the intensity of the transition, I_{sat} is the saturation intensity and δ is the detuning of the laser beam [50]. By choosing the frequency to be red-detuned ($\delta < 0$) it is possible to target only atoms moving towards the laser beam. When this is extended to three dimensions, any atom moving in the region within the overlapping laser beams will be slowed down. This is the so-called optical molasses, which will be discussed again in Section 3.4 when talking about sub-Doppler cooling. Mathematically speaking, in one dimension, one looks at the forces of the counter-propagating beams on the atoms, which can be expressed as

$$\begin{aligned} F_{\text{molasses}} &= F_{\text{scat}}(\omega - \omega_0 - kv) - F_{\text{scat}}(\omega - \omega_0 + kv) \quad \big| F_{\text{scat}} \text{ from Eq. (3.6)} \\ &= -\alpha \cdot v\,, \end{aligned} \tag{3.7}$$

with ω being the frequency of the lasers, ω_0 being the resonant absorption frequency of the transition and kv resulting from the Doppler effect with v being the velocity of the atoms [50]. This holds for low velocities $kv \ll \Gamma$, with $\alpha = 4\hbar k^2 \frac{I}{I_{\text{sat}}} \frac{-2\delta/\Gamma}{\left[1+(2\delta/\Gamma)^2\right]^2}$ [50]. From this one now gets a velocity dependent force.

To trap atoms, an additional spatially dependent force is needed. This is realised in a MOT with a

pair of magnetic coils in anti-Helmholtz configuration, which create a quadrupole field that is spatially dependent and has its magnetic field minimum in the center of the overlap region of the laser beams. This lifts the degeneracy of the m_F states due to the Zeeman effect [52]. The Zeeman shift was already introduced in Eq. (3.5) from which one can see that the splitting depends on the absolute magnetic field as well as the magnetic quantum number m_F. With the resulting energy shift of the states it is more likely to drive one transition (e.g. σ^+) than the others by shifting one level closer to resonance (e.g. $m_F \rightarrow m_{F'} = m_F + 1$) as illustrated in Fig. 3.7. This is later relevant as we need σ^+ polarized light in our experiment to drive the wanted transition $|F = 2, m_F = 2\rangle \rightarrow |F' = 3, m_{F'} = 3\rangle$ of ^{87}Rb.

By combining a velocity dependent force for slowing down the atoms together with a spacial dependent force for confining the atoms, this results in

$$F_{\mathrm{MOT}} = -\alpha v - \frac{\alpha\beta z}{k}\,, \tag{3.8}$$

with $\beta z = \frac{g\mu_B}{\hbar}\frac{dB}{dz}z$ being the Zeeman shift at displacement z [50]. This makes it possible to cool and trap the atoms.

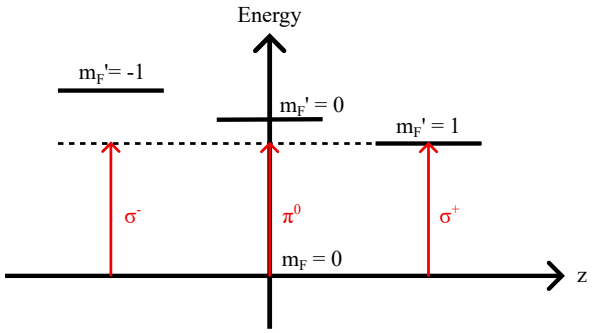

Figure 3.7: Schematic of a general energy level diagram for explaining the working principle of a MOT based on [53]. The transition $|F = 0, m_F = 0\rangle \rightarrow |F = 1, m_F = (-1, 0, 1)\rangle$ is illustrated for the case of an applied external magnetic field. Frequency and polarization are chosen such that the light is resonant with the $|F = 0, m_F = 0\rangle \rightarrow |F = 1, m_F = 1\rangle$ transition.

3.3.2 Characterization and optimization of the setup

The MOT implemented in this experiment as well as some loading characterizations and optimizations will be discussed in more detail here. As mentioned above, the trapped atomic species is ^{87}Rubidium, which is provided by a Rubidium source. The background pressure is at the order of 10^{-9} mbar and the vacuum is maintained by an ion pump. The level scheme with the levels relevant for the MOT can be seen in Fig. 3.8. Two lasers are needed to trap the atoms in the MOT chamber, the Cooler laser and the Repumper laser. The Cooler drives the σ^+- transition $|F = 2, m_F\rangle \rightarrow |F' = 3, m_{F'} = m_F + 1\rangle$ which ends in the closed cycle transition $|F = 2, m_F = 2\rangle \rightarrow |F' = 3, m_{F'} = 3\rangle$ where the laser cooling takes place as described in Eq. (3.7). Due to red detuning and imperfections in the excitations, some atoms end up in $|F = 1, m_F\rangle$ and are therefore lost from the cooling cycle. The Repumper excites the lost atoms back to $|F' = 2, m_{F'}\rangle$ which brings them back to the closed cycle cooling transition.

As discussed before both Cooler and Repumper laser light needs to shine on the atom cloud from all six sides. This is realized by both lasers being coupled into two fiber beam splitters (1:4 and 1:2 (from

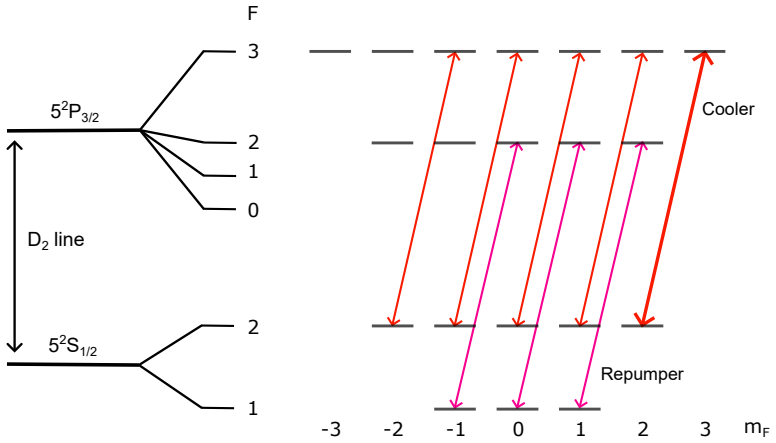

Figure 3.8: Energy level diagram for the hyperfine splitting of ^{87}Rubidium based on [44]. The Cooler drives the σ^+- transition $|F = 2\rangle \rightarrow |F' = 3\rangle$ which ends in a closed-cycle transition where cooling takes place. Some atoms end up in $|F = 1\rangle$ which are excited back to $|F' = 2\rangle$ by the Repumper laser.

Evanescent Optics Inc.)), which are then out-coupled to the collimators in front of the MOT chamber as shown in Fig. 3.9. Here, the collimators are supplied with light from the 1:4 fiber beam splitter in the horizontal plane and the 1:2 fiber beam splitter for the vertical axis. This allows counter-propagating power balanced beams from the same laser source. A QWP is mounted in front of the collimators to produce the circularly polarised light required to drive the correct transition. Additionally, the frequency and intensity needs to be controlled and stabilized to ensure stable operation over a long period of time.

The magnetic quadrupole field which provides the spacial dependence for trapping the atoms is generated by two parallel so-called MOT coils in anti-Helmholtz configuration mounted in a copper block. The copper blocks are slit to reduce eddy currents [54] and are water cooled. Bias coils (visualized by the cage system for the bias coils) are also implemented to allow the position of the cloud to be changed (by changing the minimum position of the quadrupole field) and to provide a quantisation axis if required. Changing the position of the atom cloud is important later to overlap the MOT position with the starting point of the magnetic transport.

There are also additional viewports used to image the atom cloud. Fig. 3.9(a) shows the absorption imaging axis, which is described in more detail in Section 3.2. This imaging setup is used for most of the measurements needed to optimize the various steps of cold atom preparation in the MOT chamber. Fig. 3.9(b) also shows the fluorescence imaging system used to monitor the fluorescence of the atom cloud with a camera. Both imaging systems will be used in the following to optimize the atom loading.

The sequence for performing the MOT loading can be seen in the previous section in Fig. 3.4 for the demonstration of absorption imaging. The main steps are to switch on the magnetic field, the Cooler light and the Repumper light. The parameters that have a large influence on the atom number are the overlap of all beams in the center of the magnetic field, the polarization of the light, the magnetic field gradient (as it can be seen in Eq. (3.8)), the detuning of the Cooler and the Repumper and their powers as shown in Eq. (3.6).

Beam overlap was done with irises on either side of the viewports and fine tuning could be done by maximizing the atom number using fluorescence imaging. The polarization was roughly set using a reference waveplate and then fine-tuned by looking at the live image of the atoms again using

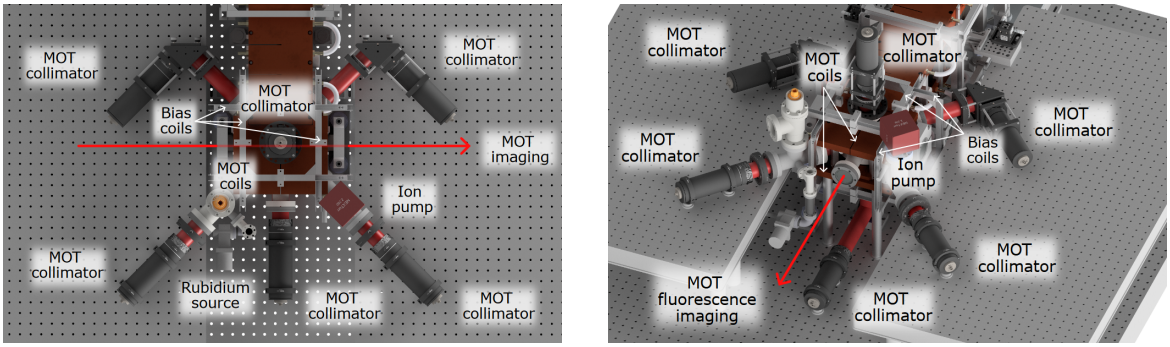

(a) (b)

Figure 3.9: Schematic of the MOT chamber made by Cedric Wind **(a)** from top down and **(b)** from the side. Four collimators in the horizontal plane and two in the vertical axis provide the trapping light. The MOT coils in Anti-Helmholtz configuration are mounted in copper blocks which are water-cooled. The bias coils coil mounts are shown and the coils themselves were hand-wound. The Rubidium is provided by a Rubidium source and the vacuum is maintained by a ion pump as part of the vacuum setup. Both, the absorption imaging setup as well as the fluorescence imaging setup are marked with red arrows.

fluorescence imaging. Next, the power for the two MOT lasers was looked at in more detail which can be seen in Fig. 3.10. Here, the atom number is measured for different values of Cooler and Repumper power which are displayed in control voltages (10 V corresponds to the maximal available output power of 95 mW for the Cooler and 3 mW for the Repumper in each MOT beam, which is about the size of $1/e^2$ diameter $\sim$ 37.5 mm). Higher Cooler and Repumper powers should lead to a stronger trapping force (as it can also be seen Eq. (3.6)) independent of the detuning of the two lasers as long as the Cooler is much stronger than the Repumper. This is also apparent in the measurement.

The next thing to look at is the detuning of the lasers used. Since the detuning depends on the splitting of states (i.e. the choice of the magnetic field gradient), it is important to check both at the same time. This is done by performing a 2D scan of these two parameters, as shown in Fig. 3.11(a). The detuning of the Cooler laser is red detuned with respect to the on-resonant Cooler transition (The detuning of the Cooler laser is given as a positive value). For this scan, a clear trend is apparent and a set of parameters can be determined that leads to the highest atom number. Furthermore, one also has to check for the optimal detuning of the Repumper laser. To do so, the detuning of the Repumper laser is scanned while using the newly found values for the Cooler detuning and magnetic field gradient and the determined atom number is visualized in Fig. 3.11(b). With these scans it is then possible to find the magnetic field gradient to be 10.5 G/cm, Cooler detuning of 29 MHz and a Repumper detuning range of 0 MHz up to 20 MHz which lead to highest MOT loading atom numbers in the order of 10^9 atoms.

For most of these optimization measurements, off-resonant absorption imaging was used (for more details on that, see Section 3.2) which works for optimizing the atom number but it does not necessarily provide the correct absolute atom number. To determine the absolute atom number, one can use the fluorescence imaging together with the resonant absorption imaging and by combining both, it is possible to determine the absolute number of atoms. The number of atoms $N(t)$ after a set time t during MOT loading can be determined as follows:

$$N(t) = N_0 \cdot (1 - e^{-t/\tau}) \,, \tag{3.9}$$

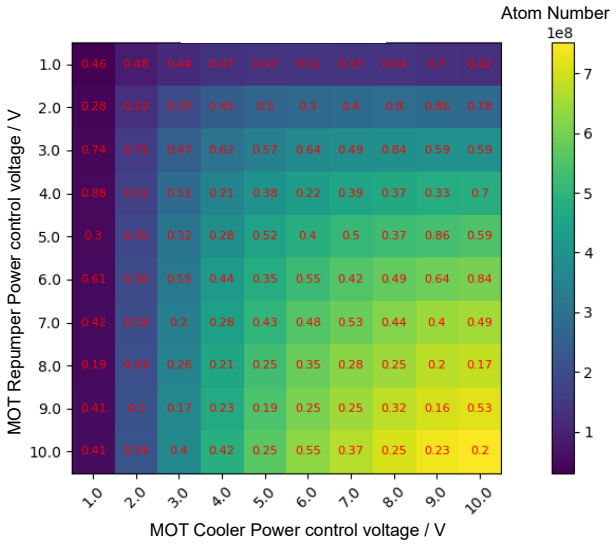

Figure 3.10: Atom number measured for different Repumper and Cooler control voltages. For this measurement the MOT was loaded for 1 s and the imaging detuning was set to 10 MHz. Four measurement cycles were performed and the average is displayed here. The red numbers correspond to the relative errors in percent determined as the standard error of the mean. One can see that the higher the powers of the laser (here: higher control voltage also corresponds to higher output powers) results in a higher atom number.

with τ being the loading time and N_0 the atom number in equilibrium [55]. From fitting the loading curve measured with fluorescence imaging, as illustrated for one example in Fig. 3.12(a)) with Eq. (3.9) and an offset to take the background into account, the loading time τ can be determined. This has been done for six different loading curves and their respective values are summarized in Table 3.1 and the mean loading time can be found to be (1.82 ± 0.03) s.

The atom number in equilibrium can can be calibrated with on-resonant absorption imaging. When only looking at short loading times (i.e. in the order of tens of ms), Eq. (3.9) can be Taylor expanded to first order which results in a linear function of the form

$$N(t) \approx \frac{N_0}{\tau} \cdot t \,. \tag{3.10}$$

When now loading the MOT for short times and measuring the atom number with on-resonant absorption imaging (see Fig. 3.12(b)) it is possible to fit a linear function to the data and with this determine the atom number at equilibrium with Eq. (3.10):

$$N(t) \approx \frac{N_0}{\tau} \cdot t \stackrel{!}{=} m \cdot (t - t_{\text{offset}}) \,, \tag{3.11}$$

with m being the slope that is fitted to the data. For the plot seen, one could find $m \cdot (t - t_{\text{offset}}) = (1.20 \pm 0.01) \cdot 10^6\,\text{ms}^{-1} \cdot (t - (8.08 \pm 0.22)\,\text{ms})$. The time offset can be explained by the time it takes for the mechanical shutters to open which is in the order of 8 ms.

Putting the two parameters found together, one can now determine the maximum atom number by combining Eq. (3.9) and Eq. (3.11) and one can find for a loading time of $t = 1$ s (as this is the value used in the experiment)

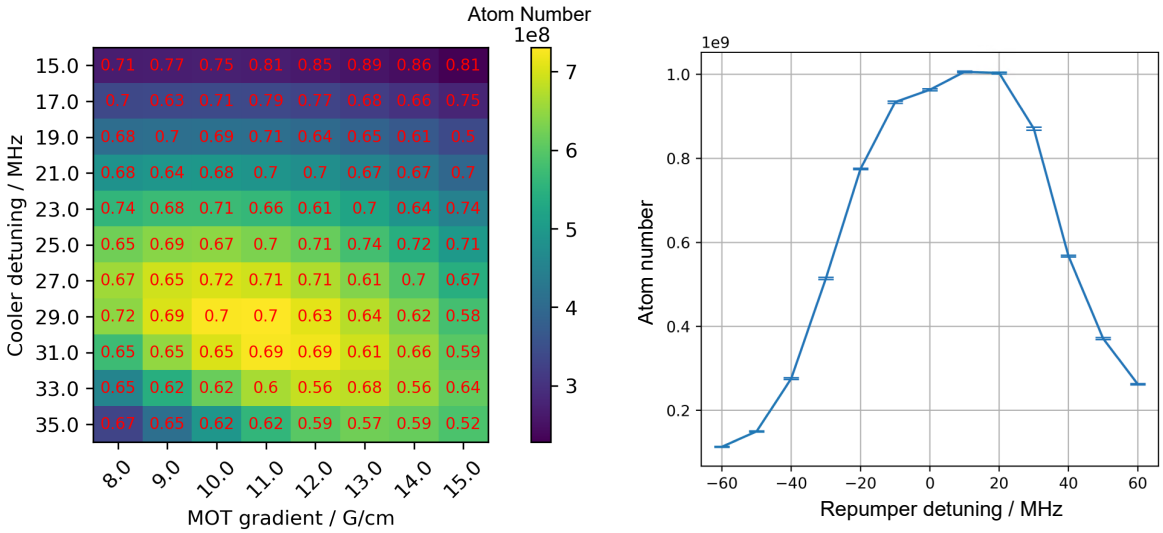

(a) (b)

Figure 3.11: Atom number as a function of MOT magnetic field gradient (here: MOT gradient) and Cooler detuning for 1 s MOT loading time before optimizing the Repumper detuning in **(a)**. The measurement was repeated for 18 times and the red numbers are the relative error in percentage. Here, one can see a clear optimum. In **(b)** one can see the atom number as a function of the detuning of the Repumper laser for 1 s MOT loading time. This measurement was repeated 17 times. One can see a range for which the atom number is the highest. For both measurements the imaging detuning was set to 10 MHz.

$$N(t) = m \cdot \tau(1 - e^{-t/\tau}) \tag{3.12}$$
$$= (9.20 \pm 0.15) \cdot 10^8 \,.$$

This shows that the atom number is of the same order of magnitude as what is displayed with off-resonant absorption imaging meaning that off-resonant absorption imaging is a good tool to estimate the atom number in this experiment. In the following, all characterization and optimization measurements in the MOT chamber are provided by off-resonant absorption imaging.

As a final characterization measurement of the atoms in the MOT one can determine the temperature

Table 3.1: Fitted values for fluorescence imaging fit of life time τ and N_0 using $N(t) = N_0 \cdot (1 - e^{-t/\tau}) + c$ as a function which is illustrated in Fig. 3.12(a) for one example. The errors mentioned are fit errors.

No.	τ / s	$\Delta\tau$ / s	$N_0 \cdot 10^6$	$\Delta N_0 \cdot 10^4$	c·10^6	$\Delta c \cdot 10^4$
1	1.77	0.03	1.44	1.01	0.96	1.07
2	1.84	0.03	1.37	0.92	1.04	0.97
3	1.89	0.03	1.42	1.06	1.00	1.13
4	1.81	0.03	1.45	0.93	0.95	0.98
5	1.83	0.03	1.39	1.10	0.96	1.07
6	1.81	0.03	1.46	1.09	0.94	1.15

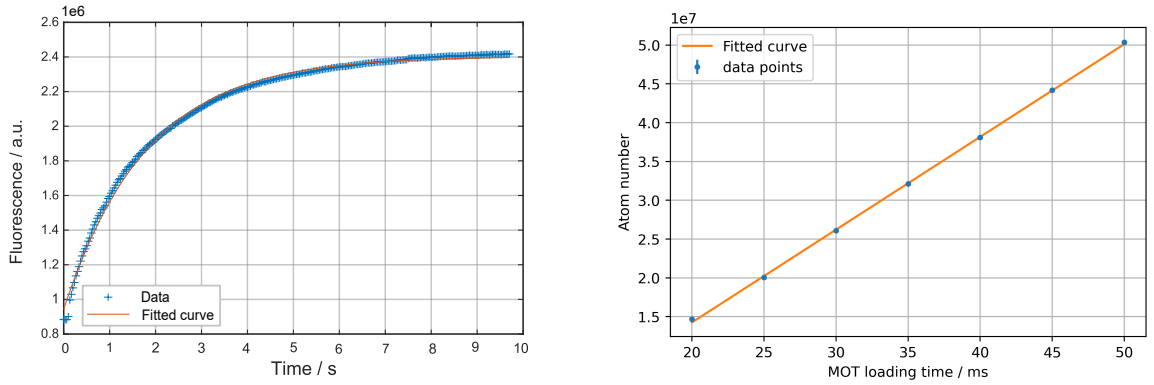

(a) (b)

Figure 3.12: **(a)** Example for a MOT loading curve measurement with fluorescence imaging for 10 s of loading the atoms from background gas. A loading curve was fitted to determine the loading time of the MOT τ. In **(b)** one can see the atom number as a function of small loading times averaged over 10 measurement cycles using absorption imaging. Here, "loading time" corresponds to the time the MOT was loaded before measuring the atom number. A linear function was fitted to the data to determine the maximum atom number.

of the atoms which is shown in Fig. 3.13. This is done by performing a time of flight measurement which is described in more detail in Section 3.2. The cloud size as a function of the free expansion time (TOF) t is shown. By fitting Eq. (3.3) one can determine the temperature to be (373.7 ± 15.7) µK. This is above the Doppler temperature for Rubidium which is discussed in more detail in Section 3.4.1 where the goal is to reduce the temperature of the atom cloud.

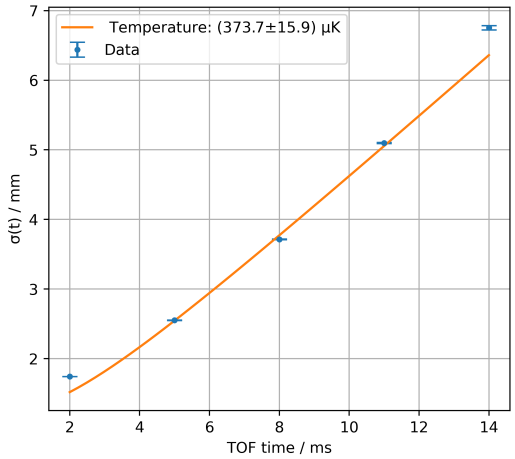

Figure 3.13: Full width half maximum of the cloud expansion determined by a Gaussian fit to the summed density $\sigma(t)$ (see Section 3.2.1) as a function of the free expansion time of the cloud (TOF time). The measurement was repeated for 46 times for a MOT loading time of 1 s. By fitting Eq. (3.3), one can determine the temperature.

3.4 Sub-Doppler cooling

Once the Rubidium atoms have been loaded and trapped in the MOT, it is advantageous to cool them further to make the next steps of state preparation and magnetic trapping more efficient. This is the case since the next steps take up some time and a reduced temperature of the atoms leads to a smaller expansion of the cloud and therefore better confinement during the next steps. This is done using the optical molasses described in Section 3.4.1. It has been implemented in the experimental sequence and optimized so that the atom number remains high but the temperature of the atoms is reduced below the Doppler temperature, as described in Section 3.4.2.

3.4.1 Optical molasses

The working principle of optical molasses and laser cooling for a two level atom has already been described in Section 3.3.1, where the velocity dependent force created by counter-propagating laser beams was introduced in Eq. (3.7). It is not possible to cool the atoms to zero velocity because there is heating caused by the laser beams which competes with the cooling force. By equating the cooling and heating rates, it is then possible to determine a minimum temperature, the so-called Doppler temperature, which is given by

$$T_D = \frac{\hbar\Gamma}{2k_\mathrm{B}}, \tag{3.13}$$

with Γ being the linewidth, and k_B the Boltzmann constant [56].

To counteract this, a so-called sub-Doppler cooling mechanism has to be applied, which in the case of this experiment is possible because of the multi-level structure of the atom together with a rotating laser polarization. A detailed mathematical derivation of the sub-Doppler cooling is described in [58] and I want to stress the idea of the concept in the following.

Since the light for the MOT is circularly polarised and in the atomic frame σ^+ from one side and σ^- from the counter-propagating beam, this results in a rotating linear polarization at the position of the atom. Looking at a level scheme with sublevels, as shown in Fig. 3.14(a), π-transitions take place, i.e. from $m_F \Rightarrow m'_F = m_F$ (shown in green). Looking at the Clebsch-Gordan coefficients for such a level scheme, one can see that the transition starting at $m_F = 0$ is more intense than the transitions starting

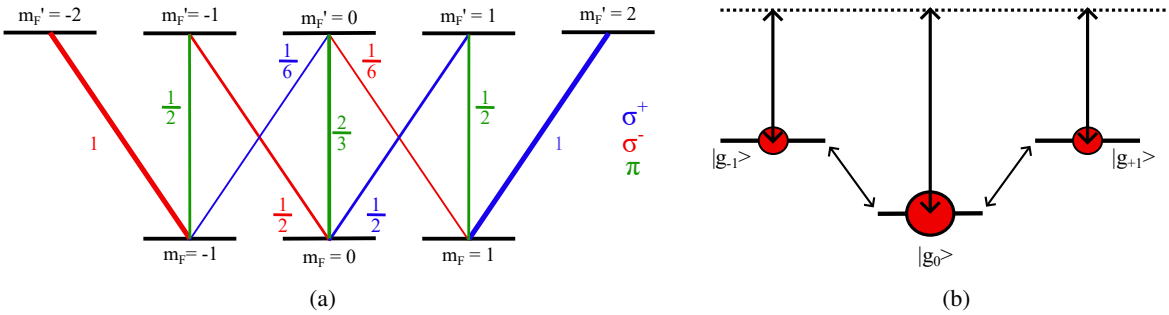

Figure 3.14: **(a)** Atomic level scheme with Clebsch-Gordon coefficients [57] to illustrate different transitions and their respective probabilities. **(b)** Light-shifted ground state sublevels in the case of $\sigma^+ - \sigma^-$ configuration, based on the figure from [58]. The steady state population is represented by the red circle and the arrows between the ground states indicate coupling.

at $m_F = (-1, 1)$, resulting in a stronger light shift for the $m_F = 0$ transition compared to the other two (which experience the same but smaller light shift). Also, due to the Clebsch-Gordan coefficients, the $m_F = 0$ state has the strongest population. Next, it is useful to work in a rotating frame with a fixed polarization direction. This leads to an additional rotation term depending on the velocity of the atoms and their magnetic quantum number. This results in a coupling between the different sub-levels, which is illustrated in Fig. 3.14(b). In addition, one can also see the light-shifted ground state sub-levels as discussed above. This coupling then leads to an asymmetric mixing of the sub-levels, resulting in an absorption imbalance, which leads to a force in the opposite direction to the motion of the atoms, assuming that the light shift is much larger than the linewidths. With this model it is then possible to determine the temperature given by the sub-Doppler cooling process, which leads to

$$k_B T \propto \frac{\hbar \Omega^2}{|\delta|}, \tag{3.14}$$

in the limit of $|\delta| \gg \Gamma/2$, where Ω is the Rabi frequency of the transition and δ is the detuning, which is described in more detail in [59]. This can now be well below the Doppler limit.

3.4.2 Characterization and optimization of the setup

Optical molasses is used to reduce the temperature of the atoms. In the MOT it was possible to achieve a temperature of roughly 370 µK (see Section 3.3.2 for more details on that). The goal of optical molasses is to cool the atoms below their Doppler temperature, which is given by Eq. (3.13). For Rubidium this is 146 µK [42]. The main parts of the sequence used are shown in Fig. 3.15. After loading the atoms into the MOT, the MOT coils are switched off, allowing for optical molasses. To perform optical molasses the laser powers and detunings need to be adjusted.

Optimal molasses parameter would result in a reduction of the temperature of the atoms without significant atom loss. This is why both, a measurement of the atom number and a measurement of the temperature, are performed for different parameter sets. To determine the temperature of the atoms, a TOF measurement is performed which is described in more detail in Section 3.2.1. To find the best parameters, first a molasses duration of 10 ms is set because this is expected to be long enough to cool the atoms. Also, this duration is still small enough for the cloud to not expand too much such that it can be imaged with the absorption imaging setup.

First, the Cooler power and detuning are scanned and for each parameter set a TOF measurement is performed to extract the temperature as done in Fig. 3.16(a) as well as the atom number which is plotted in Fig. 3.16(b). Here, one can see that for a Cooler power of 9.5 mW (as an analogue control voltage of 1 V corresponds to a Cooler power of 10% of the maximal available power of 95 mW) in one MOT arm and a red detuning towards 90 MHz most atoms are lost and therefore, this is not a good parameter set. Apart from that, most parameter sets seem good with regards to atom loss and this is why the main focus lies in the temperature of the atoms. When having a look at the temperatures in Fig. 3.16(a), one can see that it increases for higher Cooler power and smaller red detuning which is expected when looking at Eq. (3.14). A trade-of needs to be found where the atom number is still high but the temperature sufficiently low. This is the case for a control voltage of 5 V applied for the Cooler power and a detuning of 90 MHz.

The Repumper is expected to not have much impact on the molasses because it is only needed to recapture atoms that fall out of the cooling cycle if they end up in the wrong state. It is important,

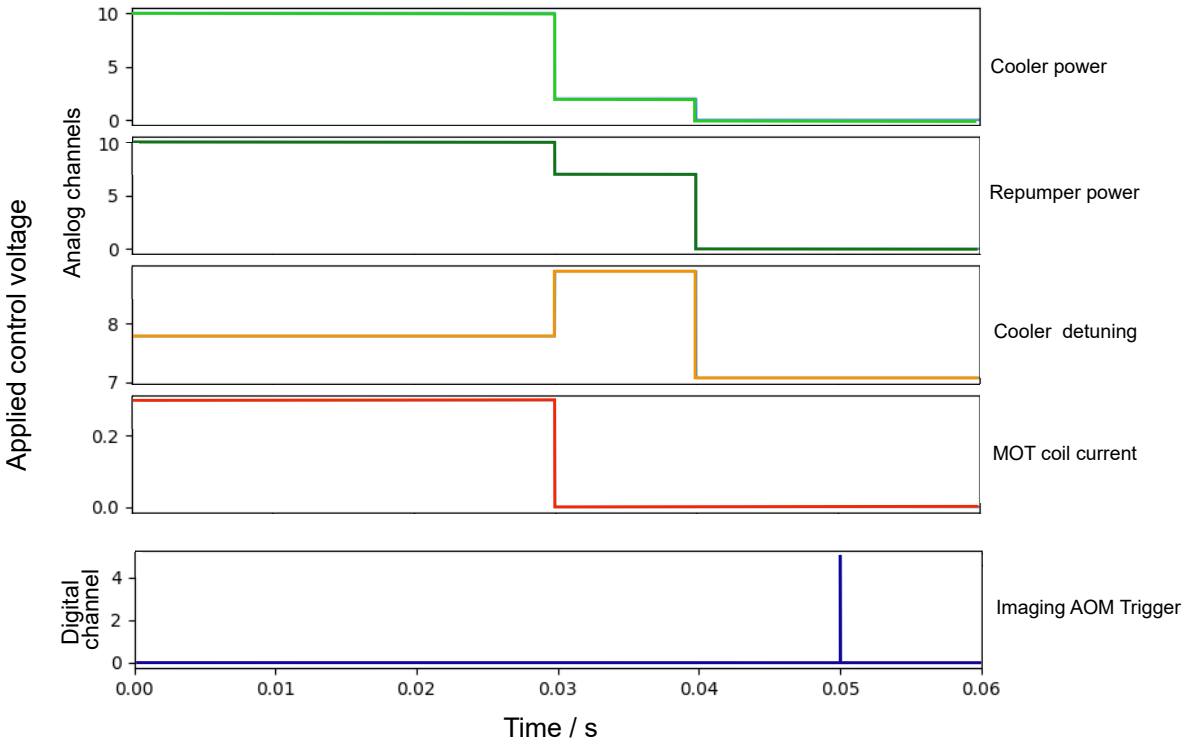

Figure 3.15: Sequence used for optical molasses showing the key parameters for this step in the experiment. The applied control voltage is displayed as a function of the time. First, the MOT is loaded for 1.03 s (the MOT coil current (red) as well as the power of Cooler (light green) and Repumper laser (dark green) are set to the optimal values found for MOT loading), then after 30 ms the MOT coils are turned off, which is the optical molasses part. During optical molasses, the laser powers and detunings have to be adjusted. After that, absorption imaging is performed (here: illustrated by the digital trigger signal for the camera).

however, that the Repumper is much weaker in power compared to the Cooler laser.

Next, one has to find the optimal molasses duration. Here, it is important to find a duration that is long enough to reach a low temperature but still short enough to keep the cloud sufficiently small. This is needed to make sure that trapping the atoms sufficiently with the magnetic trap is possible later. To do so, the duration of the molasses is scanned and for each duration a time of flight measurement is performed. This makes it possible to check for the temperature depending on the duration of optical molasses. The following measurement can be seen in Fig. 3.17. Here one can see that the temperature starts at roughly 300 µK in the MOT and then by performing optical molasses, the temperature decreases for a duration of 5 ms after which the impact of optical molasses is not apparent any more. This is why the Molasses duration is chosen to be 5 ms in this experiment.

With this scans being done and the parameters for optical molasses being optimized, it is now possible to compare the temperature in the MOT (roughly 370 µK, for more details, see Fig. 3.13) and the optical molasses to see what the impact of this step is compared to MOT alone. The time of flight measurement after optical molasses is shown in Fig. 3.18. Here, the size of the cloud as a function of the TOF is illustrated and by fitting Eq. (3.3) one can determine the temperature to be (26.7 ± 0.4) µK. This is below the initial MOT temperature and with this proves that a decrease of temperature was possible. Also, this value is below the Doppler-temperature limit. This is now a good starting point

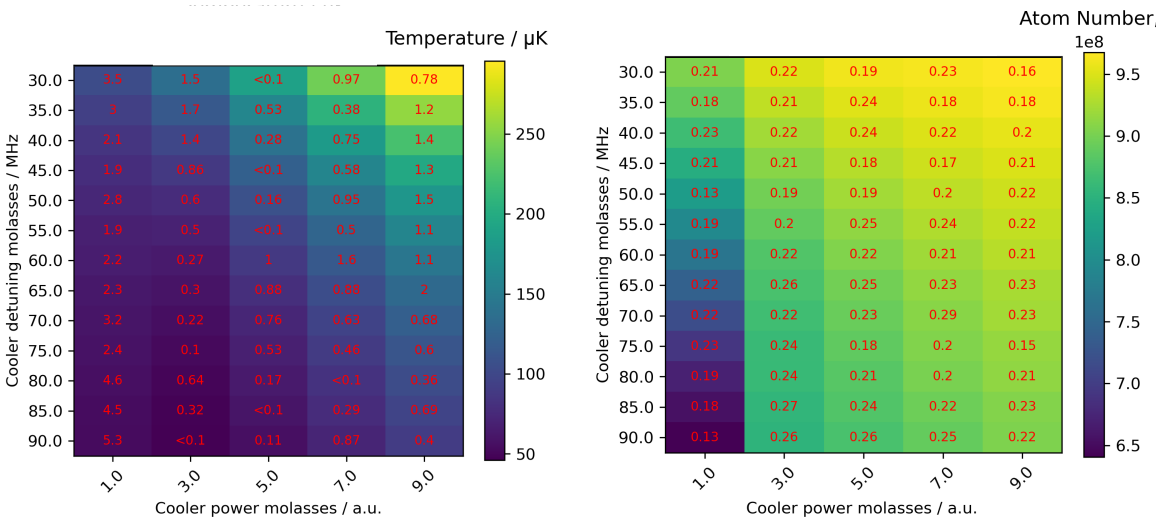

(a) (b)

Figure 3.16: Temperature measured for a scan of the Cooler detuning and the Cooler power by performing TOF absorption imaging **(a)** and the number of atoms for the same scan for a set TOF of 10 ms **(b)**. The power is displayed in applied control voltage from the computer control. The measurement was repeated for 10 times and the red numbers correspond to the relative errors in percent. The duration of molasses for this measurement was set to 10 ms.

for performing state preparation and trapping of the atoms in the following.

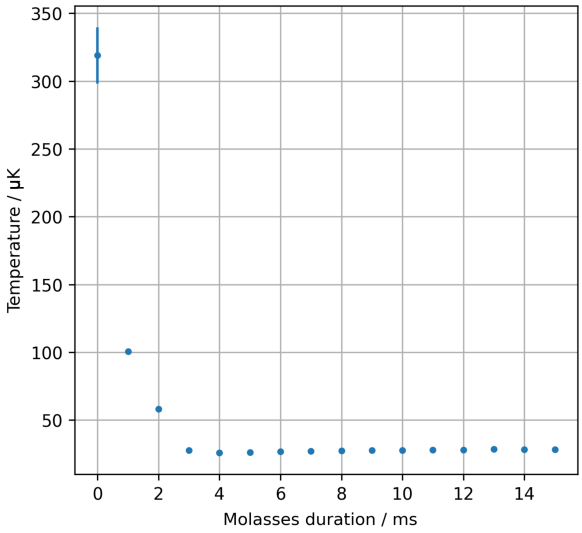

Figure 3.17: Temperature measured for different durations of optical molasses averaged over 10 measurement cycles by performing TOF absorption imaging. Starting from the temperature in the MOT, the temperature decreases to approximately 30 µK after performing optical molasses for 5 ms. After 5 ms the temperature does not decrease further.

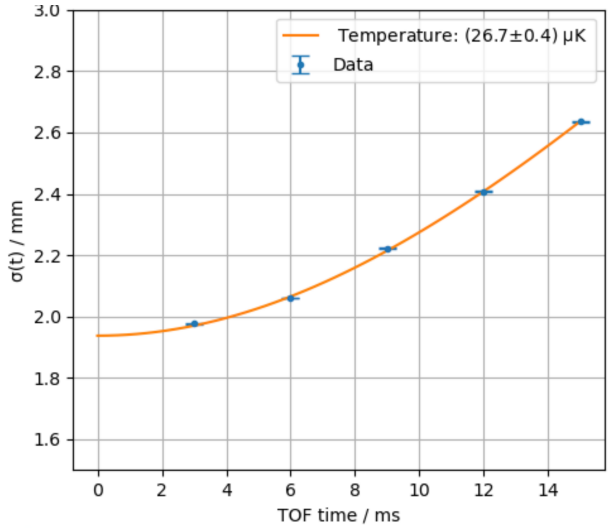

Figure 3.18: Full width half maximum of the cloud expansion determined by a Gaussian fit to the summed density $\sigma(t)$ as described in Section 3.2.1 as a function of the TOF. The measurement was repeated for 13 times for a MOT loading time of 1 s and a molasses time of 5 ms. By fitting Eq. (3.3) to the data, the temperature can be determined to be (26.7 ± 0.4) µK.

3.5 State preparation for trapping

Optical pumping is needed for state preparation to make magnetic trapping more efficient in the next step. In the magnetic trap only states with $|F = 2, m_F = (+1, +2)\rangle$ are trapped, while negative magnetic quantum numbers are not. After molasses, however, it is not guaranteed that all atoms are in the correct state, which leads to atom loss. To counteract this, state preparation is performed, in our case by optical pumping. More detail on the theory has been discussed in [60].

In this experiment, the optical pumping and optical repumping light is superimposed on the MOT imaging beam path due to the limited optical access to the atoms in the MOT chamber, as visualized in Fig. 3.19(a), by using beam splitters. As the polarization needed for the optical pumping and optical repumping light is the same as what is used for the MOT imaging light (here: σ^+ polarization), this has already been optimized when setting up the imaging.

Optical pumping is optimal when all atoms end up in the $|F = 2, m_F = 2\rangle$ dark state. This is the state in which the atoms can later on be trapped magnetically. The level scheme in Fig. 3.19(b) shows the required transitions. The optical pumping beam (shown in light red) drives σ^+ transitions between the $F = 2$ and $F' = 2$ states. Due to selection rules and multiple pumping cycles, most of the atoms end up in the dark state $|F = 2, m_F = 2\rangle$, where they cannot be pumped further (in contrast to e.g. the MOT loading scheme, where a closed-cycle transition is used). An additional laser, the Repumper laser is used, similarly to the MOT loading scheme, to repump atoms that have fallen to the $|F = 1\rangle$ state back to the pumping cycle.

To optimize the state preparation, it is useful to image the atoms with the optical pumping transition $|F = 2, m_F = 2\rangle \rightarrow |F' = 2, m_{F'} = 2\rangle$ after performing optical pumping. Since they are pumped to a dark state for exactly this transition, one would expect a reduction in absorption. This makes it possible to optimize the optical pumping by reducing the absorption from the atom cloud when imaging on this transition, while still checking using imaging on the MOT transition (the transition generally used for MOT imaging $|F = 2, m_F = 2\rangle \rightarrow |F' = 3, m_{F'} = 3\rangle$) as one would expect to see all the atoms there. Also, when optical pumping is done efficiently, one can see a higher absorption on the MOT imaging transition compared to atoms which are not optically pumped. This is the case

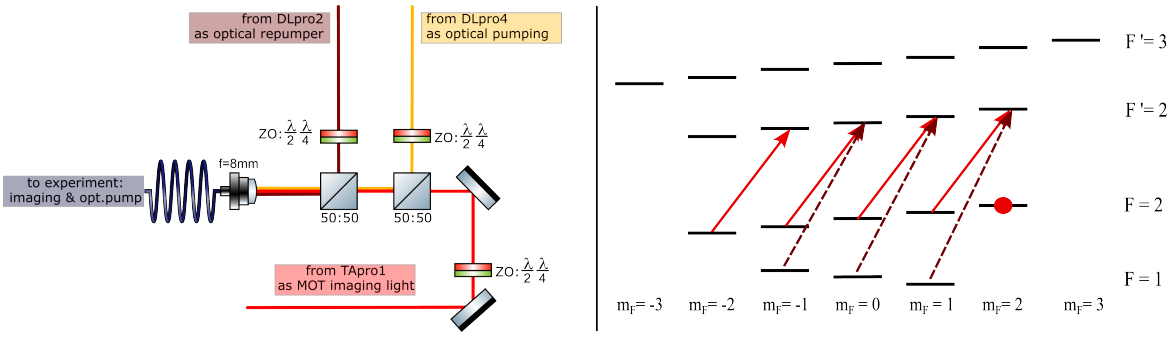

(a) (b)

Figure 3.19: **(a)** Schematic of the laser system needed for preparing the light for optical pumping. The light of MOT imaging, optical pumping and optical repumping are all coupled into the same fiber and guided to the experiment. The level scheme addressed by the optical pumping and optical repumping laser can be seen in **(b)** where red is the Pumping transition and brown the Repumper transition for optical pumping. Due to selection rules, most atoms end up in the dark state marked in red.

because when pumped, the atoms are already in the closed cycle transition (i.e. in the $|F = 2, m_F = 2\rangle$ state) where the imaging is performed and do not need to be pumped there first. This cross-checking on both, the MOT imaging and optical pumping transition, guarantees to distinguish between better optical pumping (as this would have no effect on atom loss at the MOT imaging transition) and general atom loss due to parameter choice (e.g. too high power which would lead to pushing the atoms away, or wrong detuning and many more).

Before this can be done, the laser DLpro4 used for optical pumping must be calibrated for imaging in the same way as the MOT imaging laser in Section 3.2.2. First, the quantization axis is set to $B_x = 2\,\mathrm{G}$ as for this value the level shift is still small enough such that one is still close to resonance. As the choice of the quantization field leads to a shift of the states, the detuning offset has to be found to be able to compensate for this offset. The offset is expected to be (calculated as it was done in Eq. (3.5) for the MOT imaging) $(0.93\,\mathrm{MHz/G} \cdot 2 - 0.7\,\mathrm{MHz/G} \cdot 2) \cdot 2\,\mathrm{G} = 0.92\,\mathrm{MHz}$.

To find the frequency for which DLpro4 is resonant with the optical pumping imaging transition with the set bias field, the detuning of DLpro4 is scanned and the atom number is calculated for each detuning plotted in Fig. 3.20. Here, one has to note that the calculated atom number is not correct since here it was calculated as if one would be imaging on the $|F = 2, m_F = 2\rangle \rightarrow |F' = 3, m_{F'} = 3\rangle$ transition instead of the optical pumping transition. Nonetheless, the detuning for highest absorption can be found to be at 2 MHz which corresponds to the detuning offset. The derivation from the theoretical value can be explained by the previously set zero detuning only being rounded to integers as it is only used as a starting point for finding the correct detuning. Also, residual magnetic fields also might have an impact to the resulting detuning value. The offset of 2 MHz is taken into account when performing measurements on this transition.

Additionally, it has to be possible to change the detuning of the optical pumping laser during one measurement sequence and not only between measurement sequences. Since the reference source

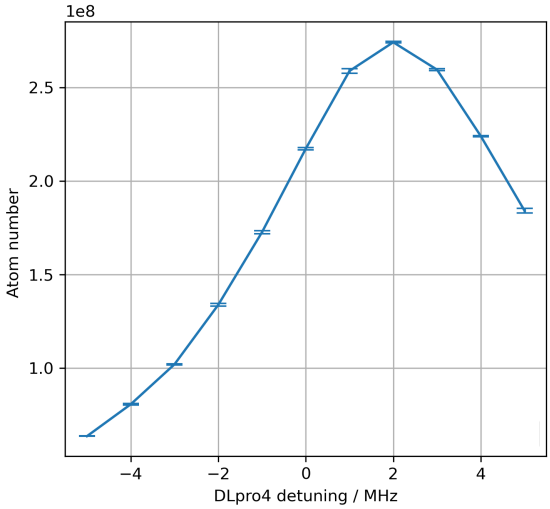

Figure 3.20: Reconstructed number of atoms calculated for the Cooler transition (and not for the used optical pumping transition) as a function of the detuning of DLpro4. This makes it possible to find the detuning for highest absorption to be 2 MHz but it is not possible make a statement about the absolute atom number here. The average of three measurements is illustrated for a MOT loading time of 1 s.

for the phase locks in this experiment is realized by a DDS board and an arduino, the channel could be modified such that a frequency ramp during the sequence is possible. With this one can scan the detuning of DLpro4 for the optical pumping step and then jump to the detuning needed for imaging.

First, the power and detuning of the optical pumping beam must be considered. A quantization axis is applied and then the detuning has to be optimized to drive the desired transition. The power must also be set so that the optical pumping works but the atoms are not blown away and lost. All this was done for a fixed optical pumping duration of 20 µs. These measurements are shown in Fig. 3.21. When one first looks at the MOT imaging measurements in Fig. 3.21(a), the atom number remains approximately constant for optical pumping powers of 290 µW (as this corresponds to a set control voltage of 5 V set by the computer control) and above. One cannot see any loss of atoms for higher powers, as we are not yet in the regime where atoms are blown away. However, one can see when the atoms are not pumped correctly, as this is visible in a lower absorption. If we now look at the measurement taken with optical pumping as the imaging light (see Fig. 3.21(b)), we can see the exact opposite, as expected. The pumped atoms are not visible for the imaging light. This makes it possible to determine a wide range of parameter sets that would work best. It is advisable to choose one set for the time being and to do this scan again on the Science chamber side, as the more atoms are pumped correctly, the more atoms should arrive. This is done in Section 3.8.

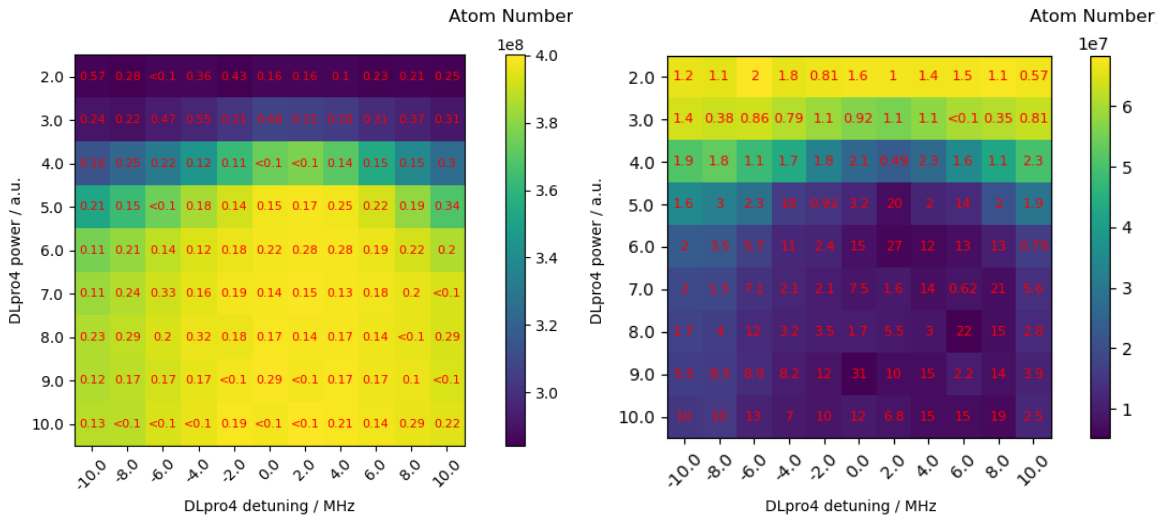

(a) (b)

Figure 3.21: Reconstructed number of atoms as a function of optical pumping laser power (displayed by set control voltage with 10 V corresponding to the maximal available output power of 580 µW) and detuning imaged on **(a)** the MOT transition and **(b)** the optical pumping transition. The average of three measurement cycles in displayed for both plots. The atom number is calculated both times for the MOT transition and measured for MOT loading of 1 s, optical molasses of 5 ms and optical pumping of 20 µs. The red numbers correspond to the relative error in percent.

3.6 Magnetic trap in MOT chamber

After state preparation of the atoms, it is possible to trap them driving the MOT coils with a higher control voltage of 3.37 V producing a gradient of 130 G/cm along the axial direction. This trap is the initial step needed for the magnetic transport because from that coil onwards the atoms are transported over 45 cm which is discussed in the next chapter in Section 3.8. In this section, the characterization of the magnetic trap in the MOT chamber is discussed in more detail.

Fig. 3.22 shows the sequence used for loading the atoms in the magnetic trap and highlights the most important steps during this sequence. First, the MOT loading takes place for 30 ms (Cooler and Repumper are set to the highest output power, for more details, see Section 3.3.2) and optical molasses for 5 ms (MOT coils are turned off and the laser powers are adjusted such that the atoms are cooled, for more details on that, see Section 3.4.2). After applying optical pumping for state preparation (illustrated in purple and described in more detail in Section 3.5), the atoms are trapped by rapidly ramping the MOT coil current to produce a magnetic field gradient of 130 G/cm in the axial direction. Here, the bias fields are adjusted such that the overlap between the initial MOT position and the start of the magnetic transport is optimized. This is done by using fluorescence imaging to have a look at the cloud in x- and y-direction and absorption imaging is used to check for y- and z-direction. With this it is possible to set the bias fields by checking from all directions.

When ramping the MOT coils to turn on the magnetic trap for trapping the atoms, this results in

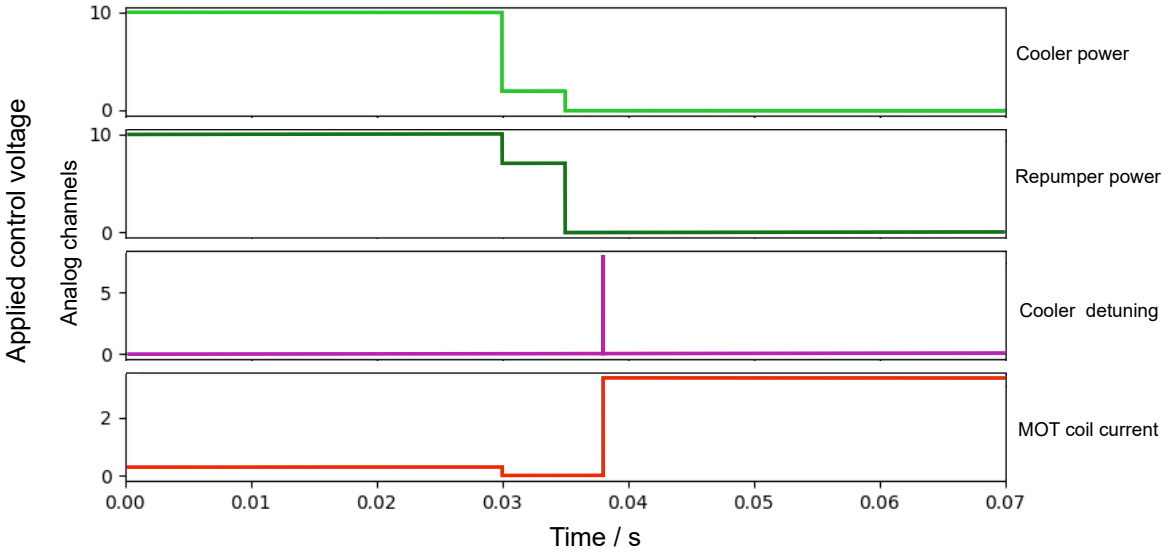

Figure 3.22: Sequence illustrating some of the key parameters for all steps up to trapping the atoms in the magnetic trap in the MOT chamber. The applied control voltage to to the respective devices as a function of the time in the experiment is visualized. First, the MOT loading (for 1 s and an additional 30 ms) takes place which is shown here by the maximal applied control voltage for the Cooler (light green) and Repumper laser (dark green). Then, optical molasses is performed for 5 ms, where the magnetic field is turned off (red) and the Cooler and Repumper power is adjusted. Then, the optical pumping is performed (analogue signal provided to the Optical pumping laser for 20 µs, shown in purple). After that, the trapping of the atoms takes places by ramping the magnetic field gradient to a higher value.

sloshing of the atoms. The main reason for this is that the ramping of the magnetic field is too slow which results in the atom cloud expanding and especially falling before being trapped in the magnetic trap. Additionally to that, it is not possible to turn the magnetic trap off fast due to eddy currents being generated in the copper cooling blocks. This leads to the presence of a residual magnetic field for up to 20 ms.

The time it takes for the coils to turn on and off was measured with a current clamp (AC/AD Current Clamp CC-65 from Hantek, calibrated with [61]) and a magnetic field sensor (DRV425EVM from Texas Instruments, calibrated with [62]). The resulting measurement for turning on the coils is displayed in Fig. 3.23. It takes roughly 13 ms for the field to reach the maximum value, when rapidly ramping the magnetic field gradient from 0 G/cm to 130 G/cm at the cloud position, and roughly 25 ms to stabilise (see Fig. 3.23(a)). Also, it takes up to 8 ms for the magnetic field to turn off completely which is displayed in Fig. 3.23(b). The magnetic field sensor does not display zero field for the magnetic field being turned off as the Earth magnetic field is still present (roughly 0.4 G [54]). As the magnetic fields turn on slowly, the atoms fall and are then kicked upwards when the trap is turned on resulting in sloshing of the atoms in the magnetic trap.

It was tried to compensate for that by changing the bias fields and with this the position of the cloud before trapping but it was not possible to get rid of the sloshing.

To have a closer look at the sloshing effect, the holding time in the magnetic trap is varied and absorption images are taken. For this, the center position of the cloud is determined and plotted as a function of the holding time. This is done in Fig. 3.24(a) for the y-direction corresponding to left-right and in Fig. 3.24(b) for the z-direction corresponding to top-down. The center position is given in pixels which are of the size of 6.45 µm × 6.45 µm and the atoms are detected with a magnification of 0.5 which means that the sloshing in y-direction corresponds to ∼ 60 pixels = 0.77 mm and in z-direction ∼ 80 pixels = 1.03 mm. The sloshing results in an increase of kinetic and potential energy of the atoms which is quickly turned to a higher cloud temperature due to thermalization caused by

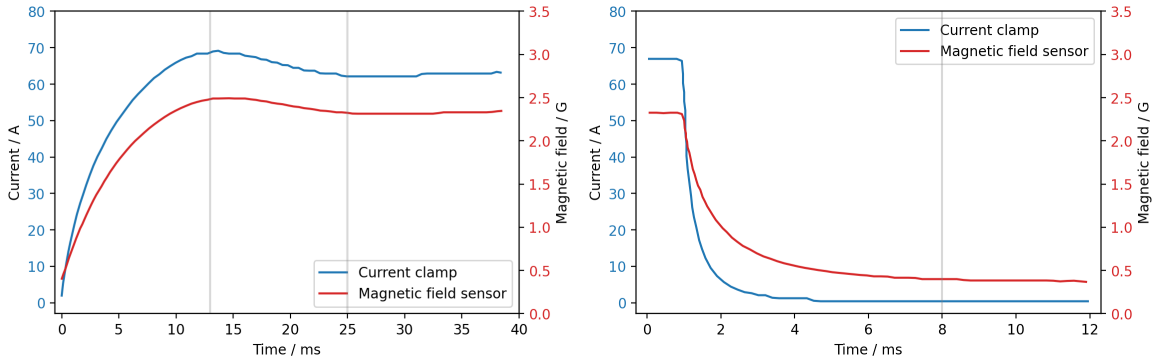

(a) (b)

Figure 3.23: Measured magnetic field response when instantaneously ramping the gradient between 0 G/cm and 130 G/cm with a magnetic field sensor (red) and a current clamp (blue). In **(a)** on can see the response when ramping the field up, where the maximum is visible at 13 ms and the field stabilizes after 25 ms. In **(b)** one can see the response for ramping down the magnetic field. It is turned off after approximately 8 ms. The offset from zero for the magnetic field measurement can be explained by the earth magnetic field. The data is measured using an oscilloscope and calibrated with [61, 62].

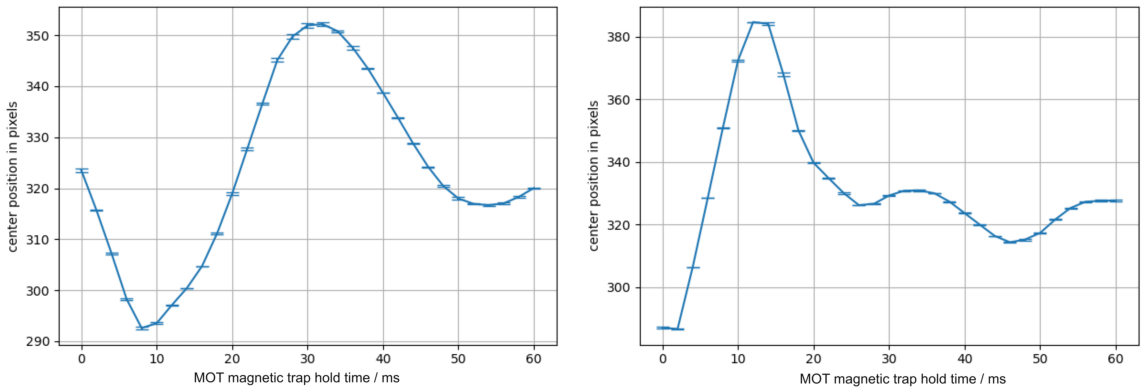

(a) (b)

Figure 3.24: Centre position of the atom cloud in camera pixels as a function of the holding time in the magnetic trap in the y-direction **(a)**, which corresponds to left-right, and in z-direction **(b)**, which corresponds to top-down in the laboratory coordinate system. An average over 2 measurement cycles is displayed, each time for MOT loading of 1 s, optical molasses for 5 ms, optical pumping of 20 µs.

atom collision.

In order to be able to see the impact the sloshing has on the temperature, a TOF measurement (see Section 3.2.1 for more details) can be performed after trapping the atoms.
To do so, the atoms are kept in the trap for 0.5 s, to make sure the sloshing is over, before turning the trap off and performing the measurement. Also since turning off the trap takes some time, the TOF measurement starts after 10 ms and not directly after turning off the trap. For this measurement, one does not have a look at the mean temperature but at the two temperatures for the different axes individually, Fig. 3.25(a) shows the y-axis (left-right) and Fig. 3.25(b) the z-axis (top-down).
Compared to after the optical molasses part, the temperature increased by roughly a factor of 10 due to sloshing of the atoms in the magnetic trap.

Also, the temperature for the top-down axis is even higher. Since turning on the trap takes some time, the atoms fall and are then kicked upwards again by the trap which results in stronger sloshing in the top-down direction (which can also be seen in Fig. 3.24) and therefore higher temperature of the atoms in that direction.

With the current setup it is not possible to fully counteract this, because it is not possible to turn on the MOT coil fast enough to trap the atoms immediately. Also, the fields can not be turned off fast due to eddy currents. To counteract that, it would be possible to use an additional large capacitor, which would charge up to the point where a fast turn-on of the coil is possible. Also, the exchange of the cooling blocks might reduce the eddy currents when turning off the magnetic fields.

In the future, it might be useful to introduce a possibility that allows for faster switching of the coils and therefore reduce the sloshing behaviour of the atoms in the trap. For now, the temperature of the atoms will be increased when trapping them but the atom number is still sufficiently high (in the order of $5 \cdot 10^8$) which is why no immediate changes on the system are planned to be implemented.

Further characterization of the magnetic trap with respect to the lifetime of the atoms in the trap is discussed in Appendix C.

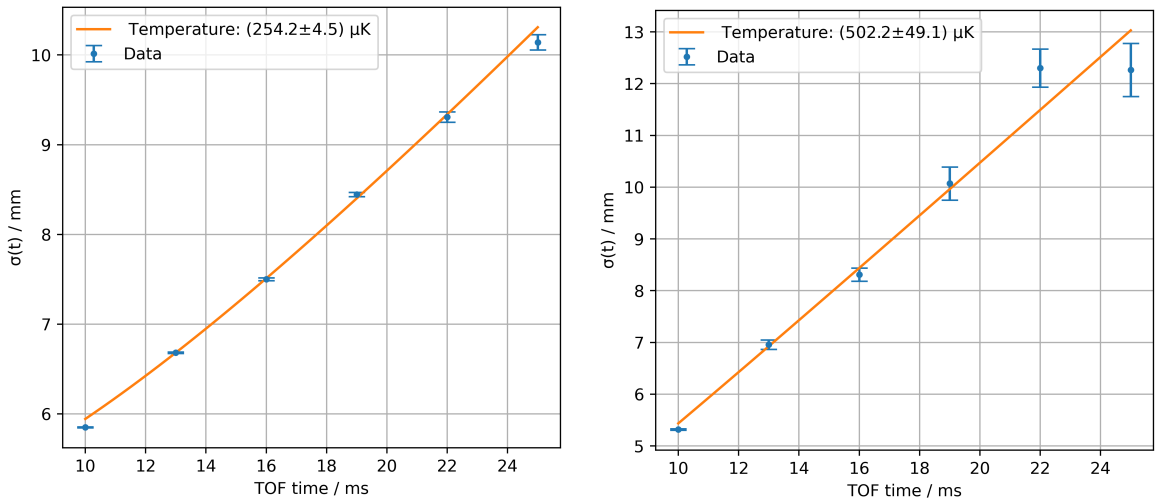

(a) (b)

Figure 3.25: Full width half maximum of the cloud expansion determined by a Gaussian fit to the summed density $\sigma(t)$ along the y-axis (left-right) **(a)** and along the z-axis (top-down) **(b)** as a function of the free expansion time of the cloud. The measurement was repeated for 37 times for a MOT loading time of 1 s, optical molasses for 5 ms, optical pumping of 20 µs, a holding time in the trap of 0.5 s and the average is plotted. The temperature was determined by fitting Eq. (3.3) to the data. The temperature increased by roughly a factor of 10 compared to after optical molasses due to sloshing of the atoms.

3.7 Imaging in Science chamber

In this section, the implemented absorption imaging system in the Science chamber (SC) is presented. The general working principle of absorption imaging can be found in more detail in Section 3.2.1.

The imaging system was first implemented by Johanna Popp in her master thesis [35]. A schematic of the optical setup is illustrated in Fig. 3.26. Absorption imaging in the SC is used for optimization of the magnetic transport, the final magnetic trap (see Section 3.8) and Rydberg excitation (see Chapter 4).

The reflected arm of DLpro3 is used as a light source which is already locked to the desired wavelength (see Section 2.2 for more details). The light is filtered with a PBS to ensure a high degree of linearly polarised light. Then a mirror converts the light from the x-lab frame axis to the z-axis where the light is circularly polarised by a QWP. This is implemented to drive the same closed cycle transition as for the imaging in the MOT chamber ^{87}Rb $|F = 2, m_F = 2\rangle \rightarrow |F' = 3, m_{F'} = 3\rangle$. The light then passes through the Science chamber in which the atoms are located after the transport sequence. The light is then guided back to the x-laboratory frame axis and captured on a CCD camera after a 0.5 magnifying telescope.

To ensure that the imaging in the science region can be used as a tool to optimize other parts of the setup, it needs to be optimized itself. In Fig. 3.27 the sequence is shown. After the atoms are transported to the Science chamber, they end in the final magnetic trap, illustrated in red with the control voltage applied to provide the set magnetic field gradient. As turning off the magnetic trap takes some time as discussed in Section 3.6 in more detail, this has to be taken into account when performing absorption imaging. To reduce that effect, the magnetic field gradient of the trapping coil is linearly reduced from 130 G/cm to 60 G/cm and then the atoms are kept in the trap for some time before it is turned off. Then, the light for the imaging is provided, here illustrated by the trigger signal

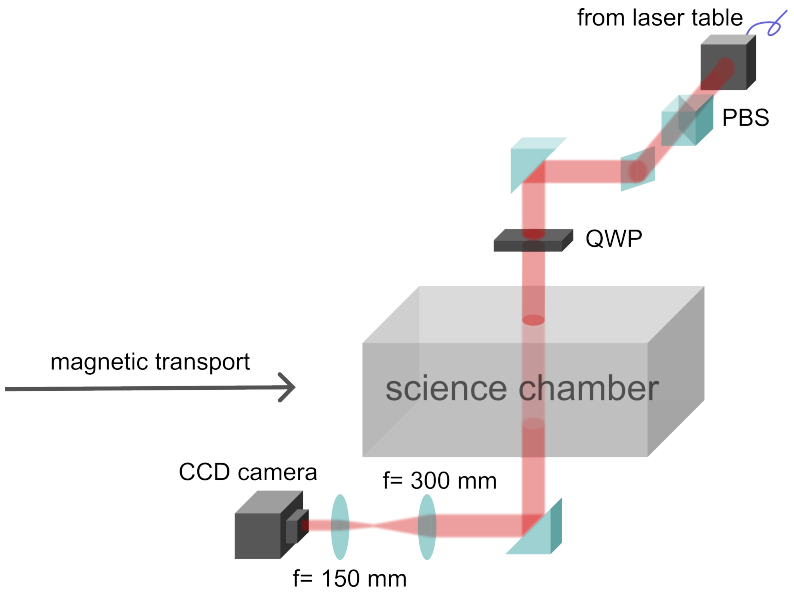

Figure 3.26: Schematic representation of the absorption image setup for the Science chamber. The setup is implemented from top to bottom so that it is perpendicular to the magnetic transport and the Rydberg excitation optics. The light is coupled out of a single mode fiber, polarization corrected with a PBS, circularly polarised with a QWP and imaged after the chamber with a magnifying telescope of 0.5.

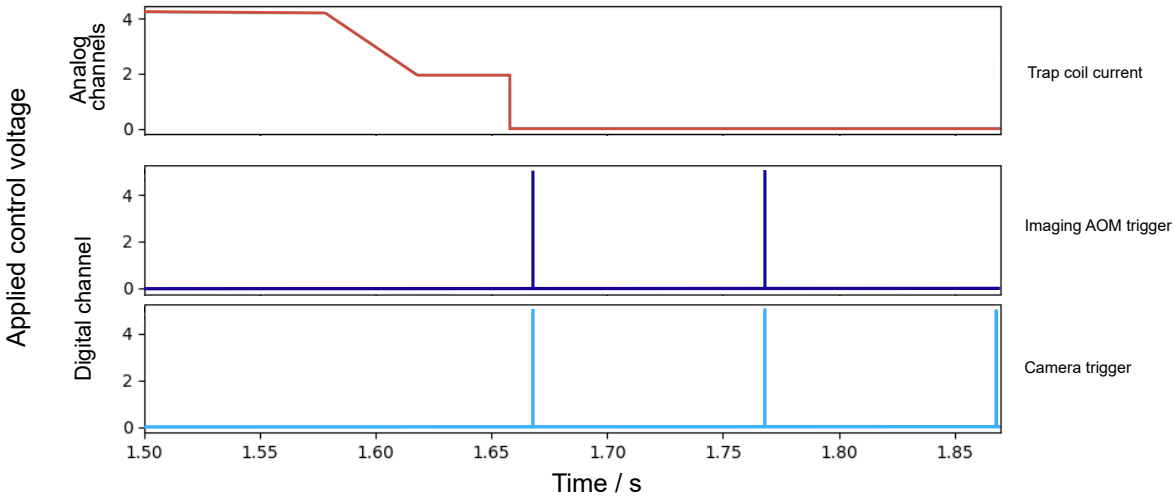

Figure 3.27: Simplified sequence used for performing absorption imaging in the Science chamber. The applied control voltage to the respective devices is displayed as a function of the time in the experiment. First, the atoms are transported to the Science chamber and trapped in the final magnetic trap (illustrated in red). Then, the magnetic field gradient is ramped down linearly to a smaller value to decrease the influence of eddy currents when turning off the trap later. After the trap is turned off, three images are acquired (imaging light and camera are triggered).

for the AOM in dark blue and then the images are taken (light blue).

The magnetic field gradient is turned off and bias fields are applied for the imaging sequence similar to how it was done for the imaging in the MOT chamber (see Section 3.2 for more detail on that). It takes some time for the magnetic fields to switch off (roughly 20 ms measured the same way as discussed in Section 3.6 for the MOT coils), which has to be compensated for with the bias fields. To make sure that we detect the atoms correctly, we perform a 2D scan of the detuning of the imaging laser (DLpro3) and the bias field that forms the quantisation axis for the imaging (bias field B_z in our laboratory coordinate system). This scan is performed in Fig. 3.28 for the case of no compensation in other directions by other bias fields.
It is important to note here, that the imaging optimization always takes place for a certain time of flight since the magnetic fields do not turn off immediately. The bias fields found only compensate the background field vectors for exactly that time after turning off of the coils which in our case is a TOF of 10 ms.

If the fields would be compensated and the quantisation axis has the correct direction, one would expect the measured atom number to be maximal whenever the detuning matches the Zeeman shift of the transition which is proportional to the applied bias field in z-direction B_z. However, if there is still a vector component of the magnetic field pointing in the wrong directions, a larger field in z-direction will align the quantization axis better with the beam which increases the absorption of the imaging beam. Here one can see that the atom number gets larger for larger quantisation bias fields B_z and detuning for DLpro3 (see Fig. 3.28) which indicates that the other two bias fields B_x and B_y have to be optimized first. These measurements are shown in Figs. 3.29(a) and 3.29(b). For this, a fixed B_z and imaging detuning are chosen and B_x and B_y are scanned to check which corresponds to the highest atom number. The values selected here are 4 MHz for the detuning and 3 G for the bias field

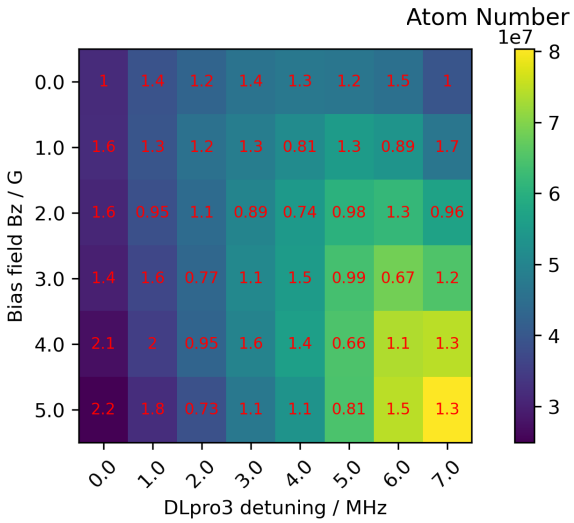

Figure 3.28: Atom number as a function of detuning of the imaging laser and the bias field applied for the quantization axis without correcting with additional bias fields in other directions. An average of 11 measurement cycles for a MOT loading time of 1 s, molasses of 5 ms, optical pumping of 20 µs and a magnetic transport duration of 1.5 s is shown. The red errors correspond to the relative errors in percentage. One can see highest absorption for large detuning and high bias field setting.

along the imaging axis. This is also expected since the Zeeman shift for 3 G can be found to be (with Eq. (3.5)) $(0.93\,\mathrm{MHz/G} \cdot 3 - 0.7\,\mathrm{MHz/G} \cdot 2) \cdot 3\,\mathrm{G} = 4.17\,\mathrm{MHz}$.

In Fig. 3.29(a) one can see that the atom number is highest for $B_x = 0\,\mathrm{G}$ and $B_y = 4\,\mathrm{G}$, but since it could get better for even smaller values of $B_x = 0\,\mathrm{G}$, the other direction was also scanned, which is shown in Fig. 3.29(b). This is realized by changing the current direction through the bias coils such that the magnetic field has the opposite sign. From the two scans, the optimum can still be found to be $B_x = 0\,\mathrm{G}$ and $B_y = 4\,\mathrm{G}$, which is why this value was chosen.

To confirm this choice of bias fields found and to check whether it has improved the imaging, the scan from the beginning (i.e. scanning the quantisation bias field together with the imaging detuning) must be performed with the new set of bias fields that has proven to be the most suitable. The following is shown in Fig. 3.30. One can see that there are several parameter sets that can be used to achieve the best imaging efficiency. This is also expected theoretically because depending on the set magnetic field for the quantization axis, the splitting due to the Zeeman effect changes. One would expect a slope of the form

$$\Delta_{\mathrm{DLpro3}} = 1.39\,\mathrm{MHz/G} \cdot B_z\,,$$

by rewriting Eq. (3.5) for the imaging transition with Δ_{DLpro3} being the detuning of the imaging laser and B_z the applied magnetic field for the quantization axis. This is also apparent in Fig. 3.30. For the following measurements, an imaging detuning of 2 MHz, a quantization bias field of $B_z = 2\,\mathrm{G}$ and $B_x = 0\,\mathrm{G}$ and $B_y = 4\,\mathrm{G}$ were chosen.

With the imaging system in the Science chamber being implemented and optimized, it is possible to characterize the magnetic transport in the following.

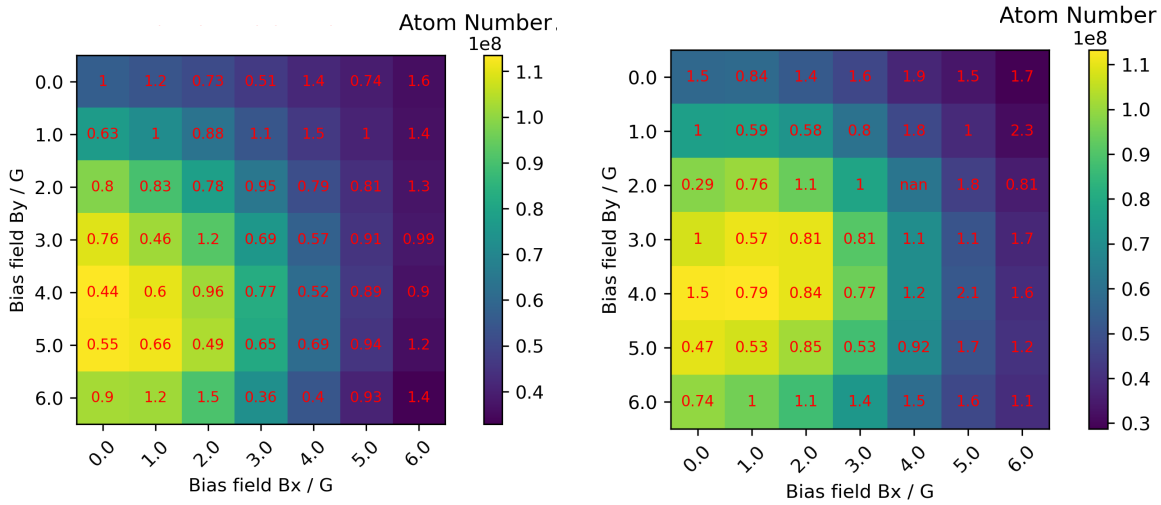

Figure 3.29: Atom number as a function of the bias fields B_x and B_y perpendicular to the imaging axis **(a)** and the same measurement again but with a different sign for B_x **(b)**. The average over 8 measurement cycles is performed under the same conditions as in Fig. 3.28. The highest absorption can be achieved for $B_x = 0\,\mathrm{G}$ and $B_y = 4\,\mathrm{G}$.

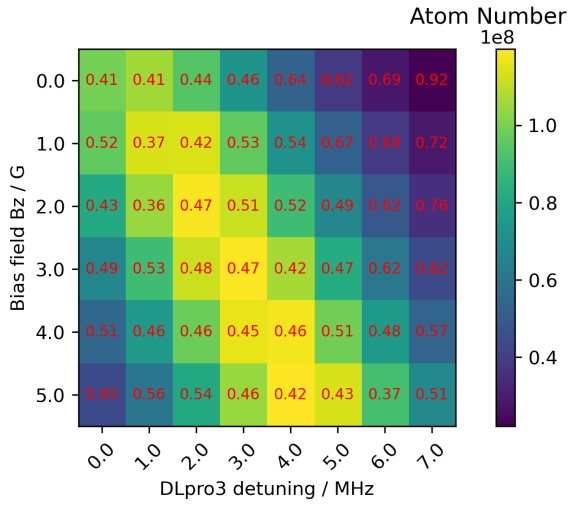

Figure 3.30: The atom number is shown as a function of the detuning of the imaging laser DLpro3 and the bias field generating the quantisation axis with the other bias fields being set. The average over 38 measurement cycles is displayed and the measurement was performed the same way as described in Fig. 3.28. Multiple sets of parameters lead to the highest absorption.

3.8 Transporting atoms from MOT to Science chamber

Once the atoms have been magnetically trapped in the MOT chamber, the next step is to transport them further into the experiment region, which in this experiment is done by a magnetic transport. It is possible to transport and trap neutral atoms optically as e.g. demonstrated in [63, 64]. However, to ensure that there is no heating, which could cause problems later when working with the cryogenic setup, a magnetic transport is chosen instead of an optical one.

The experimental implementation of the magnetic transport was designed by Cedric Wind and is based on the implementation done by Grainer et al. [34]. The working principle of the transport works as follows: The atoms are trapped in a magnetic quadrupole field generated by two coils in anti-Helmholtz configuration. The pairs of coils are arranged such that they partially overlap. When the current to one pair of coils used to trap the atoms is slowly turned off while the current of the next pair of coils is increased, the trapping field moves along the transport axis. By using three pairs of coils simultaneously, this can also be done more smoothly. A rough schematic of the transport sequence can be seen in Fig. 3.31, where the current applied to the respective coil pair is shown as a function of the transport distance. The atoms start in the MOT ($x = 0\,\mathrm{mm}$) and are then transported to the Science region over 45 cm with seven coil pairs in total. At the end of the transport the atoms are kept in the quadrupole field of the last coil pair (here: SC trap coil).

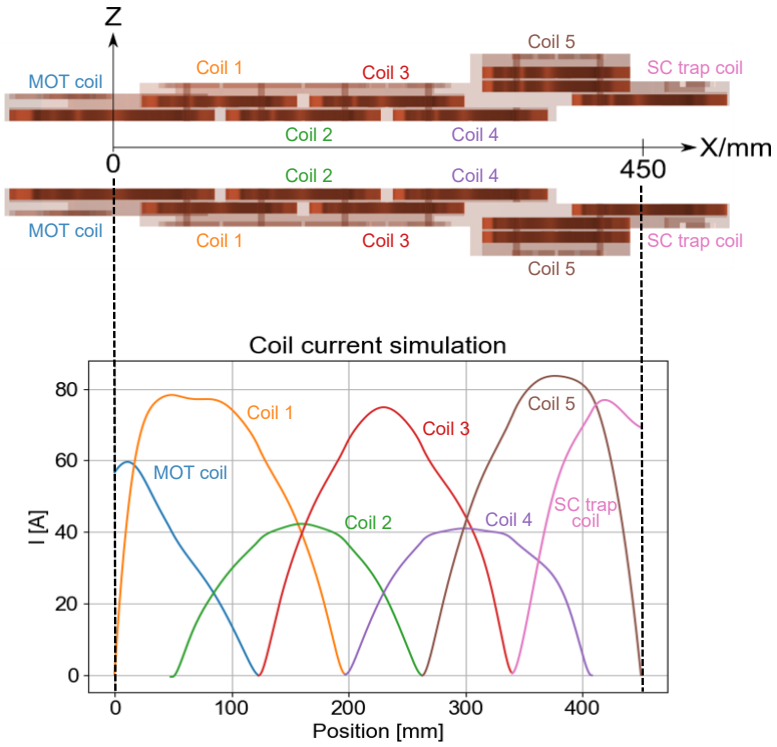

Figure 3.31: Sequence for magnetic transport made by Cedric Wind and modified. The applied current for the respective coil pair as a function of position over which the atoms are transported is displayed together with the respective coil schematic. The simulation as well as the design of the magnetic transport was done by Cedric Wind.

The magnetic transport needs to be very well aligned with the MOT position, the differential pumping tube and the final position for Rydberg excitation. This was done together with Johanna Popp, who wrote about it in more detail in her master thesis [35].

The magnetic transport uses a specific acceleration profile which was taken from [65] and implemented by Cedric Wind. Also profiles with constant speed or constant acceleration were tested but led to a worse outcome. Other, more complex transport profiles were not tested so far.

One of the free parameters for the chosen acceleration profile is the duration of the magnetic transport. Initially, a transport time of 1 s was used and an attempt was made to increase this to 1.5 s, which should improve the transport in terms of temperature and sloshing behaviour. To confirm this, the absorption imaging setup of the Science chamber was used (see Section 3.7 for more information) to perform absorption imaging in the final trap after the transport. In Fig. 3.32 one can see that the number of atoms remains about the same for both transport times, while the temperature could be improved by increasing the transport time. In x-direction the temperature could be improved from (252.6 ± 11.5) µK for 1 s transport time to (186.2 ± 3.0) µK for 1.5 s transport time. In y-direction, which corresponds to the direction of the magnetic transport, the temperature is higher in general.

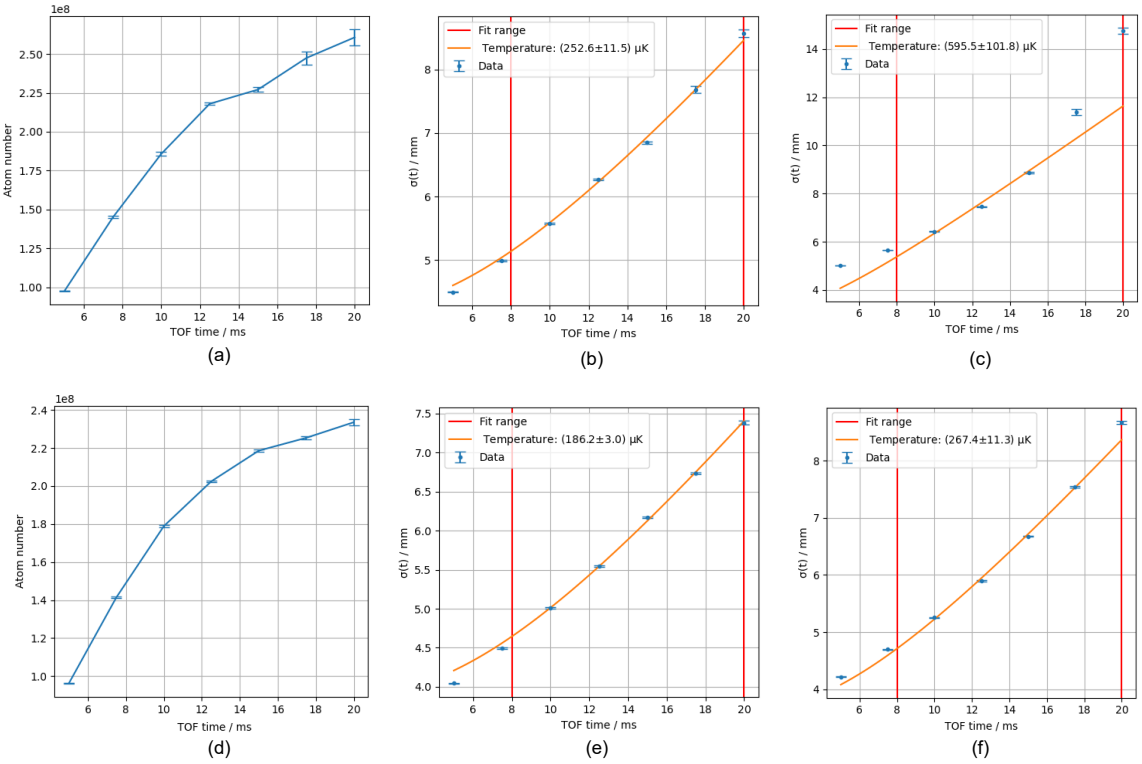

Figure 3.32: Atom number as a function of TOF time for **(a)** 1 s and **(d)** 1.5 s transporting time. Full width half maximum of the cloud expansion determined by a Gaussian fit to the summed density $\sigma(t)$ along the x-axis **(b, e)** and along the y-axis (magnetic transport axis) **(c, f)** as a function of the free expansion time of the cloud. In **(b, c)** one can see the temperature of the atoms after a transporting time of 1 s and in **(e, f)** one can see the temperature after a transporting time of 1.5 s. The average over six measurement cycles is plotted for a MOT loading time of 1 s, optical molasses for 5 ms, optical pumping of 20 µs. The fit ranges were chosen to start from 8 ms on as before that the magnetic field is not yet gone.

This is the case because in transport direction, sloshing occurs when the atoms arrive, especially for the shorter transport time of 1 s which is also why the fit does not work properly as the dynamics change due to the sloshing behaviour. With this one can see that it was possible to reduce the sloshing and the temperature of the atoms by increasing the transport time.

Other transport times were also tested but a time of 1.5 s led to the best outcome. Further optimization could be achieved by introducing a machine learning optimization package into the computer control, which was not done in this thesis.

After the magnetic transport, the atoms end up in the magnetic trap (i.e. the last coil of the transport sequence). At this point, the state preparation performed before trapping the atoms magnetically can be verified again. To do so, the same parameter scan as performed in Section 3.5 can be done (scan of the detuning and the power of the optical pumping laser) and check what parameter set leads to the highest atom number after the transport. This measurement presented in Fig. 3.33 shows a similar result as already found in Section 3.5 where a large range of parameter sets lead to a high atom number. The atom number differs from the atom numbers found in Fig. 3.32 because the measurements were taken at different times with different Rubidium background pressure in the MOT chamber. Nonetheless it was possible to find optimal values for state preparation before the magnetic transport. The values chosen are a detuning of 8 MHz and a power 290 µW which corresponds to an applied control voltage of 5 V displayed in the measurement Fig. 3.33.

With this it was possible to find optimal parameters for state preparation to guarantee for a high atom number in the Science chamber. Also, it was possible to reduce sloshing and thus the temperature at the end of the transport by increasing the time of the magnetic transport.

Further characterization measurements regarding the lifetime of the atoms in the magnetic trap and

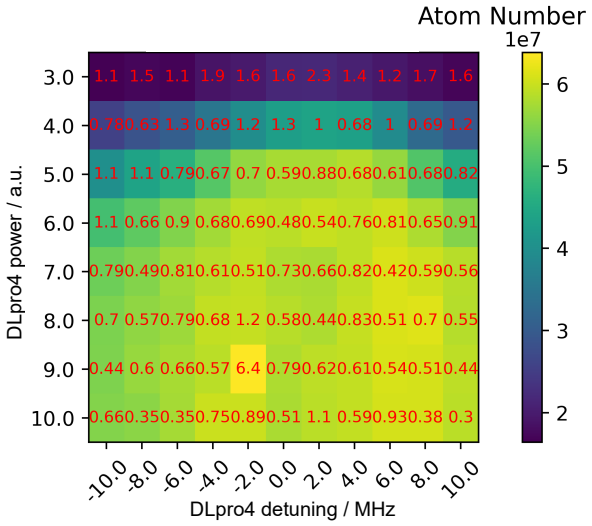

Figure 3.33: Atom number as a function of power and detuning of the optical pumping laser DLpro4. The measurement displayed is an average over seven measurement cycles and the red numbers are the relative error in percent. For each measurement, the MOT was loaded for 1 s, molasses was applied for 5 ms, optical pumping took place for 20 µs (and this is where the parameters were varied), then the atoms are trapped magnetically, transported for 1.5 s where they are imaged using absorption imaging in the SC (see Section 3.7) for a TOF time of 10 ms.

thus pressure in the SC compared to in the MOT chamber can be found in Appendix C.

In the future, the atoms are then loaded from the magnetic trap mentioned here onto a on-chip z-wire trap where also evaporative cooling will be implemented. This will then make it possible to confine the atoms at the desired position and cool them further.

With the atom preparation for the experiment being implemented with 10^8 atoms in the final magnetic trap in the science region, Rydberg excitation can be conducted which is discussed in Chapter 4.

CHAPTER 4

Rydberg excitation and detection

The Rubidium atoms are prepared and transported to the region where the experiment is about to take place. Also, the imaging in the experimental region was characterized such that it can be used for further characterization measurements.

The next step is to implement the Rydberg excitation and detection. With this, one of the two main ingredients of the final experimental goal - interfacing Rydberg atoms with an electromechanical oscillator - will be implemented in this experiment.

This implementation will now be talked about in more detail in this chapter.

For Rydberg excitation, the probe laser in the few photon regime drives the 5S $\rightarrow$ 5P transition while the control laser couples the intermediate state to a higher lying Rydberg state. In this experiment, the probe laser is at 780 nm and in the single photon regime and the control laser is at 480 nm and at roughly 100 mW.

First, I will talk about the requirements that have to be met to be able to perform Rydberg excitation in Section 4.1 and how these are implemented in the experiment.

This is followed by the explanation of the detection schemes that are implemented to make it possible to show that Rydberg excitation was performed. First, the few photon transmission spectroscopy is introduced in Section 4.2. Here, the integration of the detection scheme as well as some first characteristic measurements are shown. After that, also the ionization of Rydberg atoms and the detection of the respective ions as a different detection scheme is discussed in Section 4.3 in more detail.

4.1 Experimental requirements for Rydberg excitation

In Chapter 3 the atom preparation was implemented where the atoms are moved to the experimental region where Rydberg excitation and detection can take place. Before being able to implement the excitation in the experiment, some requirements have to be met experimentally, which will be discussed in more detail in the following.

- Correct wavelength and detuning of the control beam.
- Tightly focussed probe beam waist.
- Correct overlap of the probe light and the Rubidium atoms in the Science chamber.
- Overlap of probe and control light which should then automatically also overlap with the atom cloud.
- Integration of excitation and detection of Rydberg atoms into experimental sequence.

In the following, I will talk more about how the individual requirements are met in order to be able to implement Rydberg excitation and detection in this experiment. First, the setting of the wavelength of probe and control is mentioned in Section 4.1.1. Next, the probe optics setup is characterized such that it meets all requirements needed, one being the tightly focussed waist. This has to be done before setting up the optics around the chamber since only then the focus can be measured which is done in Section 4.1.2. After that, the setup is placed in its final position and the atom cloud is overlapped with the laser light in Section 4.1.3. Finally, the sequence used for Rydberg excitation and detection is explained in Section 4.1.4.

4.1.1 Correct wavelength of probe and control light

As a first step, one has to have a look at the wavelength of the two lasers as it is important to make sure that they address the correct transition.

First, we have a look at the probe laser at 780 nm. Since the imaging used in the Science chamber (for more details, see Section 3.7) takes place exactly at the probe transition of $|F = 2, m_F = 2\rangle \rightarrow |F' = 3, m_{F'} = 3\rangle$, the laser frequency and the detuning of the probe light are already known.

With this, one can have a look at the control light next. As mentioned in Section 2.2, the control laser is frequency locked using the PDH method. In this experiment, the locking point is generated by an external RF source which cannot be easily scanned without the laser falling out of lock. For this reason, it is not possible to scan the frequency of the control laser to find the optimum detuning during the sequence. However, the detuning of the probe laser can be scanned due to its different locking scheme (see Section 2.2 for more details on that). Before the detuning of the control laser can be fine-tuned, the wavelength must first be set to roughly the correct value. The theoretical wavelength to which we need to tune the laser to produce the $n = 68$ state is 479.66 nm[1]. Having tuned the wavelength to the expected theoretical value, one needs to fine-tune the wavelength to really find the transition, as the wavemeter may be off by a few MHz, which would be enough for us not to see any Rydberg atoms. To fine-tune the wavelength, we took advantage of real-time fluorescence imaging and the large cloud of atoms in the MOT region. Here it is much easier to see when Rydberg atoms

[1] determined with ARC [66]

are formed than just looking at absorption imaging in the Science chamber, where it is not even clear yet whether the beam overlap is sufficient (i.e. there could be several reasons for not seeing Rydberg atoms). The beam is directed to the MOT chamber and sent through the cloud. Then the wavelength is slightly tuned and the fluorescence is observed. For the transition where the fluorescence decreases, one has an indication of Rydberg atoms. This is the case because when performing Rydberg excitation on atoms no fluorescence (de-excitation from the intermediate state to the ground state) takes place.

4.1.2 Probe optics requirements and characterization

This section discusses the requirements, selection and characterization of the optics required for Rydberg excitation. Before the final setup around the Science chamber was built, the individual parts of the optics were selected and characterized so that they were sufficient for their respective purposes.

The Rydberg excitation optics must meet certain requirements for the experiment to work. First, it must be ensured that the focus of the probe light is small enough to allow a one-dimensional geometry to take advantage of the Rydberg blockade effect [67], which would be satisfied for a beam waist of about 10 µm or smaller as we are interested in principle quantum numbers of $n = 65$ and higher [23]. This might be interesting when interfacing a Rydberg super atom [68] with a quantum mechanical oscillator.

One also has to consider the geometry of the setup. The Rydberg excitation optics are chosen to satisfy not only the current room temperature setup, but also the future cryogenic setup, shown in Fig. 4.1. This shows the Science chamber for the cryogenic setup. One can see the inner and outer cryo-shields inside the Science chamber, leaving only a small optical access (top and bottom) for the Rydberg laser beams. The internal assembly of chip holder, mount and chip also leaves little room for beam divergence, as one does not want the light to hit the sample mount or the chip to create unwanted reflections. In Fig. 4.2 the calculated divergence for the probe and control light and the spatial constraints they have to meet (i.e. the chip on the chip holder) are illustrated. Different

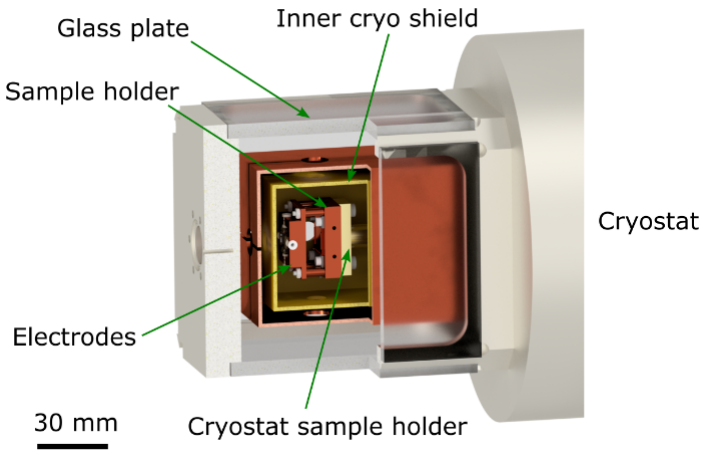

Figure 4.1: CAD drawing of the Science chamber region in the cryostat by Leon Sadowski [31]. The sample holder with electrodes in between the inner and outer cryo shield are shown. The light used for Rydberg excitation will pass through the glass plate (top and bottom) and the holes in the cryo shields which leads to spacial constraints for the propagating light.

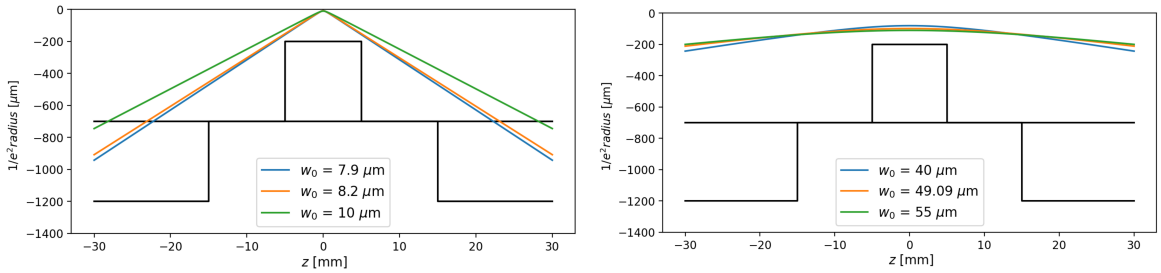

(a) (b)

Figure 4.2: Divergence of different beam radii ω_0 at the focus for **(a)** the probe light at 780 nm and **(b)** the control light at 480 nm with the dimensions given for the chip $(1.1 \times 1.1)\,\mathrm{cm}^2$ on top of the sample mount for a distance of 200 µm in between chip and focus.

focal points would be possible and here the optics are chosen so that the focal point for the probe is 8 µm (determined by Samuel Germer in his bachelor thesis [40]). The control is not as critical as this wavelength diverges less. We also want the focus to be larger than for the probe light to make overlapping easier, so I chose an asphere with a focal length of 6.24 mm (TL A110TM-A, $f = 6.24$ mm Asphere) as the out-coupling lens for the control light, resulting in a waist of 50 µm in the center of the chamber.

With the known requirements, one needs to take a closer look at the optics required. The two lasers used for the Rydberg excitation scheme are the DLpro3 as the probe and TASHGpro1 as the control laser. The laser system is discussed in Section 2.2. The optics used are presented in more detail in Fig. 4.3. First, the probe light is coupled out of the fiber, passes through a linear polariser, is circularly polarised by the combination of a HWP and a QWP to drive $|5S_{1/2},\ F = 2,\ m_\mathrm{F} = 2\rangle \rightarrow |5P_{3/2},\ F' = 3,\ m_{\mathrm{F}'} = 3\rangle$ and then focused into the chamber by an achromatic lens. The transmitted light is linearly polarised by another set of a HWP and a QWP and detected by a single photon counter module (SPCM). Since the probe laser is the more critical one (smaller needed waist and more divergence due to the wavelength), it is investigated in more detail than the control beam. The control light is also circularly polarized to drive the $|5P_{3/2},\ F' = 3,\ m_3\rangle \rightarrow |68S,\ m_\mathrm{J} = \frac{1}{2}\rangle$ transition.

For testing purposes of the probe optics, the setup was not placed directly around the Science chamber, but on a laser table with two glass plates acting as replacements for the windows of the Science chamber. This was done to characterize the setup to make sure it would work as expected around the Science chamber. Also, it is not possible to measure the beam waist and shape later because the waist position would be inside of the vacuum chamber.

Most of the optics were chosen during the course of Samuel Germer's and Valerie Leu's bachelor thesis [40, 69], with Samuel Germer focusing on the best possible beam shape for the probe beam and Valerie Leu characterized the polarization of the probe setup. I assembled the complete setup, combining the knowledge from the previous two thesis on the laser table with the components found, and tried to limit it to the dimensions that would be required in the actual setup. This also led to a reconsideration of the previously planned setup for coupling the light into the SPCM, as this setup was too large and needed to be made smaller. Instead of a telescope consisting of two lenses, a single achromatic lens was chosen. Also, a new lens mount for the focusing lens for the light into the chamber, with a translation stage for fine tuning the lens position, introduced at the end of Valerie Leu's thesis [69], is implemented in the setup. The main focus of the characterization and optimization of the test

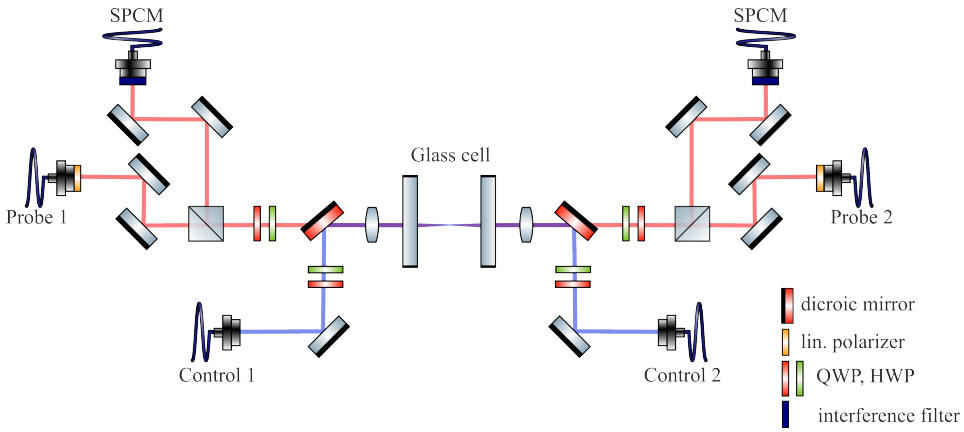

Figure 4.3: Optics used for Rydberg excitation. The light provided by the DLpro3 serves as the probe light, which is fed into the setup, polarization corrected with a linear polarizer, circularly polarised with a HWP and a QWP, and focused so that the waist at the center of the cell is approximately 8 µm. The transmitted light is then passed to the Single Photon Counter Module (SPCM) arm on the other side, where it is detected. The control beam provided by the TASHGpro1 at 480 nm is superimposed on the probe light by a dichroic mirror and focused down to about 50 µm at the waist. The setup is built such that both counter- and co-propagating probe and control light would be possible.

setup was to check the focus again with the complete setup in place, as this cannot be done after the setup has been built around the Science chamber. The focus was measured with a camera and fitted with a Gaussian beam profile as set up by Samuel Germer in his bachelor thesis [40]. The measured data can be found in Fig. 4.4. With all the optics in place, the beam waist is slightly larger than the theoretical 8 µm as it can be seen in Fig. 4.4, but since it still meets the requirements, it should be sufficiently small. There is also some astigmatism (different position of the focus in the horizontal and vertical plane), which could be improved by changing the height of the lens by inserting spacers. The next step is to see how well the position of the second lens can be adjusted. This is done by checking how well it is possible to couple the light from one side of the chamber to the opposite

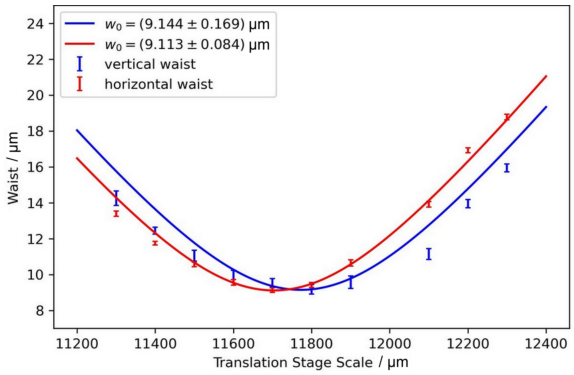

Figure 4.4: Measured horizontal and vertical waist of the probe beam along the beam axis is a bit larger than the theoretical 8 µm but meets the requirements. Slight spherical aberrations (asymmetric around the focus) and astigmatism (different positions of focus) are visible which could be reduced by changing the height of the lens in the new lens mount.

side (which has the same set of lenses), thus checking the collimation achieved by the second lens. Finally, the coupling into the SPCM arm is also optimized to get an idea of what can be expected in the actual setup. It was possible to achieve a probe-to-probe coupling of 61%, and a probe-to-SPCM arm coupling of 73%. This will provide a reference for setting up the optics around the actual Science chamber.

4.1.3 Overlap of probe/control light and Rubidium atoms

From characterizing the probe setup, one now knows that the beam waist is in the order of 9 µm. The next step is to set up the probe setup around the Science chamber and check that the light overlaps with the atom cloud. As the probe light is the reference axis to which the whole setup is aligned, one does not want to change its position. Therefore, the position of the cloud must be changed to maximize the overlap between the probe beam and the atoms. This can be done by changing the bias fields in the Science chamber. The sequence used to image the position of the atoms relative to the probe beam is shown in Fig. 4.5.

Once loaded, the atoms are transported into the science chamber. When the atoms arrive at the final magnetic trap (shown in red), the pulse generator (green) is switched on. The pulse generator acts as a trigger signal for the probe light, and in this case a pulse of resonant probe light is used. After this pulse, absorption imaging is performed as described in Section 3.7 which is illustrated by the trigger signals for the imaging light and the camera (i.e. the respective applied control voltage which acts as a trigger for the devices). This measurement is carried out with the probe beam by switching on the

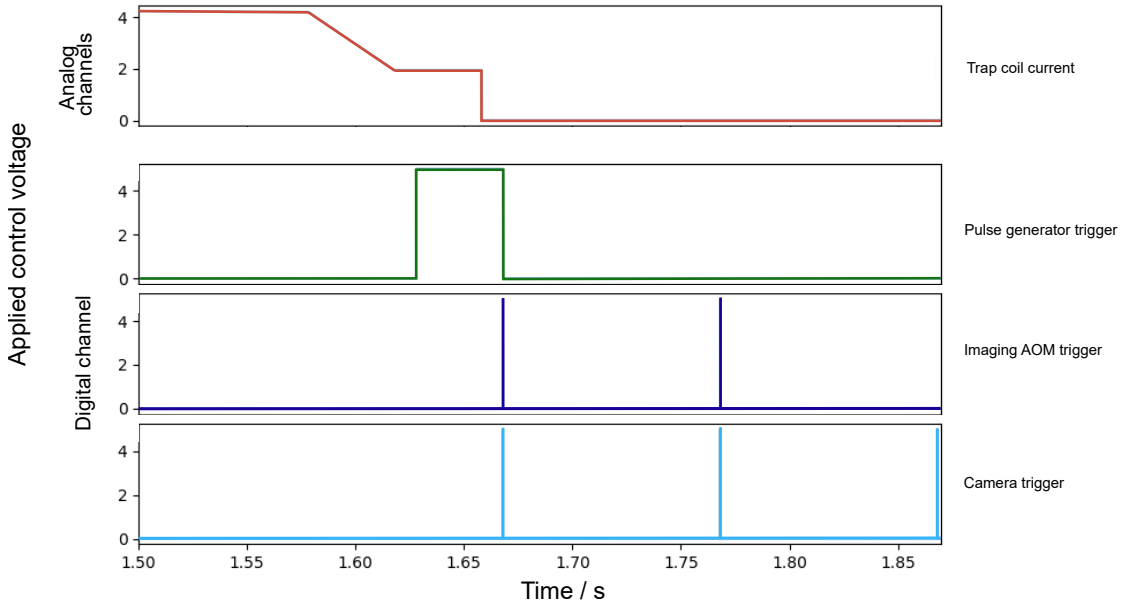

Figure 4.5: Sequence used for imaging the atom cloud after one resonant pulse of probe light. Here, the most important steps are illustrated. After transporting the atoms to the Science chamber, the atoms are hold in position by the magnetic trap in the end (red). Then, the pulse generator is turned on (green) which in this case provides one pulse of probe light and afterwards the atoms are imaged with absorption imaging in the science chamber.

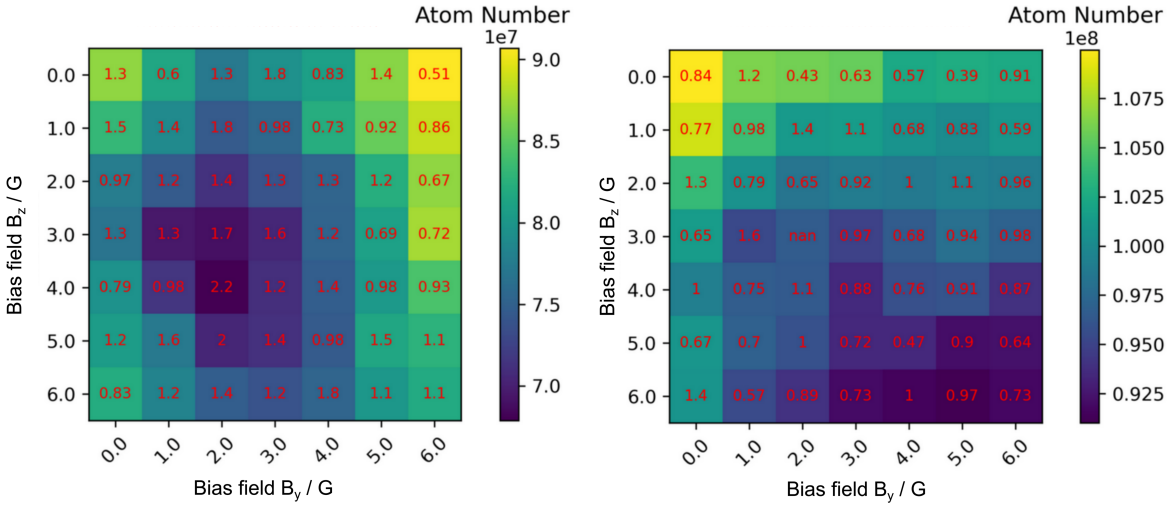

Figure 4.6: Measured number of atoms as a function of the bias fields (B_y, B_z) perpendicular to the probe beam is averaged over 10 measurement cycles each with the red numbers corresponding to the relative errors in percentage. **(a)** shows the atom number taken with absorption imaging after one probe pulse has taken place while **(b)** shows an absorption image of the atoms without a previous probe pulse. The difference of the atom number without and with pulse generator is plotted in Fig. 4.7 where the bottom right picture is the result of these two.

pulse generator (see Fig. 4.6(a)) and without (see Fig. 4.6(b)) by switching off the pulse generator but keeping the sequence exactly the same. This is done to be able to subtract the two measurements to see the effect of the probe pulse in Fig. 4.7. Here, the probe light saturates the atom cloud leading to the atoms not being detected with the absorption imaging any more. When taking a measurement without the probe light and then subtracting the measurement with probe light, that leads to a positive difference in atom number where the cloud was saturated by the probe light. The bottom right figure corresponds to the two measurements explicitly shown in Fig. 4.6. The other three are conducted in the same way. As the bias coils can only take positive applied control voltages corresponding to a specific current and cannot be changed during a measurement, different bias coil polarities were set, resulting in the four plots shown for all possible combinations. Looking at these plots it is easy to see that the atoms are approximately in the center. From this one can see that the overlap of the atom cloud and the probe light is guaranteed for different bias field configurations. This measurement not only provides information on the best possible choice of bias fields, but also gives a rough idea of the size of the atom cloud. Since the applied gradient was 30 G/cm and the cloud appears to be about 6 G, the atom cloud can be estimated to be about $\frac{6\,\mathrm{G}}{30\,\mathrm{G/cm}} = 2\,\mathrm{mm}$.

Next, the probe and control light need to be superimposed to allow Rydberg excitation. This is done roughly by eye, making sure that the beams overlap on the lenses in front of the Science chamber. Once the Rydberg detection is implemented and a rough signal is found, the detuning of the control light and the overlapping of the probe and control light can be further optimized.

This is now the starting point with which one can work since now the light and the atoms are overlapped and with this, Rydberg excitation can take place. To make this possible, next one has to implement the excitation and detection scheme into the experiment control sequence which is

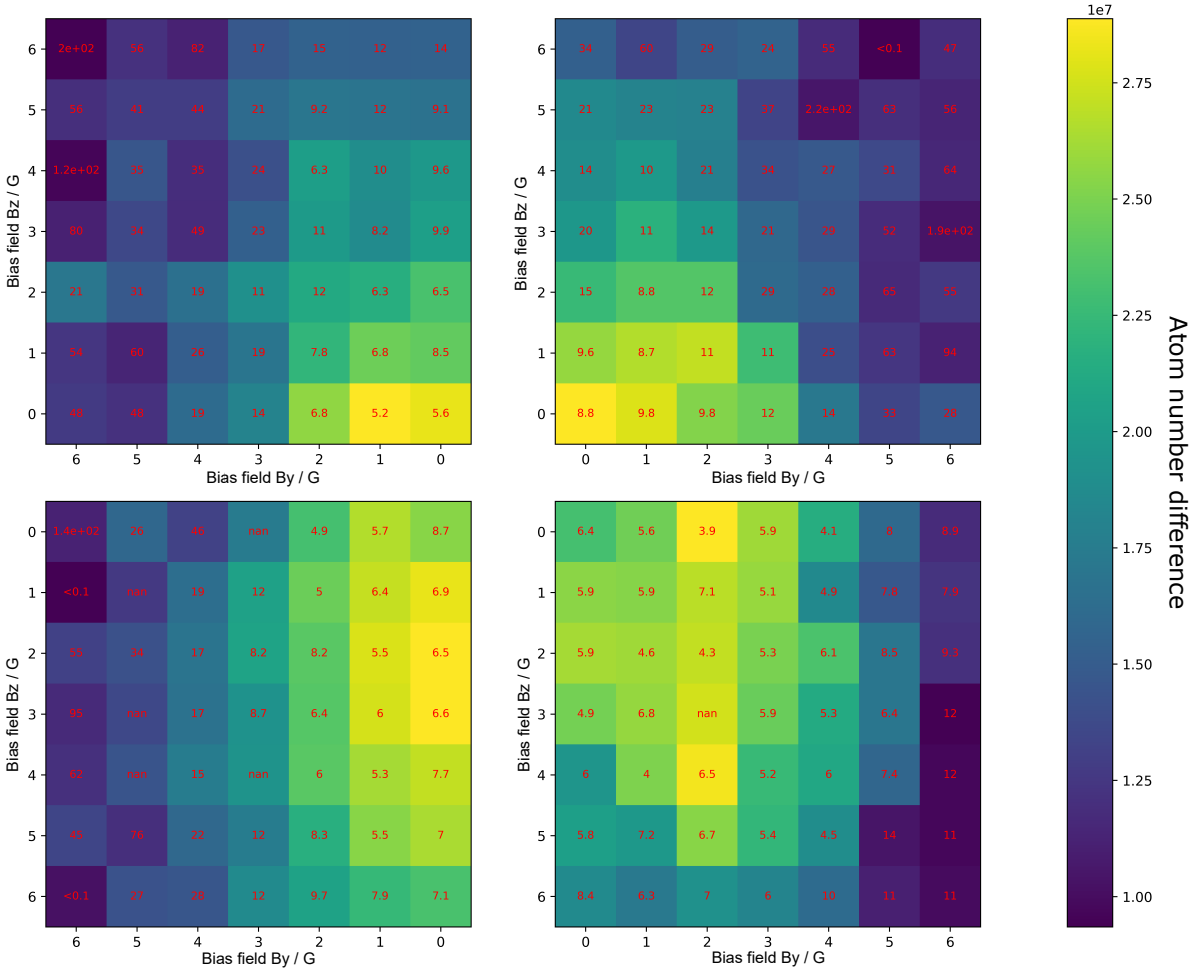

Figure 4.7: Measured atom number for a measurement with probe light which saturated the atom cloud and one without probe light as done in Fig. 4.6. By subtracting these two measurements, one can find a higher difference in atom number where the probe light saturated the atom cloud. This was done for all possible fields of bias coil configuration. Since the coils can only be set to positive values, the current through the coils was switched such that all possible configurations could be mapped out.

explained in the following.

4.1.4 Experimental sequence for Rydberg excitation

The last requirement that has to be met to be able to perform Rydberg excitation is its integration into the experimental sequence, which is described in this section in more detail. The sequence used for Rydberg excitation and detection is illustrated in Fig. 4.8.

First, the atoms are prepared in the final trap which is illustrated in blue by the applied control voltage to the power supply for the coil currents. During the atoms are trapped, the pulse generator is triggered (illustrated in green). The pulse generator itself acts as a triggering device for the pulses needed to perform Rydberg excitation and detection. Here the first 1000 pulses take place with the

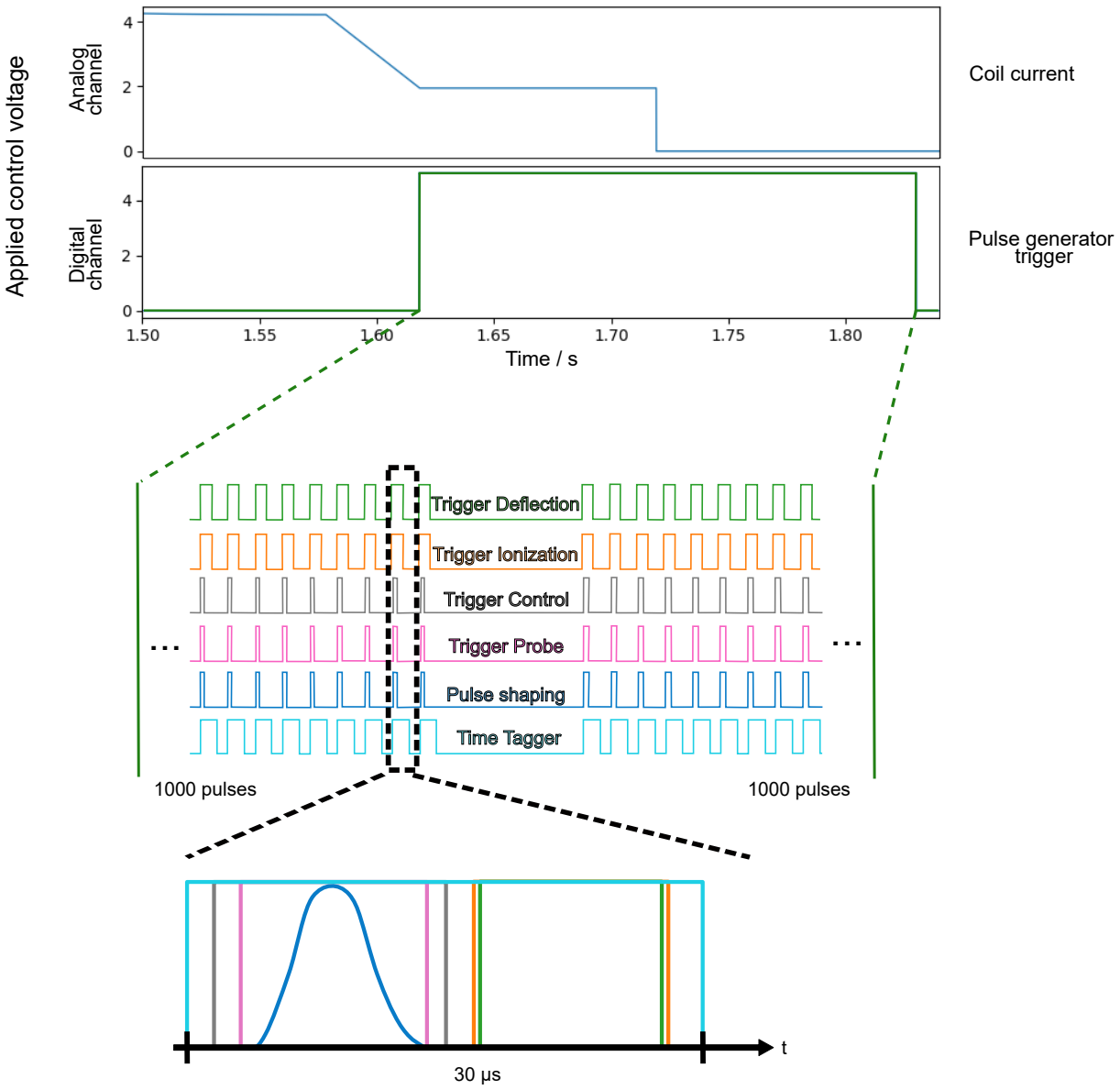

Figure 4.8: Sequence illustrating the excitation and detection of Rydberg atoms. The atoms are sitting in the final trap when the Rydberg sequence triggered by the pulse generator takes place. The pulse generator triggers 1000 pulses with atoms and another 1000 pulses without atoms (when the trap is switched off, i.e. the applied control voltage to the trap coil power supply is set to zero, the atoms are lost). Finally, there is a zoom in on one of the 2000 pulses containing the trigger for Probe and Control to perform the Rydberg excitation, shape the probe light and count the signal with the Time Tagger.

atoms trapped in the magnetic trap, then there is a pause while the trap is switched off and the atoms are lost (for 10 ms). Then there are another 1000 pulses, which serve as a background measurement without atoms.
The 1000 pulses are not shown to scale, just to give a rough idea of how this is done. The final zoom-in

shows one of the 2000 pulses as a rough sketch. The Rydberg excitation sequence consists of switching on a trigger for the control light (grey) and probe light (pink) for Rydberg excitation and a trigger for shaping the probe pulse (dark blue). These are the pulses that are used for the excitation. For the detection, other pulses are applied which are the trigger for the ionization (orange) and deflection (green), which are needed when using ionization detection of the Rydberg atoms. Also, the trigger for the Time Tagger (light blue) is shown, which is the counting device for both, the detection of transmission spectroscopy as well as ionization detection. This will, however, be discussed in more detail in the respective Sections 4.2 and 4.3.

After introducing the rough sequence, I want to talk about the additional hardware required to enable Rydberg excitation. In particular, the equipment needed to generate the probe and control light pulses and to shape the probe pulse are introduced as these are the three pulses needed to perform the excitation step.

To make this possible, a pulse generator[2] is used to trigger the light pulses for probe and control. This allows the number, start time and duration of the pulses to be varied according to what is required for the specific experiment. The timing and duration of each pulse can also be set independently. It is also possible to perform multiple repetitions of pulses in rapid succession.

The pulse generator also acts as a trigger for the function generator, which is used to change the shape of the probe pulse. In general, the shape of the pulse is important because we are working with coherent pulses that are attenuated to the level of a few photons. It is therefore important not to have a sharp edge, as this would result in numerous frequency components in the Fourier space. It is also important to be able to shape the pulse according to the purpose. For some experiments a Gaussian shape is preferred, while for other purposes other pulse shapes are more favourable (e.g. a Tuckey pulse as a compromise between a Gaussian and a flat-topped pulse, as used for the single Rydberg superatom in [71]). The probe pulse is shaped by applying a control voltage from the function generator onto the AOM through which the probe light passes. Fig. 4.9 shows the power in the first

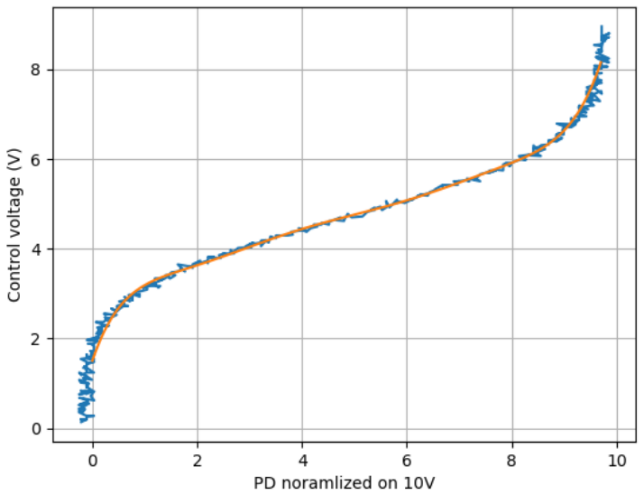

Figure 4.9: Measured power in the first order after an AOM on the photo diode as a function of input control voltage, which is plotted inverted here. With this, it is possible to fit the curve with a polynomial of fifth order to provide a specific control voltage as a function on the power one wants to have after the AOM.

[2] developed by Felix Engel in his bachelor thesis [70]

order diffracted beam from an AOM through which the probe light is guided as a function of the applied RF power to the AOM. The output intensity is measured with a photo diode and the applied RF power is controlled with a control voltage between 0 V and 10 V (corresponding to the maximum input range). The intensity is nonlinear in RF power. To compensate for that, the signal is inverted to find a control voltage as a function of power after the AOM and a calibration curve is determined. By applying this calibration to the function generator, it is possible to compensate for the nonlinear response of the AOM. In Fig. 4.10(a) the AOM power output without calibration and in Fig. 4.10(b) what it looks like with calibration are illustrated. The (red) trigger pulse from the ADWIN digital output turns on the function generator, which provides a Tukey pulse (blue; a Tuckey pulse was chosen as an example here, also other pulse shapes are possible), resulting in a power output shown in green. After calibration, the signal from the function generator looks slightly different, resulting in an AOM output with a flatter peak, closer to the desired Tukey pulse shape. For the second measurement, the power has been reduced so that both the input signal provided by the function generator to the AOM and the power output from the AOM are smaller in amplitude. Depending on the specific purpose, one has to set the amplitude accordingly in the later experiment.

The pulse generator is also used to trigger the Time Tagger, which allows time-resolved counting of pulses, such as the signals detected by the single photon counter modules or the micro channel plate for ionisation, both of which will be discussed in more detail in Sections 4.2 and 4.3. This makes it possible to measure consecutive cross correlations, lifetime measurements and much more [72]. To measure with the Time Tagger, the device is triggered by the Pulse generator which starts the measurement process. Then, the device measures the time difference between the trigger and all clicks from the connected devices and stores them in a histogram. The number of bins as well as the bin time of the histogram can be set depending on what is needed in the experiment. This is described in more detail in [73].

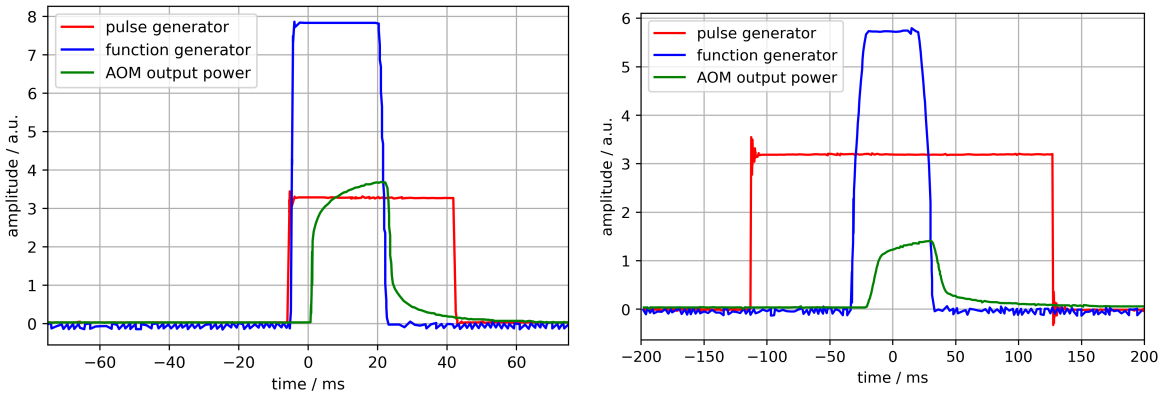

(a) (b)

Figure 4.10: Amplitude of the pulses as a function of time for shaping the probe pulse. In red one can see the trigger pulse from the pulse generator that turns on the function generator. In blue, the signal from the function generator applied to the AOM is plotted and in green one can see the power response of the AOM. **(a)** shows the AOM power output without calibration of the AOM response curve and **(b)** shows the output with calibration. For the second measurement, the power was reduced, so the amplitude for both, the input signal to the AOM and the output signal, are smaller.

The timing of the ionisation electrode and the deflection electrode is also controlled by the pulse generator. This means that most of the actual Rydberg excitation sequence is controlled by the pulse generator and not by the digital channel breakout box, which is used to generate the TTL pulses for the atom preparation.

4.2 Transmission spectroscopy

The use of single photon counters opens up the possibility of detecting Rydberg excitation via single photons. This can be achieved using Electromagnetically Induced Transparency (EIT, for more details see Section 4.2.4) [74], which creates a collective matter-light interaction, i.e. Rydberg polaritons (for more details see [75]). One can then do few photon transmission spectroscopy, which is used to detect EIT, using Single Photon Counter Modules (SPCMs), i.e. detecting the photons that pass through the medium indicating that the intermediate state was coupled to a high lying Rydberg state.

First, I will talk about the implementation of the SPCM used for the room temperature experimental setup and the dark count rate as a first characterization of the setup in Section 4.2.1. Then I will talk about the theoretical transmission spectrum one would expect in our experiment in Section 4.2.2. This is followed by first few photon transmission measurements for probe light without coupling the intermediate state to a Rydberg state (see Section 4.2.3). And finally, some first probe transmission measurements with the intermediate state being coupled to a high lying Rydberg state are presented in Section 4.2.4.

4.2.1 Implementation and characterization of single photon counters

This section discusses the implementation of single photon detection in more detail. Firstly, the principle of operation of the device currently in use will be briefly explained. Then, some important steps that have to be taken to ensure that the counter don't get damaged are discussed. Finally, the implementation of a first measurement scheme to determine the dark count rate is presented in more detail. The sequence used to perform Rydberg detection using a SPCM is the same as introduced previously for Rydberg excitation in Section 4.1.4.

Implementation of SPCM into experimental setup

Before discussing the implementation of the single photon counter modules in the current room temperature experiment, it should be noted that this selection of the used Single Photon Counter Modules (COUNT-250C-FC from Laser Components) is not the device that will be used in the final cryogenic setup. It will only be used to complete the first implementation of Rydberg excitation and detection. In the future, superconducting single photon counter detectors (The Single Quantum EOS from Single Quantum) with better performance will be used. The reason for the choice of different SPCMs for the time being is that not all components are available at the time of this work. Also, the current setup consists of only a single counter module, making correlation measurements impossible. This will change when the new system with multiple detectors is integrated. Nevertheless, it is still possible to prove the existence of Rydberg excitations and to make some first characterization measurements of the atom cloud.

The SPCM is connected to the optical fiber used to measure the spectroscopy signal of the probe light through the atom cloud. The light hits an avalanche photo diode, where electrons are created by the photoelectric effect. The signal is then amplified by a photomultiplier, resulting in measurable electrical pulses at an anode, as described in more detail in [76, 77]. This signal can then be sent to the Time Tagger, which counts the number of events for a given time interval.

As the single photon counter can easily be damaged if the count rate sent to the counter is too high (the maximum count rate for the counter used is given as 20 MHz [78]), it is important to

attenuate the probe beam sufficiently. This is done by measuring the probe power in front of the chamber and determining the required attenuation. For the current setup, the power in front of the chamber is 15.9 mW, which corresponds to a count rate of about $R = \frac{15.9\,\mathrm{mW}}{h\nu} \approx 6.25 \cdot 10^{16}$ Hz. This allows us to determine the minimum OD value needed for the neutral density filters, which is $\mathrm{OD} > -\log_{10}\left(\frac{R_{\max}}{R}\right) \approx 9.5$. The filters were selected accordingly. The filters were placed on the laser table in front of the fiber coupling to the experiment. This is because neutral density filters can distort the beam profile, which can be compensated by coupling into the single-mode fiber afterwards.

Another precaution was to ensure that no control light entered the counters. In typical experiments, the control light has more power and even a small back reflection could destroy the counters. To prevent this from happening, a narrowband 780 nm interference filter (FL780-10 from Thorlabs) with an OD of 4 at 480 nm (the wavelength of the control light) was placed in front of the SPCM coupler.

Finally, the fiber-coupler itself was covered with black tape to prevent stray light from entering the fiber, and the fiber was also insulated with aluminium foil to prevent light from entering through the fiber cladding.

Next, the SPCM is integrated into the experimental sequence discussed in Fig. 4.8. For this, the SPCM is connected to the counting device (the Time Tagger). This makes it possible to count the single photons that are detected with the SPCM.

Dark count rate measurement

As a first measurement to test the setup, the dark count rate of the SPCM is measured, as this can be compared with the value given by the manufacturer to get a first idea of the measurement process and it is important to know for later evaluations. The probe control sequence in Fig. 4.8 is used. However, the probe and control lights are blocked, as we are only interested in the dark counts for this measurement. The blocking consists of placing a piece of paper in front of the coupler where the light is coupled into the fiber connected to the SPCM. With this it is then possible to measure the number of counts per pulse as illustrated in Fig. 4.11(a). Here, every data point being averaged over 1000 measurement pulses and 4 measurement cycles. This whole cycle of atom preparation and 1000 pulses resulting in a data point is performed 100 times (indicated by the dummy iterator "Iterator" on the x-axis). Four complete measurement cycles containing 100 measurements with 1000 pulses were performed. For better visualisation, the measured number of photons in one pulse for a dataset of 800000 pulses is visualized in a histogram in Fig. 4.11(b). From this the mean photon number per pulse can be determined to be $(1.28 \pm 0.01) \cdot 10^{-2}$. This value can be used to determine the dark count rate. In the case of this measurement, the number of bins for the Time Tagger was 5050 with a bin time of 0.02 µs (for more details on that, see Section 4.1.4), which corresponds to a measurement time of $5050 \cdot 0.02\,\mu\mathrm{s} = 101\,\mu\mathrm{s}$, giving a dark count rate of $\frac{(1.28\pm0.01)\cdot10^{-2}}{101\,\mu\mathrm{s}} = (126.73 \pm 1.19)$ Hz. If we compare this result with the manufacturer's characterization of 139 Hz (taken from the characterization sheet), the measured value is lower, but in the same order of magnitude. This might be the case because of the different setup that was used to specify the dark count rate compared what was set up in our experiment. Nonetheless it shows that it is possible to work with the SPCM in the way it is implemented in the sequence.

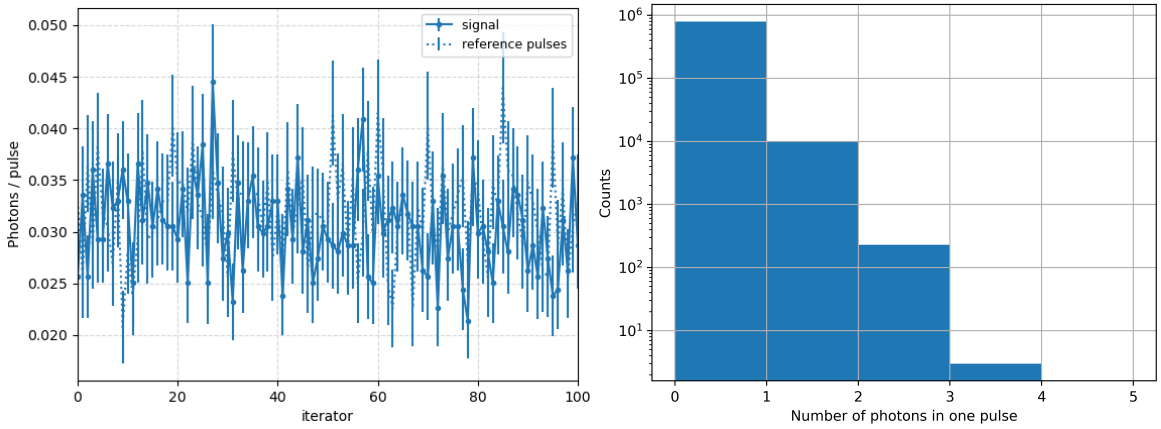

(a) (b)

Figure 4.11: **(a)** Number of photons per pulse for measuring the dark count rate with every data point being averaged over 1000 measurement pulses and 4 measurement cycles. One hundred data points were taken under the same conditions ("iterator" just being a dummy-iterator). For a better visualisation, the absolute number of photons measured in one pulse is plotted in a histogram in **(b)**. From this, the mean photon number per pulse for the dark count rate can be determined to be $(1.28 \pm 0.01) \cdot 10^{-2}$.

4.2.2 Optical density of atom cloud

The next step is the implementation of the few photon transmission spectroscopy from which the optical density for probe photons of the atom cloud can be determined. The optical density within the blockade region $\mathrm{OD_b}$ is one of the key parameters in any application of Rydberg nonlinearities [75].

For deriving the optical density, one needs to start of with describing the system which in this case can be done with the Lindblad master equation of the form [79]

$$\dot{\rho} = -\frac{i}{\hbar}[H, \rho] + \sum_i \gamma_i \left(L_i \rho L_i^\dagger - \frac{1}{2} \left\{ L_i^\dagger L_i, \rho \right\} \right) , \tag{4.1}$$

with H being the Hamiltonian of the system, $\{L_i\}_i$ describes dissipation of the system, γ_i are the damping rates and ρ is the density matrix of the system [80]. In our case, we are interested in a two level system with decay from the excited state to the ground state. For this case, one can re-write Eq. (4.1) for the specific case to

$$\dot{\rho} = -\frac{i}{\hbar}\Bigg[\underbrace{\begin{pmatrix} 0 & \Omega_P/2 \\ \Omega_p/2 & -\delta \end{pmatrix}}_{H_{2\,\text{level sysyem}}}, \underbrace{\begin{pmatrix} \rho_{11} & \rho_{12} \\ \rho_{21} & \rho_{22} \end{pmatrix}}_{\rho_{2\,\text{level system}}} \Bigg] + \Gamma \cdot \begin{pmatrix} \rho_{11} & -\frac{1}{2}\rho_{21} \\ -\frac{1}{2}\rho_{12} & -\rho_{22} \end{pmatrix}$$

with $H_{2\,\text{level system}}$ being the Hamiltonian of the 2 level system in the rotating frame approximation with Ω_P being the Rabi frequency of the probe light and δ the detuning of the probe light. Also, the density matrix for the 2 level system $\rho_{2\,\text{level system}}$ and the term describing the decay containing Γ (decay rate from the excited state to the ground state), which is the only decay we take into account here, can be seen [80, 81]. From this, one can now determine the optical Bloch equations. Solving this system in

the steady state ($\dot{\rho} = 0$), one can determine ρ_{22} and with this the photon scattering rate to be

$$\Gamma\rho_{22} = \frac{\Gamma}{2} \cdot \frac{s_0}{1 + s_0 + \frac{4\delta^2}{\Gamma^2}}, \tag{4.2}$$

with $s_0 = \frac{2\Omega^2}{\Gamma^2} = \frac{I}{I_{\text{sat}}}$ being the saturation parameter, I being the intensity and I_{sat} being the saturation intensity [79]. One can use Eq. (4.2) together with $s_0 \ll 1$ (since we are in the single photon regime) to describe the probe attenuation in the atom cloud as

$$\begin{aligned} \frac{\mathrm{d}I}{\mathrm{d}z} &= -\hbar\omega \cdot \Gamma\rho_{22} \cdot n \\ &= -\underbrace{\frac{\sigma_0}{1 + \left(2\frac{\delta}{\Gamma}\right)^2}}_{=:\sigma} \cdot n \cdot I, \end{aligned} \tag{4.3}$$

with $\sigma_0 = \frac{\hbar\omega\Gamma}{2I_{\text{sat}}} = \frac{3\lambda^2}{2\pi}$ being the resonant cross section [79] and n being the atom density. With this one can then determine the transmission as

$$T = e^{-\sigma \int n dx},$$

with σ from Eq. (4.3). When now defining the optical density to be $\text{OD} = \sigma_0 \int n dx$, one can re-write the transmission to be

$$\mathrm{T} = a \cdot \exp\left(\frac{-\text{OD}}{1 + 4\frac{\delta^2}{\Gamma^2}}\right), \tag{4.4}$$

where a is the number of photons.

The transmission signal calculated from Eq. (4.4) for different values of the probe detuning δ is shown in Fig. 4.12(b) together with the respective level scheme in Fig. 4.12(a). The only parameter varied for the different plots is the optical density. It can be seen that the higher the optical density, the broader the absorption spectrum.

The Rubidium atoms are magnetically trapped and the spacially varying field alters the probe transmission signal. This was investigated in more detail by Cedric Wind and I want to stress the idea here. Depending on where the atoms are sitting relative to the zero field, they either see the incoming probe light with σ^+ or σ^- polarization because of the orientation of the magnetic field. Because of the optical pumping, all atoms start of in the $|F = 2, m_{\text{F}} = 2\rangle$ state. Therefore the probe laser drives either $|F = 2, m_{\text{F}} = 2\rangle \rightarrow |F' = 3, m_{\text{F}'} = 1\rangle$ or $|F = 2, m_{\text{F}} = 2\rangle \rightarrow |F' = 3, m_{\text{F}'} = 3\rangle$. Here, one has to note that since we work in the single photon regime, the two possible transitions are treated as a two-level system each and combined by taking their Clebsch Gordon coefficients CG (1 for $|F = 2, m_{\text{F}} = 2\rangle \rightarrow |F' = 3, m_{\text{F}'} = 3\rangle$ and $\frac{1}{15}$ for $|F = 2, m_{\text{F}} = 2\rangle \rightarrow |F' = 3, m_{\text{F}'} = 1\rangle$ [57]) into account. This is why one can take the cross section from Eq. (4.3) as a starting point. Depending on where the atoms sit with respect to the magnetic field, this results in a different level shift because of the Zeeman effect which is given by

$$\Delta_{\text{Zeemann}} = \begin{cases} 0.93\,\text{MHz/G} \cdot 1 - 0.70\,\text{MHz/G} \cdot 2, & |m_{\text{F}} = 2\rangle \rightarrow |m_{\text{F}'} = 1\rangle \\ 0.93\,\text{MHz/G} \cdot 3 - 0.70\,\text{MHz/G} \cdot 2, & |m_{\text{F}} = 2\rangle \rightarrow |m_{\text{F}'} = 3\rangle \end{cases}, \tag{4.5}$$

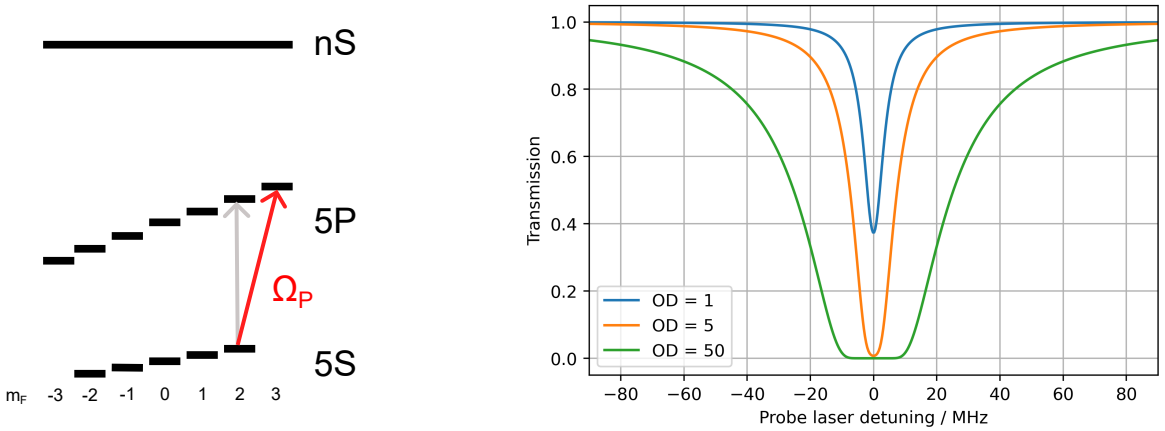

(a) (b)

Figure 4.12: Optical probe transition level scheme where the probe light drives the $|5S,\ F = 2,\ m_F = 2\rangle \rightarrow |5P,\ F' = 3,\ m_{F'} = 3\rangle$ transition and the control light is turned off **(a)**. The splitting caused by the magnetic trap in which the atoms are sitting in is illustrated. For this case, however, we are only interested in a simple two level system (red arrow) and the consideration of other transitions contributing (grey) will only be included later. This then corresponds to the theoretical probe transmission signal through the atom cloud in **(b)**. The transmission spectrum is plotted for a linewidth of 6 MHz and for different values of the optical density using Eq. (4.4) with QuTiP [82, 83]. The larger the optical density, the stronger the absorption dip.

with values taken from [42]. Here, μ_B is the Bohr magneton and g_F being the g-factor for an atom with total atomic angular momentum F. By inserting Eq. (4.5) into the given formula for the cross section from Eq. (4.3), one can find a new cross section depending on which of the two transitions mentioned is driven

$$\sigma_B = \frac{\sigma_0}{1 + \left(2(\delta - \Delta_{\text{Zeemann}}) \cdot B\right)^2} \cdot \begin{cases} 1, & |m_F = 2\rangle \rightarrow |m_{F'} = 3\rangle \\ \frac{1}{15}, & |m_F = 2\rangle \rightarrow |m_{F'} = 1\rangle \end{cases} . \tag{4.6}$$

One other parameter that has to be considered is the expected probability density in a linear magnetic quadrupole trap for a given temperature and field which can be written as

$$D(x, y, z) = \exp\left(-\frac{g_F \mu_B m_F}{k_B} \cdot \text{grad}(B) \frac{\sqrt{x^2 + y^2 + 4z^2}}{10^4 \cdot T}\right), \tag{4.7}$$

assuming the atoms to be Boltzmann distributed and 10^4 being the factor between Gauss and Tesla [50, 84]. When applying Beer's law it is possible to write down the transmission of the photon through the atom cloud which can be written as

$$T = \exp\left(-\int dx \sigma_B D(x, 0, 0) \cdot \frac{N}{\iiint D(x, y, z)\, dxdydz}\right), \tag{4.8}$$

with N being the number of atoms, D is from Eq. (4.7) and σ_B from Eq. (4.6).

With this it is possible to have a look at the theoretical signal of the transmission depending on

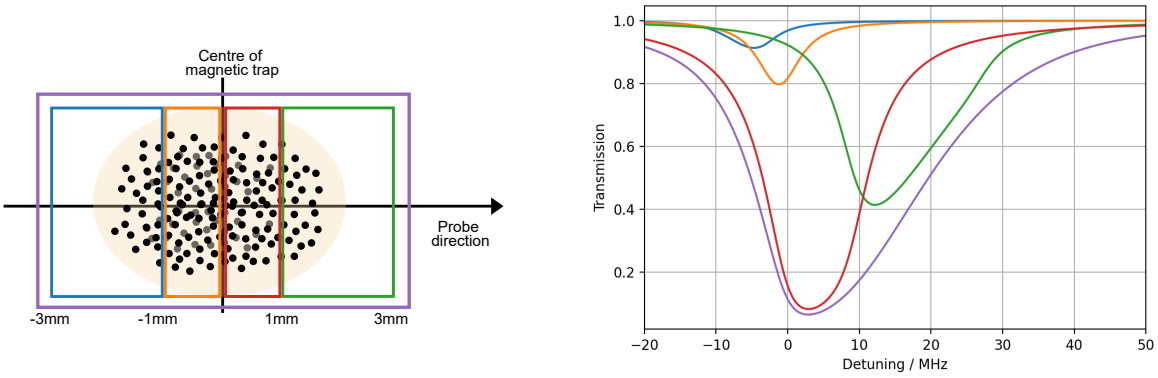

(a) (b)

Figure 4.13: Drawing of the atom cloud sitting in the center of the magnetic quadrupole trap **(a)**. Depending on where the atoms are sitting in the cloud (different slices for different distances from the magnetic field center along the probe axis are illustrated) corresponds to a different OD contributions in **(b)**. For the OD plot, Eq. (4.8) is plotted for a magnetic field gradient of 65 G/cm, an atom number of $N = 2 \cdot 10^8$ and a temperature of $T = 400\,\mu\text{K}$ for different atom cloud slices (blue: -3 mm to -1 mm, orange: -1 mm to 0 mm, red: 0 mm to 1 mm and green: 1 mm to 3 mm from the center) and the sum over all slices (-2 cm to 2 mm) which is illustrated in purple.

the position of the atoms with respect to the magnetic field center along the probe axis which is visualized in Fig. 4.13(b). The respective slices of the atom cloud are illustrated in Fig. 4.13(a). The temperature, atom number and magnetic field gradient for the plot are set to values we would expect in our experimental setup. From this, one can see that different positions of the atoms in the cloud along the probe axis lead to different contributions to the transmission spectrum. In purple, the sum over all contributions (four of which are illustrated in blue, orange, red and green) are plotted.

With this it is possible to determine the atom number and the temperature of the atoms by fitting Eq. (4.8) to the data in the following.

4.2.3 Transmission spectroscopy of probe light without control

With the SPCM being implemented, it is now possible to perform a first transmission spectroscopy measurement. For this, the transmission spectrum of the probe light as a function of the probe detuning through the atom cloud can be measured while the control light is blocked. This measurement depends on the number of atoms as well as the overlap of the atoms with the probe beam. The measurement is displayed in Fig. 4.14(a). The solid line corresponds to the data taken with atom cloud and the dashed line to the background measurement. Here, one can see the transmission spectrum and an absorption dip corresponding to the probe light being resonant with the atom transition. By dividing the two traces, signal and background measurement, and taking detection efficiencies into account, it is possible to plot the transmission as a function of the probe detuning as it is illustrated in Fig. 4.14(b). By taking the laser power, attenuation, fiber couplings and detection efficiency into account, it is possible to determine the number of photons per pulse from the detected signal. Here, one can see that the minimal transmission is not at zero detuning but shifted. The shift towards blue-detuning results from the atoms sitting in the magnetic trap. This also becomes apparent in the theoretical

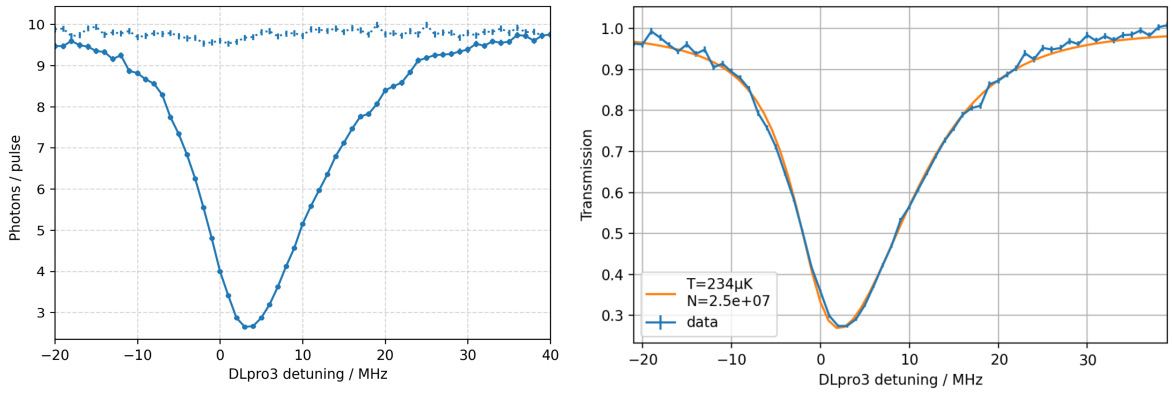

(a) (b)

Figure 4.14: Photon signal per pulse detected with the single photon counter with one data point being the average of 1000 pulses for signal (solid line) and background (dashed line) for seven measurement cycles **(a)**. In **(b)** one can see the resulting signal when subtracting the background counts from the signal to determine the transmission normalized to 1, with one being complete transmission and 0 being complete absorption. This is fitted with the function in Eq. (4.8) from which the atom number and temperature can be determined.

model (see Eq. (4.8)) which is fitted to the data. From this fit it is possible to determine the atom number to be $N = (2.5 \pm 0.1) \cdot 10^7$ and the temperature to be $T = (234 \pm 5)$ µK. The temperature is similar to what was found after the magnetic transport assuming re-thermaization of the atom cloud ($T = (186.2 \pm 3.0)$ µK and $T = (267.4 \pm 11.3)$ µK for two different axes in Section 3.8).

With this, it was possible to show that the probe beam is overlapped with the atom cloud because this results in an absorption dip in the transmission spectroscopy. However, for this first measurement, not much attention was paid to the exact overlap of atom cloud and probe light other than choosing a position where the overlap was apparent. To improve this (i.e. increase the absorption further), it helps to improve the overlap.

This means that the cloud position is moved in the area perpendicular to the probe beam (similar to how it was done previously using the imaging system in Section 4.1.3) and the probe signal passing through is detected with the SPCM. The control light is blocked for this measurement. The transmission of the probe light as a function of the cloud position (i.e. the settings for the bias fields) is displayed in Fig. 4.15. For this, the probe light detuning was chosen such that it is resonant with the atoms.

The result can be interpreted in such a way that when the probe overlaps with the atoms, the light is absorbed and therefore the transmission reduced.

To cover the whole area possible, the orientation of the bias fields had to be switched, i.e. the sign of the current was changed, such that the largest possible area could be mapped out. With this done, it is now possible to choose the bias field setting such that the overlap of the probe light and the atom cloud is best. Here, the bias field configuration corresponding to the lower right plot in Fig. 4.15 was chosen with the bias field settings of $B_y = 0\,\mathrm{G}$ and $B_z = 2\,\mathrm{G}$.

With the overlap of the atom cloud and the probe beam being optimized further, it is possible to re-do the transmission spectroscopy measurement from Fig. 4.14(b). This then results in the measurement visualized in Fig. 4.16(a). Here, one can see a higher atom number seen by the probe light of $N = (4.3 \pm 0.4) \cdot 10^7$ and roughly the same temperature as before $T = (239 \pm 12)$ µK (the

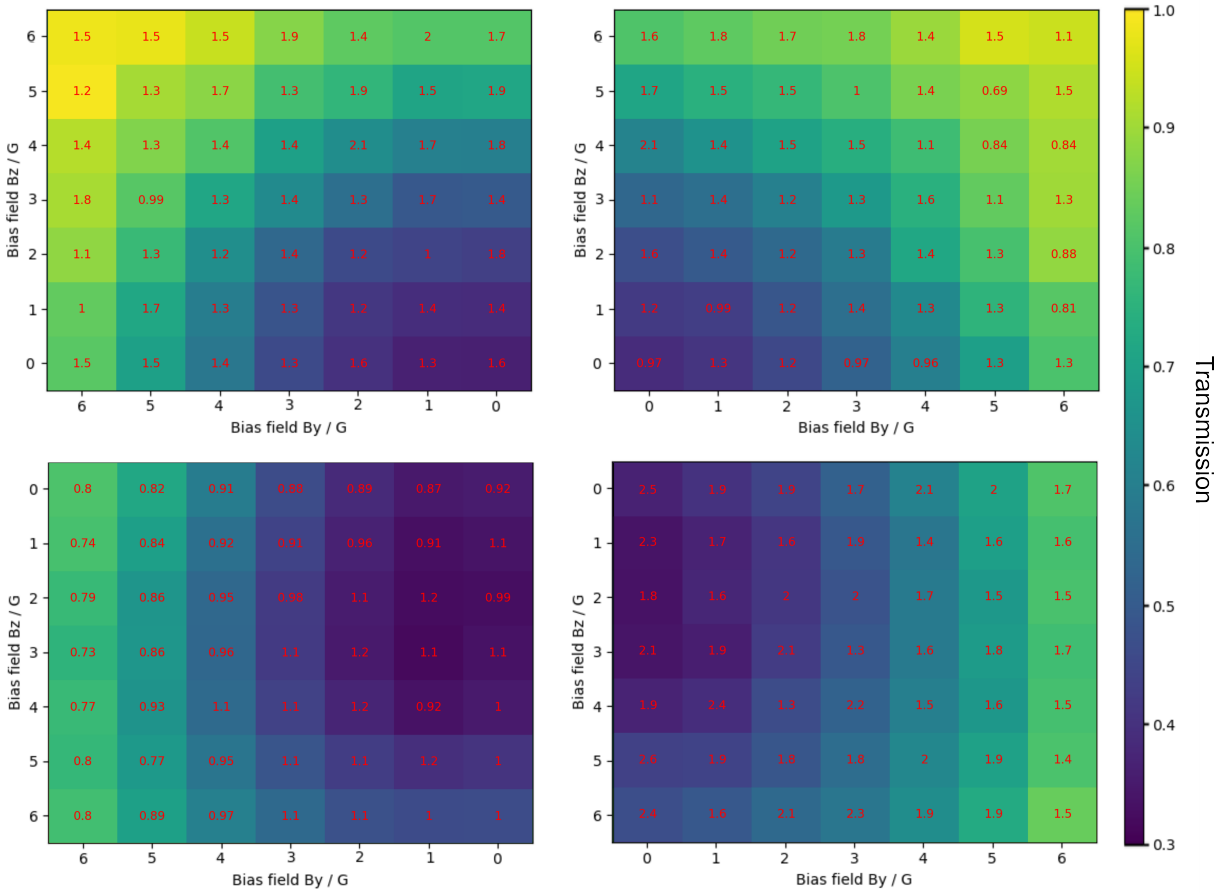

Figure 4.15: Transmission of the probe light through the atom cloud as a function of different bias field settings measured with the SPCM. The red numbers correspond to the relative error in percentage. A decrease in transmission indicates the presence of atoms as then probe light is absorbed. The bias fields are scanned in both directions meaning that all four plots map the cloud position.

previously found values were: $N = (2.5 \pm 0.1) \cdot 10^7$ and $T = (234 \pm 5)$ µK). With this it was possible to show that the overlap of the atom cloud and the probe beam could be further improved resulting in a higher atom number contributing to the absorption spectrum.

To increase the transmission dip even further, it was chosen to not ramp down the magnetic field gradient any more but to keep it at 130 G/cm in axial direction as this results in a cloud which is more optically dense as it is shown in Fig. 4.16(b). Here, the atom number contribution to the absorption is almost one order of magnitude larger ($N = (2.8 \pm 0.2) \cdot 10^8$) compared to the smaller magnetic field gradient. However, this also leads to a higher temperature of $T = (421 \pm 21)$ µK which is almost twice as hot as for the smaller gradient. For now, we are more interested in a larger optical density and stronger absorption which is why we chose the larger magnetic field gradient for now. For this, also the bias fields had to be scanned again to look for the optimal overlap similar to how it was done in Fig. 4.15 with the decreased magnetic field gradient.

With this being found, it is now possible to go one step further and include the control laser for coupling the intermediate state to the Rydberg state in the following.

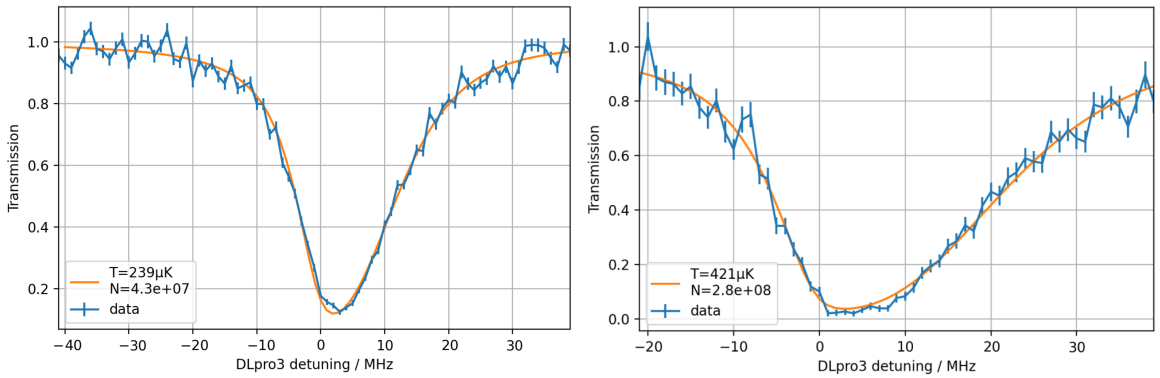

(a) (b)

Figure 4.16: Photon signal per pulse detected with the single photon counter after optimizing the overlap of atom cloud and probe beam in **(a)** (averaged over six measurement cycles) with the same configurations as in Fig. 4.14(b) and with an increased magnetic field gradient for the final trap in **(b)** (averaged over three measurement cycles). It was possible to decrease the transmission from 0.2 to 0.1 with the better beam overlap and it was possible to increase the number of atoms contributing to the absorption by increasing the magnetic field gradient. Also, the theoretical model from Eq. (4.8) could be fitted to the data from which the temperature T and atom number N could be extracted.

4.2.4 Detection of Rydberg excitation

With everything set up and tested, it is now possible to perform transmission spectroscopy of the probe beam when the intermediate transition is coupled to a Rydberg state.

In this part I will briefly introduce the concept of EIT as it is implemented in the experiment. EIT can be described using the dressed state picture or the dark state polariton picture [33].

In the dressed state picture the phenomenon can be explained as follows: the strong control beam couples the states $|2\rangle$ and $|3\rangle$, which leads to a splitting of the state $|2\rangle$ into so-called dressed states $|+\rangle$ and $|-\rangle$. This splitting can also be seen for the state $|3\rangle$, but is not relevant for the explanation of EIT. This is illustrated in more detail in Fig. 4.17(a). This coupling and splitting of states of a two level system can be described by the Jaynes-Cummings Hamiltonian given by

$$H_{\mathrm{JC}} = \underbrace{\hbar\omega_a \sigma^+\sigma^-}_{\text{atom}} + \underbrace{\hbar\omega_c a^\dagger a}_{\text{light}} + \underbrace{\hbar g(a^\dagger\sigma^- + \sigma^+ a)}_{\text{atom-light}},$$

where $\hbar\omega_a$ is the energy of the atom in the excited state, $\sigma^+ = |e\rangle\langle g|$ and $\sigma^- = |g\rangle\langle e|$ are the creation and annihilation operators of the atom, $\hbar\omega_c a^\dagger a$ are the energy eigenvalues depending on the number of photons and $a^\dagger$, a are the ladder operators [85]. When the absorption or transmission of the probe light is measured as a function of the probe laser detuning, destructive interference of the excitation paths $|1\rangle \rightarrow |+\rangle$ and $|1\rangle \rightarrow |-\rangle$ occurs. This results in a transmission window characteristic for EIT.

The susceptibility in the EIT limit (derived by Fleischhauer et al. in [33]) is given by

$$\chi_{\mathrm{EIT}} = \frac{\mu_{\mathrm{eg}}^2 n}{\epsilon_0 \hbar V}\left(\frac{4\delta(|\Omega_c|^2 - 4\delta\Delta) - 4\Delta\gamma_{21}^2}{||\Omega_c|^2 + (\gamma_{31} + 2i\Delta)(\gamma_2 1 + 2i\delta)|^2} + i\frac{8\delta^2\gamma_{31} + 2\gamma_{21}(|\Omega_c|^2 + \gamma_{21}\gamma_{31})}{||\Omega_c|^2 + (\gamma_{31} + 2i\Delta)(\gamma_{21} + 2i\delta)|^2}\right), \tag{4.9}$$

where Ω_c is the Rabi frequency of the control laser, $\Delta = \Delta_1$ is the single-photon detuning, $\delta = \Delta_1 - \Delta_2$ is the two-photon detuning, and γ_{31}, γ_{21} are the coherence decay rates. The decay rate from the intermediate state to the ground state γ_{21} can be approximated by the natural linewidth of Γ as done in [86]. From the imaginary part of Eq. (4.9) the transmission can be extracted, similar to the optical density.

There are two cases one has to take a closer look at. First, there is the resonant Rydberg excitation which is illustrated in Fig. 4.17(b). Here, the probe laser is resonant with the $|5\mathrm{S}\rangle \rightarrow |5\mathrm{P}\rangle$ transition and the control laser is resonant with the $|5\mathrm{P}\rangle \rightarrow |n\mathrm{S}\rangle$ transition. Also, possible decays from the intermediate state to the ground state γ_{21} and from the Rydberg state to the ground state γ_{31} are illustrated. The decay from the Rydberg state to the intermediate state γ_{32} is suppressed and therefore not illustrated here [23]. For this case, one would expect to see the characteristic EIT peak on resonance. The second case is the off-resonant two-photon transition (illustrated in Fig. 4.17(c)). In this case, both, the control and the probe laser, are detuned from resonance such that Rydberg excitation takes place when the probe laser compensates for the detuning of the control laser. In this case, one would expect a decrease of probe transmission for the two photon detuning corresponding to zero.

In the following, the expected theoretical signal for the resonant and off-resonant case are plotted with QuTiP in Figs. 4.18(a) and 4.19(a) to be able to compare them to the experimental data. For the following plots, the optical density was set to 3 as this is roughly what we would expect. The coupling strength of the probe beam is set to $\Omega_P/(2\pi) = 0.5\,\mathrm{MHz}$ which is smaller than the values chosen for the control coupling strength which is mentioned in the plots explicitly. Also, the linewidth (i.e. the decay from the intermediate state back to the ground state) was set to $\Gamma/(2\pi) = 6\,\mathrm{MHz}$ (value taken from [42]). Other decays (from the Rydberg state to the intermediate state $|n\mathrm{S}\rangle \rightarrow |5\mathrm{P}\rangle$ and from the Rydberg state back to the ground state $|n\mathrm{S}\rangle \rightarrow |5\mathrm{S}\rangle$) are set to zero as they are not known. These assumptions together with not taking the influence of the magnetic field into account will lead to a deviation from the measurements but it will still be possible to identify the characteristic features for the respective signals.

The theoretical signal for the resonant case in EIT conditions is plotted in Fig. 4.18(a), where one can see the characteristic transmission window. The signal is plotted for two different Rabi frequencies of the control beam to illustrate its behaviour with respect to the transmission signal. For higher control power ($\Omega_c \propto \sqrt{I_c}$) the linewidth becomes wider. This must be taken into account depending on what is required.

Fig. 4.18(b) shows the signal measured in the experiment. In the measured signal one can again see the characteristic features caused by the magnetic trapping of the atoms which is a slightly asymmetric transmission spectrum shifted towards blue detuning. The figure shows that by coupling the intermediate state with the control laser to the Rydberg state, it is possible to see the characteristic EIT features one would expect theoretically. The measured transmission in the EIT window is smaller

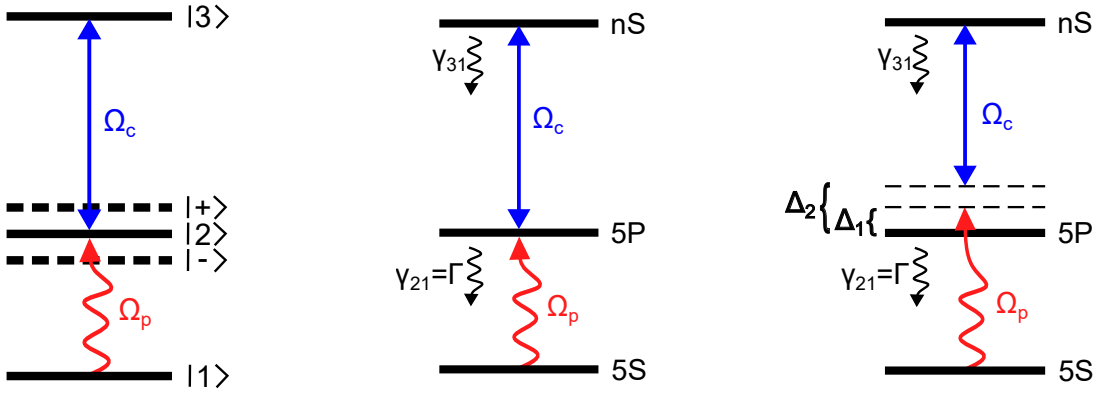

(a) (b) (c)

Figure 4.17: General three level scheme with ground state $|1\rangle$, intermediate state $|2\rangle$ and Rydberg state $|3\rangle$ **(a)**. The states $|2\rangle$ and $|3\rangle$ are coupled with a strong control field Ω_c which leads to a splitting of the states in dressed states $|+\rangle$ and $|-\rangle$. In principle this would also apply to $|3\rangle$ but since we perform transmission spectroscopy on the probe transition $|1\rangle \rightarrow |2\rangle$, it is not relevant here. The used Rubidium Rydberg excitation level scheme for on resonant excitation in **(b)** and off-resonant excitation in **(c)** are illustrated. Also, the decay from the intermediate state to the ground state is illustrated as $\gamma_{21} = \Gamma$ as well as the decay from the Rydberg state back to the ground state γ_{31}. The detuning for the probe beam with respect to the intermediate state is Δ_1 and for the control laser Δ_2. The resonant transition scheme would result in the expected EIT peak on resonance while the off-resonant transition would result in a two photon Rydberg excitation dip detuned from resonance.

than in Fig. 4.18(a) because for the theoretical plot all decoherences and decays other than the linewidth were neglected. With this measurement it was possible to show that the intermediate state was in fact coupled to the Rydberg state.

Additionally, one can also look at off-resonant two-photon excitation. The theoretical signal is plotted in Fig. 4.19(a). Here, one can see the OD-valley which corresponds to the absorption of the probe laser by the atom cloud. Additionally, one can see another dip corresponding to the detuning for which Rydberg excitation can be performed. Since the control laser is detuned from resonance, Rydberg excitation takes place when the detuning of the probe laser compensates for the detuning offset of the control laser. This is illustrated for two different detuning offset of the control laser.

This was implemented experimentally by changing the locking point of the control laser such that its frequency is slightly detuned from the transition of the intermediate state to the Rydberg state. Then, transmission spectroscopy of the probe light through the atom cloud is again performed by changing the detuning of the probe light which is illustrated in Fig. 4.19(b). One can see the two-photon excitation dip at a probe detuning of $-10\,\mathrm{MHz}$ which indicates Rydberg excitation. Again, the transmission dip is smaller than plotted for the theoretical signal because for the theoretical signal no decoherences and decays were taken into account.

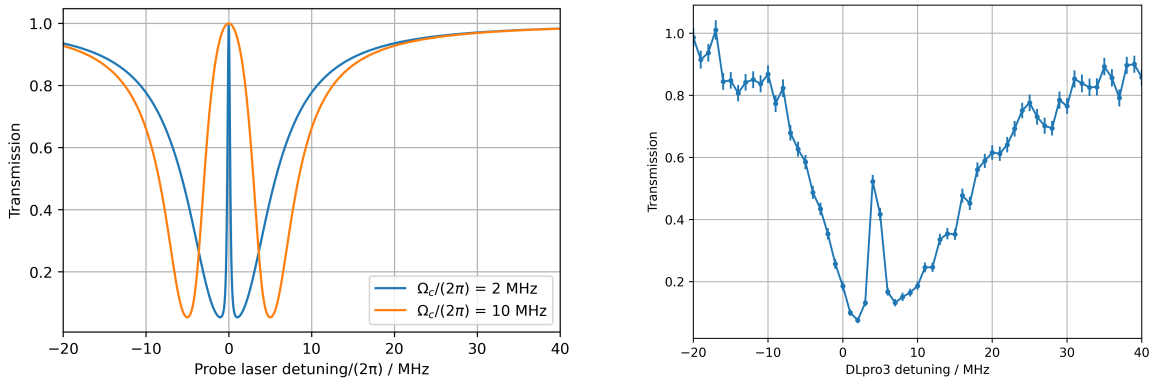

(a) (b)

Figure 4.18: Theoretical transmission spectrum of the probe light through an atom cloud in EIT conditions for different Rabi frequencies of the control light Ω_c is plotted as a function of the probe detuning **(a)** with QuTiP. The linewidth (i.e. decay rate on probe transition) was set to $\Gamma/(2\pi) = 6\,\text{MHz}$, the coupling strength of the probe laser was set to $\Gamma/(2\pi) = 0.5\,\text{MHz}$, the OD was set to 3 and other decays (decay on coupling transition and decay from upper state to the ground state) were set to zero. The transmission spectroscopy signal in EIT condition measured in the experiment shows the characteristic EIT peak **(b)**. Each data point is the average over 3000 measurement pulses.

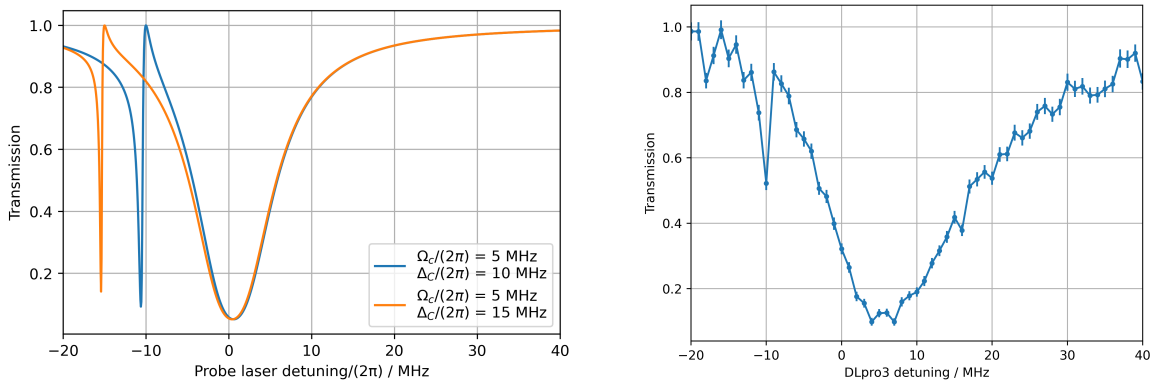

(a) (b)

Figure 4.19: Theoretical transmission spectrum of the probe light through an atom cloud in the case of off-resonant two-photon excitation for different detuning offsets from resonance is plotted as a function of the probe detuning **(a)** with QuTiP. The linewidth was set to $\Gamma/(2\pi) = 6\,\text{MHz}$, the coupling strength of the probe laser was set to $\Gamma/(2\pi) = 0.5\,\text{MHz}$, the OD was set to 3 and other decays were set to zero. The transmission spectroscopy signal for a two photon resonance measured in the experiment is plotted in **(b)**. Each data point is the average over 3000 measurement pulses.

4.3 Ionization detection of Rydberg atoms

In addition to the single photon counters, the use of ionization in this experiment provides another way of detecting Rydberg atoms. To use ionization, one exploits the fact that Rydberg atoms can be ionised with electric field strengths that are easily achievable [23].

Ionization detection of Rydberg atoms after performing an experiment allows to determine how many Rydberg atoms remain after the experiment. Another benefit of ionization detection is the possibility to ionize state-selective as different states need different ionization voltages to be ionized.

First, the Rydberg ionization setup implemented in the experiment will be introduced in Section 4.3.1. This is followed by the detection of Rydberg atoms in Section 4.3.2.

4.3.1 Implementation of the Rydberg ionization setup

In this section, the current room-temperature setup used to perform ionization detection of Rydberg atoms is discussed in more detail. The current room temperature setup used during this thesis is shown in Fig. 4.20. It was designed by Hannes Busche and assembled by Johanna Popp [35]. After Rydberg excitation, the atoms are ionized with the ionization electrodes. One electrode is grounded while the other is positively charged. This causes ionization and the positively charged ion is accelerated away from the positively charged "push"-electrode towards the deflection electrode. The deflection electrode then guides the ions to the Micro Channel Plate (MCP) (F4655-11 MCP from Hamamatsu), which detects the ions. The MCP has many separate channels, making specially resolved detection possible. The incoming ion results in a signal on the detector, which can be counted by the Time Tagger.

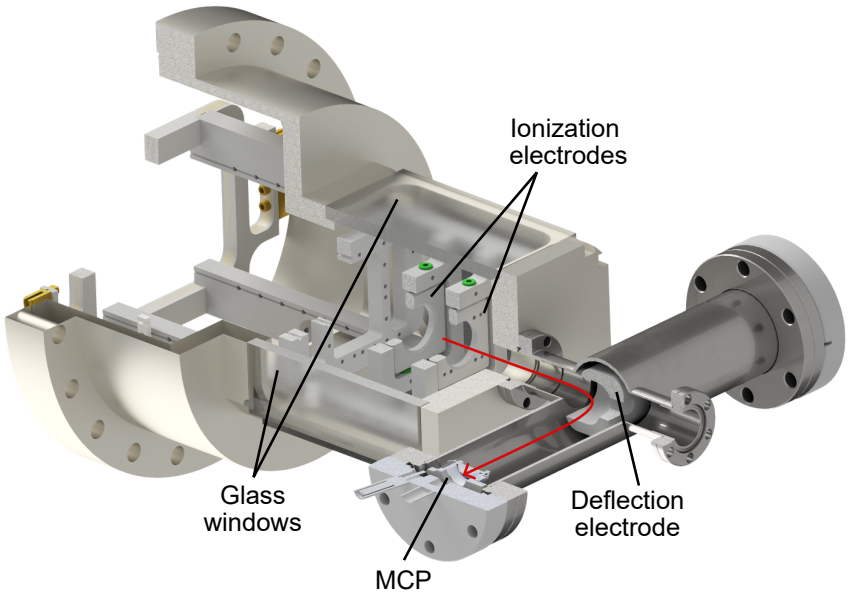

Figure 4.20: Inner assembly used for detecting ionized Rydberg atoms. The Rydberg atoms (sitting in the middle of the two ionization electrodes) are ionized using two electrodes and are accelerated towards the deflection electrode which guides the ions to the MCP where it corresponds to a click. The red arrow visualizes the trajectory of the ion towards the MCP.

As the ionization voltage available in the experiment is finite, one can find a lower bound of what Rydberg states can be ionized. The electric field needed to perform ionization for a Rydberg s-state ($l = 0$) can be approximated as follows, as mentioned in [87]: In the case of large electric fields, the potential between the Rydberg atom and its valence electron can be classically described as a superposition of the Coulomb potential $V_C(r) \approx -\frac{1}{r}$ and the electric potential $V_E = -eEz$. This can then be estimated as

$$E = 3.2 \cdot 10^8 \frac{\mathrm{V}}{\mathrm{cm}} \cdot \frac{1}{(n - \delta_{nlj})^4}\,, \tag{4.10}$$

in the case of a Rydberg s-state ($l = 0$), where n is the principal quantum number, δ_{nlj} is the quantum defect [22, 88]. In this way, it is possible to determine the minimum principal quantum number that can still be ionized. A voltage of 500 V, which is achievable in the current setup, corresponds to a field of 192 V/cm for the current geometry. With a quantum defect of $\delta_{nlj} \approx 3.13$, [89], and Eq. (4.10), the minimum quantum number is found to be

$$n = \left(\frac{3.21 \cdot 10^8}{192}\right)^{1/4} \approx 40\,. \tag{4.11}$$

As the future experiments are planned to be performed with a principal quantum number of $n = 68$, as determined by Leon Sadowski [31], this detection setup is suitable to detect Rydberg atoms of this state. This means that even though this is not the setup that will be used in the cryogenic setup later, it is suitable for testing the Rydberg excitation.

As the cryostat is not available for the duration of this thesis, a partially alternative setup, was used. The setup discussed in this section will ultimately be exchanged by the future setup designed by Leon Sadowski [31]. The main difference between the two setups are the ionization electrodes. In the future setup the ionisation electrodes will be much smaller and implemented together with the atom chip. The deflection used to guide the ions to the MCP and the MCP itself will remain the same in the future setup. The goal of the current setup was to make the implementation of Rydberg excitation and detection possible such that it can be used in a modified fashion later in the future setup.

Before performing measurements with the ionization setup, it is necessary to ensure that the pulses generated by the MCP are within an amplitude range that does not damage the counting device, i.e. the Time Tagger. This is ensured by a protection circuit designed by Cedric Wind. The signal is attenuated by 12 dB, passes through a set of four protection diodes (1SS315(TPH3,F) from Toshiba) in an anti-parallel circuit, is inverted by an amplifier (ZX60-6013E-S+ from Mini-Circuits) and passes again through a set of 6 protection diodes before being detected. This is necessary to avoid damaging the Time Tagger, as the signals from the MCP can produce large positive and negative signals that could destroy the Time Tagger. Fig. 4.21 shows the analogue pulse that results from an ion detection signal passing through the protection circuit. The shown resulting signal amplitude lies in the required range.

This made it possible to integrate the ionization of Rydberg atoms into the experimental setup and implement the sequence described below.

The implementation of the ionization into the computer control is mentioned in Fig. 4.8. After performing Rydberg excitation, single photon spectroscopy is done. After that, the ionization and deflection electrodes are triggered by the Pulse Generator and a control voltage is applied such that the ionization and deflection takes place.

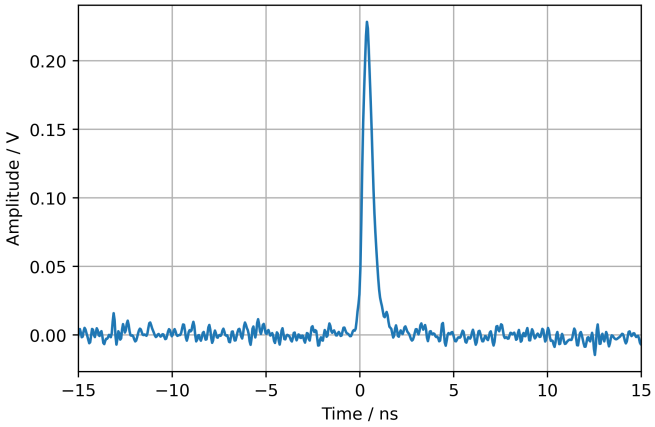

Figure 4.21: Example for an analogue MCP signal measured after attenuation, being inverted and going through protection diodes resulting in a sufficiently small signal amplitude. This is the signal that will be connected to the Time Tagger which counts the number of signals in a given time range.

This makes it possible to perform an experiment where transmission spectroscopy is performed, followed by ionizing the remaining Rydberg atoms and detecting them via ionization detection.

4.3.2 Detection of Rydberg atoms

With the ionization sequence being implemented, it is possible to detect Rydberg atoms by ionization in this experimental setup. This has been done and the measurement is shown in Fig. 4.22(a). The solid line corresponds to the data taken with atoms and the dashed line corresponds to the data taken without atoms, after turning off the trap. For the measurement the probe detuning was scanned and for each detuning 4000 measurements were taken (i.e. the atoms were loaded for 4 times each time performing a 1000 measurements). In each measurement, one can see the sum of all detection events inside a detection window of 17 µs. It is possible to first measure transmission spectroscopy of the probe light with the SPCM and then perform ionization detection. The photon signal is obtained from the same measurement and is shown in Fig. 4.22(b). One can see that the two-photon transition takes place for a probe detuning of roughly 45 MHz and roughly one photon is absorbed during that process. This is known by determining the detection efficiencies by checking the power in front of and after the chamber and also taking coupling efficiencies into the optical fibers into account. It is then possible to extract the photons per pulse which can then be compared to the measured ion signal. One photon being absorbed corresponds to roughly 0.14 ion counts. From this we can see that the efficiency of the ionization is about 14%.

It is important to note that the aim of this measurement was to prove that it is possible to excite Rydberg atoms and then detect them. No further optimization of improving the detection efficiency was carried out during this work. However, as the deflection electrode and the MCP will also be present in the future setup, it is useful to further improve the detection of ions.

This has shown that the Rydberg excitation works and we are able to detect both, the photon signal and the ion signal, to prove the existence of the Rydberg atoms.

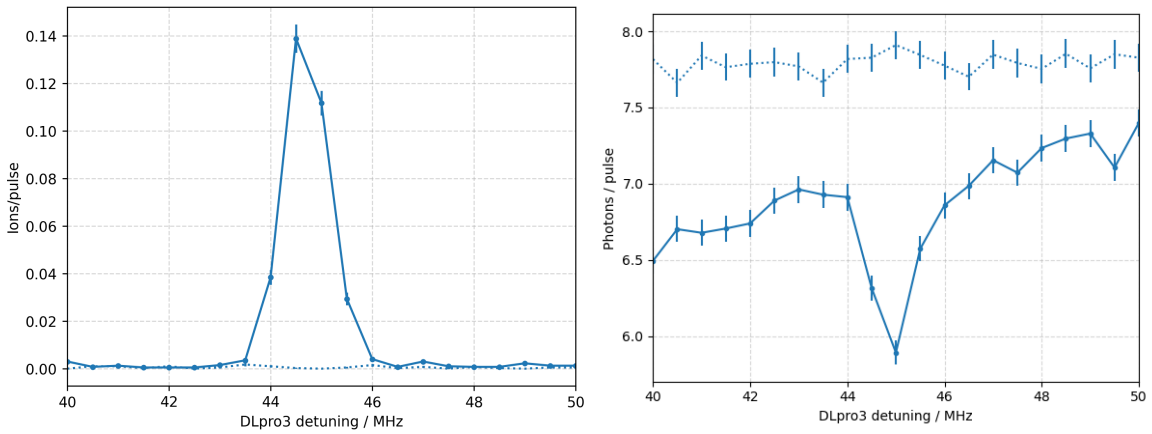

(a) (b)

Figure 4.22: Measured ions per pulse as a function of the probe detuning **(a)**. One can see counts corresponding to the ion signal. For the same measurement, also the photon signal was detected **(b)**. In both cases the solid line corresponds to the measurement and the dashed line to the background measurement. One can see that one lost photon corresponds to 0.14 ion counts which leads to a detection efficiency of 14%.

CHAPTER 5

Conclusion

The goal of this thesis was to implement a Rubidium Rydberg excitation scheme in the Hybrid Quantum Optics (HQO) experiment, taking one step towards the ultimate aim of interfacing Rydberg atoms with electromechanical oscillators on a chip.

Due to the two chamber design of the HQO experimental setup, which is needed to fulfil certain requirements (differential pressures and temperatures for atom loading and conducting the experiment) multiple steps of atom preparation have to be performed. The steps were characterized and optimized as part of this thesis. This includes trapping the atoms, preparing them for magnetic trapping and transporting them to the Science chamber, where the Rydberg excitation can be performed.

The first step of the atom preparation of Rubidium atoms is trapping of ^{87}Rb in a MOT from background gas for a set duration of 1 s and optimizing for the highest achievable atom number. Using multiple parameter scans for optimization, it was possible to find parameter sets that allow trapping of up to 10^9 atoms. Next, the temperature of the atom cloud had to be reduced to provide a better hand-over between MOT and magnetic trap. For this, an optical molasses was used and the respective parameters for this preparation step were optimized such that the temperature of the atom cloud could be reduced from ~374 µK in the MOT to ~26 µK after optical molasses, which is well below the Doppler limit of Rubidium [42].

For trapping the atoms magnetically, state preparation of the atoms was performed, which results in trapping of $4 \cdot 10^8$ atoms after optimization. When trapping the atoms magnetically, the finite rise (25 ms) and fall times (8 ms) of the magnetic field response of the MOT coils caused sloshing of the atoms and thus an increase of temperature. This is also the reason why MOT compression, which is used in numerous cold atom experiments to increase the phase space density of the cloud [90], could not be implemented successfully in this experiment, as magnetic trapping afterwards would lead to an increase of temperature and thus worse phase space density. By optimizing the magnetic transport, it was possible to achieve an atom number of the order of $2 \cdot 10^8$ in the Science chamber.

The optimization of the atom preparation steps, that are done in the MOT chamber, was performed with a combination of fluorescence imaging and absorption imaging. In the Science chamber, the optimization was performed with absorption imaging. Both absorption imaging setups were characterized and optimized such that the number of atoms as well as the temperature could be determined in the respective chambers.

With $2 \cdot 10^8$ Rubidium atoms being prepared at the final position, the Rydberg excitation and detection scheme was implemented. The optics were set up around the Science chamber and all

requirements such as correct wavelengths, tightly focussed probe waist, beam alignment, final atom cloud position and integration of experimental sequence, to be able to perform two photon Rydberg excitation to the desired state of $n = 68$, were met. This target state was chosen because its transition was determined by the resonance frequency of the resonator of the first generation atom chip [31]. To be able to confirm the creation of Rydberg excitation, two different detection schemes, transmission spectroscopy of the probe light and ionization detection for ionized Rydberg atoms, were implemented and characterized. Transmission spectroscopy was set up, characterized and used to map the cloud position, confirming the overlap of the cloud and the laser light for Rydberg excitation. Additionally, the theoretical transmission spectrum was fit to the probe transmission through the atom cloud in the magnetic trap. It was used to determine a temperature estimation of ($\sim 400\,\mu$K) and the number of atoms of $2 \cdot 10^8$, contributing to the transmission spectrum. It was also possible to detect a first transmission signal under EIT conditions (described in more detail in [74]), verifying a coupling from the intermediate state to the Rydberg state. To verify the presence of Rydberg excitation, ionization detection was used. The detection efficiency was estimated to be 14%.

The next steps would be to further improve the ionization detection in the current setup, without the cryostat present, followed by further characterization of the detection setup as most parts will also be used in the future cryogenic setup. Additionally, it would be beneficial to integrate an automatic optimization protocol, allowing for a more efficient atom preparation, and to achieve a large number of atoms in the Science chamber.

For now, only one single photon counter was used to perform transmission spectroscopy of the probe laser through the atomic cloud to verify the coupling to the Rydberg state. However, it is planned to use four counters simultaneously, allowing for correlation measurements. This would enable further characterization of the Rydberg excitation and transmitted photon correlation.

Finally, the cryostat will be integrated into the setup in the near future, which will make first experiments with Rydberg atoms and the first generation test chip possible.

APPENDIX A

Complete laser table

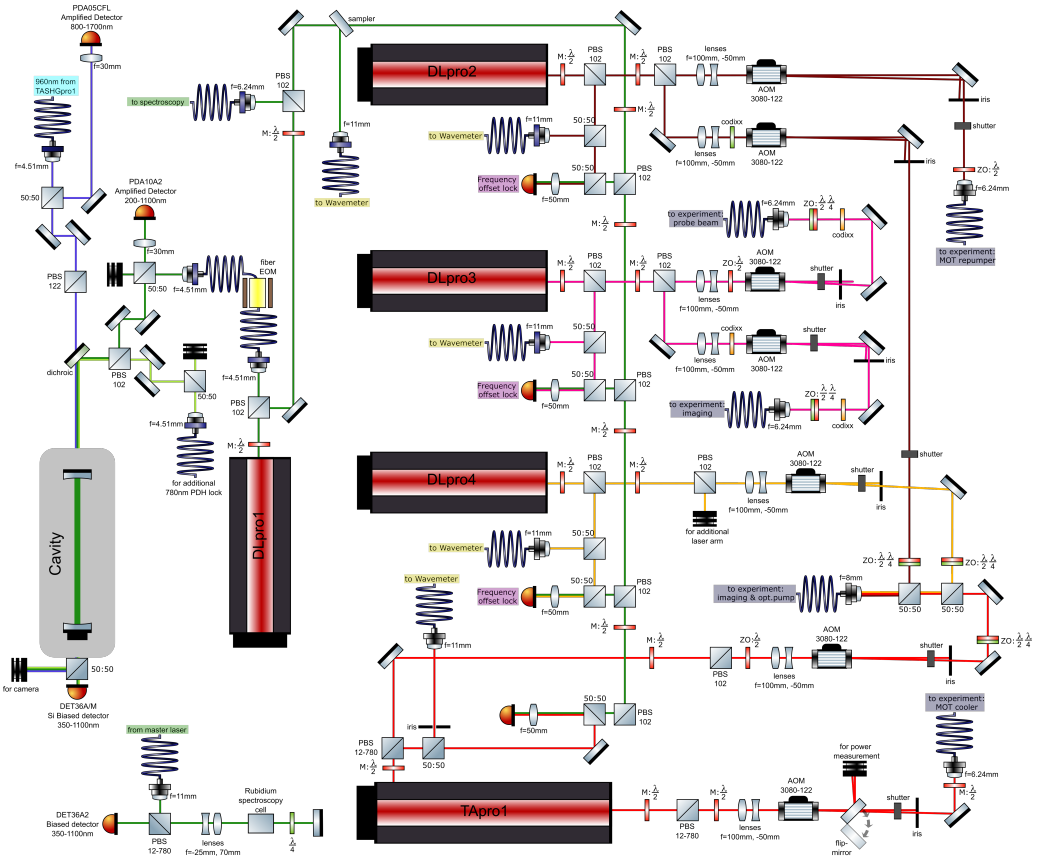

Figure A.1: Schematic of the complete laser setup for 780 nm. DLpro1 is frequency-locked to an external ultra low expansion cavity and is used as a frequency reference for the other lasers which are stabilized relative to that laser with an optical phase lock loop. DLpro2 and DLpro3 are split into two paths to be able to use them individually for different purposes. All paths are coupled through an AOM into a single mode fiber to the experimental table.

APPENDIX B

MOT compression

In most cold atom experiments it is useful to increase the phase space density to e.g. generate a Bose-Einstein condensate [91], or to better trap the atoms later on as mentioned in the methods in [90]. One benefit of MOT compression in this experiment is a better trap volume overlap with the magnetic trap which could improve the trap transfer from the MOT to the magnetic trap. This would then also result in a lower cloud temperature in the magnetic trap.

The aim of compression in this experiment is to load the atoms into the magnetic trap more efficiently later. Direct loading into the compressed MOT is not possible due to light-assisted collisions and will not lead to a sufficient number of atoms. In this experiment it is found that compression does not lead to an improvement in the atom preparation and is therefore omitted, which will now be discussed in more detail.

In the compression process, the aim is to further compress the atoms trapped in the MOT by rapidly increasing the magnetic field gradient, as shown in Fig. B.1. Besides increasing the MOT gradient, also the red detuning of the MOT lasers is increased linearly. The power of both MOT lasers stay at the highest value, as decreasing the power only led to a decrease of atom number. Compression is done over a period of 30 ms.

In this experiment, it is not possible to turn the magnetic field on and off quickly, which is described in more detail in Section 3.6. This results in not being able to turn off the magnetic field fast enough after compression to perform optical pumping or optical molasses before the atoms have fallen too far. Furthermore, it is not possible to turn on the magnetic field fast enough after optical pumping to avoid sloshing, because the atom cloud will be accelerated downward by gravity before the magnetic trap is fast enough to trap the atoms. This means that the possible advantage of compression for a better overlap with the magnetic trap is nullified. Compression therefore only leads to a loss of atoms without improving the transfer.

Attempts were made to optimize MOT compression, but due to the points mentioned, the optimization of the transfer was not possible.

One idea would be to exchange the cooling blocks made of copper but for the time being the atom number is sufficiently high. It is also planned to implement evaporative cooling in the Science chamber later which will make it possible to reduce the temperature of the atom cloud.

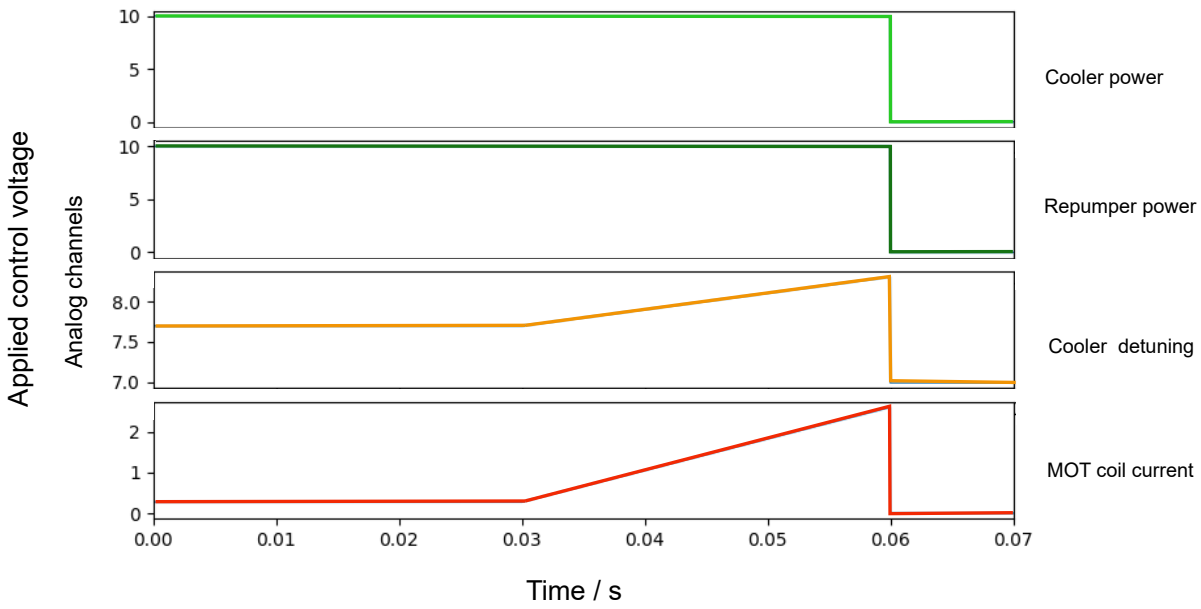

Figure B.1: Sequence used for MOT compression. The applied control voltage of the analog channel for the respective output is plotted as a function of time. First, the MOT is loaded which is illustrated as it was already introduced in Fig. 3.1 and after that, the control voltage for the MOT coils and the detuning of the Cooler laser is linearly ramped. This results in a linear increase of the magnetic field gradient and the detuning of the cooler laser which leads to a compression of the atom cloud. Then, all four signals are turned off as the next step would be the imaging as a characterization tool which is not illustrated here but done exactly as in Fig. 3.1.

APPENDIX C

Characterization measurement in the magnetic traps

The experimental setup consists of a two chamber design. Among other advantages, this allows to have different pressures in both chambers. This enables a quick loading of the MOT in the MOT chamber while conducting the experiment in better vacuum in the Science chamber. In Appendix C.1, I will first present the expected possible pressure difference in the case of our experiment with the chosen differential pumping tube. This is followed by characterization measurements in both magnetic traps (see Appendix C.2). The lifetime of the atoms in the two chambers in the magnetic traps were determined and from this it is possible to get a rough estimation for the respective background pressure.

C.1 Pressure difference because of differential pumping

As mentioned above, an advantage of the two-chamber design is the ability to ensure a better vacuum in the experimental region compared to the location where the atoms are loaded.

For that, one can make a rough estimation of the expected background pressure when outgassing of the walls is neglected. This follows the calculation in reference [92]. Taking all the approximations into account, one can define the differential pressure as follows

$$p_2 \cdot (S + C) = p_1 \cdot C\,, \tag{C.1}$$

with p_2 being the pressure in the Science chamber, p_1 being the pressure in the MOT chamber, S being the pump rate of the ion pump in the Science region and C being the conductance in molecular flow through the differential pumping tube which connects the two chambers [93]. The molecular flow C through the differential pumping tube can be estimated by assuming the tube to be a pinhole which results in

$$C_{\text{pinhole}} = \frac{1}{4}\sqrt{\frac{8 \cdot k_{\text{B}} \cdot T}{\pi m_{\text{Rb}}}} \cdot A\,, \tag{C.2}$$

with $A = \pi \cdot r^2$ being the cross section of the tube, T being the temperature of the background gas, m_{Rb} being the Rubidium mass and $d = 2r = 4\,\text{mm}$ being the diameter [94]. Next, one can estimate

the flow through a tube which is given by

$$C_{\text{tube}} = \frac{4}{3} \cdot \frac{d}{l}\,, \tag{C.3}$$

with $l = 105.3\,\text{mm}$ being the length of the tube [92]. When combining Eq. (C.2) and Eq. (C.3), one can determine the flow to be

$$\begin{aligned} C &= C_{\text{pinhole}} \cdot C_{\text{tube}} \\ &= \frac{\pi}{12}\frac{d^3}{l} \cdot \sqrt{\frac{8 \cdot k_{\text{B}} \cdot T}{\pi \cdot m_{\text{Rb}}}} \\ &= 0.04\,\text{l/s}\,, \end{aligned} \tag{C.4}$$

with $T = 300\,\text{K}$ being the temperature at room temperature. The pump rate of the ion pump is not stating a specific value for the case of Rubidium [95], but for H_2 the pump rate is 500 l/s and for N_2 it is 200 l/s and using these values as bounds one can estimate the minimal pressure achievable in the Science chamber depending on the pressure in the MOT chamber. By using these values given for S together with Eq. (C.4) and insert it into Eq. (C.1), it is possible to determine the pressure that can be achieved in the Science chamber for a given pressure in the MOT chamber:

$$\begin{aligned} p_2 &= \frac{p_1 \cdot C}{S + C} \\ &= \begin{cases} 2.0 \cdot 10^{-4} \cdot p_1 & , \quad \text{N}_2 \\ 8.0 \cdot 10^{-5} \cdot p_1 & , \quad \text{H}_2 \end{cases} . \end{aligned} \tag{C.5}$$

This is the ratio one would expect to achieve for a set pressure in the MOT chamber.

C.2 Estimated pressure in the two chambers

In this section, the pressure in the MOT chamber and in the Science chamber is determined by performing a lifetime measurement of the atoms in the respective trap.

First, one is having a look at the lifetime of the atoms in the MOT magnetic trap. To do so, the holding time of the atoms in the magnetic trap is scanned and then an absorption image is taken for different times. This results in a reduction of atoms over time. Since the MOT loading time, described by Eq. (3.9) in more detail, which is discussed in Section 3.3.2, coincides with the trap lifetime, both can be described with an exponential as discussed by Moore et al. [55]. By fitting an exponential to that curve, it is possible to determine the life time of the atoms in the trap. This can be seen in Fig. C.1(a) where the lifetime in the MOT chamber can be found to be $\tau = (2.62 \pm 0.02)\,\text{s}$.

Using this result it is possible to make a rough estimation of the background pressure in the chamber. For this, the following rate equation can be found to be [55]

$$\frac{dN(t)}{dt} = \alpha P_{\text{Rb}} - (\beta P_{\text{Rb}} + \gamma) N(t)\,,$$

with αP_{Rb} describing the trapping cross section with P_{Rb} being the partial Rubidium pressure, $\beta N(t)$

describes the losses due to collisions with background gas and $\gamma N(t)$ describe other losses such as laser light shining onto the atoms, noise of the magnetic fields or Majorana spin-flips [96]. Since the mechanical shutters are in place, laser light is prohibited from hitting the atoms when they are in the trap. Also, the magnetic coils used have a high inductance and little noise. Furthermore, the temperature of the atoms is at the order of 200 µK and with this Majorana spin-flips should not lead to large atom loss [97]. In this case, we neglect all terms except for the contribution of collisions with Rubidium atoms from background pressure. This then results in

$$\begin{aligned} \frac{dN(t)}{dt} &= -\beta P_{\mathrm{Rb}} \cdot N(t) \\ \Rightarrow \tau &= \frac{1}{\beta \cdot P_{\mathrm{Rb}}} \\ \Leftrightarrow P_{\mathrm{Rb}} &= \frac{1}{\beta\tau} \,. \end{aligned} \tag{C.6}$$

Since not much is known about the composition of the background gas, upper and lower bounds (hydrogen and nitrogen) are used to achieve a rough estimation. In the case of H_2 one can find $\beta = 4.9 \cdot 10^7 \mathrm{Torr}^{-1}\mathrm{s}^{-1}$ and for N_2 one can find $\beta = 2.6 \cdot 10^7 \mathrm{Torr}^{-1}\mathrm{s}^{-1}$ [98]. By inserting this together with the found lifetime of 2.66 s one can find the pressure to be in the order of 10^{-8} mbar up to 10^{-9} mbar.

As discussed in Appendix C.1, one would expect the pressure to be much better in the Science chamber compared to the MOT chamber. This is looked at in more detail in the following in Fig. C.1(b). The number of atoms is again measured as a function of the holding time of the atoms in the final trap. By fitting an exponential function, one can determine the lifetime of the atoms. This gives a lifetime of $\tau = (4.80 \pm 0.13)$s, which is almost a factor of two longer than the lifetime in the MOT chamber of $\tau = (2.62 \pm 0.02)$s. Here, the fit range was chosen such that it only starts after 4 s as this is the time when the sloshing almost vanished.

Using these lifetimes, one can again calculate upper and lower bounds for the expected background pressure with Eq. (C.6) to be 10^{-9} mbar. From this one can see that the improvement is not as significant as one would expect from Appendix C.1. This can be explained by the fact that so far, the glass cell for the Science chamber was not baked out yet in order to minimize its stress before using it in the cryostat.

Baking out the system will reduce the background pressure further and consequently minimize collisions with the background gas. This will thus lead to an increased lifetime of the atoms in the trap. It is also expected that working at cryogenic temperatures alone will further improve the vacuum, leading to an even longer lifetime of the atoms.

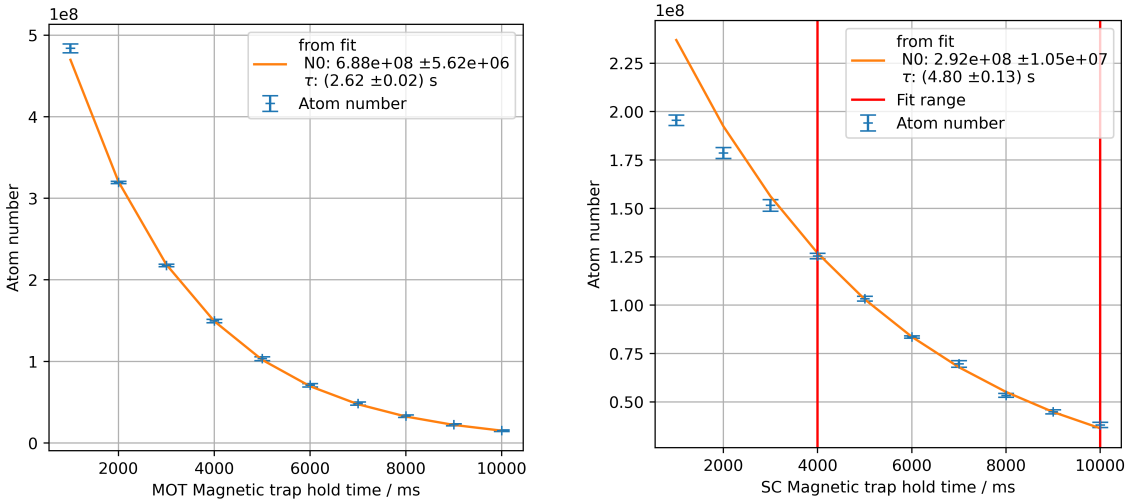

(a) (b)

Figure C.1: Atom number as a function of holding time in the magnetic trap to determine the trap life time in the MOT chamber **(a)** and in the Science chamber **(b)** averaged over five measurement cycles each. This is then fitted with an exponential decay to be able to extract the trap life time which can be found to be $\tau = (2.62 \pm 0.02)$ s for the MOT chamber and $\tau = (4.80 \pm 0.13)$ s in the Science chamber.

Bibliography

[1] A. G. J. MacFarlane, J. P. Dowling and G. J. Milburn,
Quantum technology: the second quantum revolution,
Philosophical Transactions of the Royal Society of London. Series A: Mathematical, Physical and Engineering Sciences **361** (2003) 1655,
eprint: https://royalsocietypublishing.org/doi/pdf/10.1098/rsta.2003.1227.

[2] A. Ajagekar, T. Humble and F. You, *Quantum computing based hybrid solution strategies for large-scale discrete-continuous optimization problems*,
Computers & Chemical Engineering **132** (2020) 106630.

[3] J. Biamonte et al., *Quantum machine learning*, Nature **549** (2017) 195.

[4] S. Pirandola et al., *Advances in quantum cryptography*, Adv. Opt. Photon. **12** (2020) 1012.

[5] F. Grasselli, *Quantum Cryptography: From Key Distribution to Conference Key Agreement*,
Quantum Science and Technology, Springer International Publishing, 2021,
ISBN: 9783030643607.

[6] G. Kurizki et al., *Quantum technologies with hybrid systems*,
Proceedings of the National Academy of Sciences **112** (2015) 3866,
eprint: https://www.pnas.org/doi/pdf/10.1073/pnas.1419326112.

[7] J. Preskill, *Quantum computing 40 years later*, 2023, arXiv: 2106.10522 [quant-ph].

[8] J. M. Gambetta, J. M. Chow and M. Steffen,
Building logical qubits in a superconducting quantum computing system,
npj Quantum Information **3** (2017).

[9] C. S. Adams, J. D. Pritchard and J. P. Shaffer, *Rydberg atom quantum technologies*,
Journal of Physics B: Atomic, Molecular and Optical Physics **53** (2019) 012002.

[10] M. Saffman, T. G. Walker and K. Mølmer, *Quantum information with Rydberg atoms*,
Rev. Mod. Phys. **82** (3 2010) 2313.

[11] F. Arute et al., *Quantum supremacy using a programmable superconducting processor*,
Nature **574** (2019) 505.

[12] C. Hufnagel, A. Landra, L. C. Chean, D. Yu and R. Dumke,
"Superconducting atom chips: towards quantum hybridization", *Quantum Photonic Devices*,
ed. by C. Soci, M. Agio and K. Srinivasan, vol. 10358,
International Society for Optics and Photonics, SPIE, 2017 103580D.

[13] S. Kotler, R. W. Simmonds, D. Leibfried and D. J. Wineland,
Hybrid quantum systems with trapped charged particles, Phys. Rev. A **95** (2 2017) 022327.

[14] Z.-L. Xiang, S. Ashhab, J. Q. You and F. Nori,
Hybrid quantum circuits: Superconducting circuits interacting with other quantum systems,
Rev. Mod. Phys. **85** (2 2013) 623.

[15] A. Clerk, K. Lehnert, P. Bertet, J. Petta and Y. Nakamura,
Hybrid quantum systems with circuit quantum electrodynamics, English (US),
Nature Physics **16** (2020) 257, Publisher Copyright: © 2020, Springer Nature Limited.

[16] D. Petrosyan, K. Mølmer, J. Fortágh and M. Saffman,
Microwave to optical conversion with atoms on a superconducting chip,
New Journal of Physics **21** (2019) 073033.

[17] M. Forsch et al., *Microwave-to-optics conversion using a mechanical oscillator in its quantum ground state*, English, Nature Physics **16** (2020) 69, Publisher Copyright: © 2019, The Author(s), under exclusive licence to Springer Nature Limited.

[18] S. Barzanjeh, M. Abdi, G. J. Milburn, P. Tombesi and D. Vitali,
Reversible Optical-to-Microwave Quantum Interface, Physical Review Letters **109** (2012).

[19] M. J. Weaver et al.,
An integrated microwave-to-optics interface for scalable quantum computing,
Nature Nanotechnology **19** (2023) 166.

[20] M. Gao, Y.-x. Liu and X.-B. Wang,
Coupling Rydberg atoms to superconducting qubits via nanomechanical resonator,
Phys. Rev. A **83** (2 2011) 022309.

[21] A. Blais, A. M. van den Brink and A. M. Zagoskin,
Tunable Coupling of Superconducting Qubits, Phys. Rev. Lett. **90** (12 2003) 127901.

[22] R. Löw et al., *An experimental and theoretical guide to strongly interacting Rydberg gases*,
Journal of Physics B: Atomic, Molecular and Optical Physics **45** (2012) 113001.

[23] T. F. Gallagher, *Rydberg atoms*, Reports on Progress in Physics **51** (1988) 143.

[24] S. D. Hogan et al.,
Driving Rydberg-Rydberg Transitions from a Coplanar Microwave Waveguide,
Phys. Rev. Lett. **108** (6 2012) 063004.

[25] D. M. Walker, L. L. Brown and S. D. Hogan,
Electrometry of a single resonator mode at a Rydberg-atom–superconducting-circuit interface,
Phys. Rev. A **105** (2 2022) 022626.

[26] M. Saffman and K. Mølmer, *Scaling the neutral-atom Rydberg gate quantum computer by collective encoding in holmium atoms*, Phys. Rev. A **78** (1 2008) 012336.

[27] S. J. Evered et al., *High-fidelity parallel entangling gates on a neutral-atom quantum computer*,
Nature **622** (2023) 268.

[28] S. de Léséleuc, D. Barredo, V. Lienhard, A. Browaeys and T. Lahaye,
Optical Control of the Resonant Dipole-Dipole Interaction between Rydberg Atoms,
Phys. Rev. Lett. **119** (5 2017) 053202.

[29] A. N. Cleland and M. R. Geller,
Superconducting Qubit Storage and Entanglement with Nanomechanical Resonators,
Phys. Rev. Lett. **93** (7 2004) 070501.

[30] Y. Chu et al., *Quantum acoustics with superconducting qubits*, Science **358** (2017) 199, eprint: https://www.science.org/doi/pdf/10.1126/science.aao1511.

[31] L. Sadowski, *Design of a superconducting atom chip for interfacing Rydberg atoms with microwave resonators*, Master's Thesis: University Bonn, 2024.

[32] D. Petrosyan, J. Otterbach and M. Fleischhauer, *Electromagnetically Induced Transparency with Rydberg Atoms*, Phys. Rev. Lett. **107** (21 2011) 213601.

[33] M. Fleischhauer, A. Imamoglu and J. P. Marangos, *Electromagnetically induced transparency: Optics in coherent media*, Rev. Mod. Phys. **77** (2 2005) 633.

[34] M. Greiner, I. Bloch, T. W. Hänsch and T. Esslinger, *Magnetic transport of trapped cold atoms over a large distance*, Phys. Rev. A **63** (3 2001) 031401.

[35] J. Popp, *Construction and Preparation of an Experimental Setup for Excitation and Detection of Rydberg Atoms in a Cryogenic Environment*, Master's Thesis: University Bonn, 2024.

[36] E. D. Black, *An introduction to Pound-Drever-Hall laser frequency stabilization*, Am. J. Phys. **69** (2000) 79.

[37] R. W. P. Drever, *Laser Phase and Frequency Stabilization Using an Optical Resonator*, Appl. Phys. B **31** (1983) 97.

[38] V. Mauth, *Realization of a 87Rb magneto-optical trap*, Bachelor's Thesis: University Bonn, 2023.

[39] J. Gamper, *Frequenzstabilisierung zur Laserkühlung von Rubidium*, Bachelor's Thesis: University Bonn, 2022.

[40] S. Germer, *Frequency stabilization of a laser and a high resolution optical setup for excitation of ultracold Rydberg atoms*, Bachelor's Thesis: University Bonn, 2023.

[41] D. A. Steck, *Rubidium 85 D Line Data*, 2021, URL: http://steck.us/alkalidata (visited on 25/08/2024).

[42] D. A. Steck, *Rubidium 87 D Line Data*, 2021, URL: http://steck.us/alkalidata (visited on 25/08/2024).

[43] S. L. Cornish, N. R. Claussen, J. L. Roberts, E. A. Cornell and C. E. Wieman, *Stable* ^{85}Rb *Bose-Einstein Condensates with Widely Tunable Interactions*, Phys. Rev. Lett. **85** (9 2000) 1795.

[44] A. Banerjee, D. Das and V. Natarajan, *Precise fine-structure and hyperfine-structure measurements in Rb*, 2002, arXiv: physics/0209019 [physics.atom-ph].

[45] H. Busche, *Efficient loading of a magneto-optical trap for experiments with dense ultracold Rydberg gases*, University Heidelberg, 2011.

[46] P. Rakitzis, *Diffractive Dark-Ground Imaging of Ultra-Low Atom-Numbers in a MOT*, University of Crete, 2011.

[47] T. Pyragius, *Developing and building an absorption imaging system for Ultracold Atoms*, 2012, arXiv: 1209.3408 [physics.ins-det].

[48] S. Roof, K. Kemp, M. Havey, I. M. Sokolov and D. V. Kupriyanov, *Microscopic lensing by a dense, cold atomic sample*, Opt. Lett. **40** (2015) 1137.

[49] W. Demtröder, *Laser Spectroscopy, Vol. 2 Experimental Techniques*, 4th ed., Springer, 2008, ISBN: 978-3-540-74952-3.

[50] C. Foot, *Atomic physics*, Oxford University Press, USA, 2005.

[51] H. Metcalf and P. van der Straten, *Laser Cooling and Trapping*, Journal of the Optical Society of America B **20** (2003).

[52] K. Kowalski et al., *Magneto-optical Trap: Fundamentals and Realization*, Computational Methods in Science and Technology **Special Issue** (2010) 115.

[53] E. L. Raab, M. Prentiss, A. Cable, S. Chu and D. E. Pritchard, *Trapping of Neutral Sodium Atoms with Radiation Pressure*, Phys. Rev. Lett. **59** (23 1987) 2631.

[54] W. Demtröder, *Experimentalphysik 2: Elektrizität und Optik*, Springer-Lehrbuch, Springer Berlin Heidelberg, 2013, ISBN: 9783642299438.

[55] R. W. G. Moore et al., *Measurement of vacuum pressure with a magneto-optical trap: A pressure-rise method*, Review of Scientific Instruments **86** (2015).

[56] H. J. Metcalf and P. V. der Straten, *Laser Cooling and Trapping*, Springer Science and Business Media, 1999, 1999, ISBN: 9780387987477.

[57] P. McNAMEE, S. J. and F. CHILTON, *Tables of Clebsch-Gordan Coefficients of* SU_3, Rev. Mod. Phys. **36** (4 1964) 1005.

[58] J. Dalibard and C. Cohen-Tannoudji, *Laser cooling below the Doppler limit by polarization gradients: simple theoretical models*, J. Opt. Soc. Am. B **6** (1989) 2023.

[59] M. S. Yoon, *Experiments On Magnetic Transport, Magnetic Trapping, And Bose-Einstein Condensation*, PhD Thesis: The Queen's College University of Oxford, 2009.

[60] W. HAPPER, *Optical Pumping*, Rev. Mod. Phys. **44** (2 1972) 169.

[61] Hantek, 2020, URL: https://hantek.com/products/detail/77 (visited on 20/10/2024).

[62] T. Instruments, *DRV425 Evaluation Module*, 2020, URL: https://www.ti.com/lit/ug/slou410b/slou410b.pdf?HQS=dis-mous-null-mousermode-dsf-pf-null-wwe&ts=1729431870753&ref_url=https%253A%252F%252Feu.mouser.com%252F (visited on 20/10/2024).

[63] T. Klostermann et al., *Fast long-distance transport of cold cesium atoms*, Phys. Rev. A **105** (4 2022) 043319.

[64] R. Grimm, M. Weidemüller and Y. B. Ovchinnikov, *Optical Dipole Traps for Neutral Atoms*, Advances in Atomic Molecular and Optical Physics **42** (2000) 95, arXiv: physics/9902072 [physics.atom-ph].

[65] T. Badr et al., *Comparison of time profiles for the magnetic transport of cold atoms*, Applied Physics B **125** (2019).

[66] N. Šibalić, J. Pritchard, C. Adams and K. Weatherill, *ARC: An open-source library for calculating properties of alkali Rydberg atoms*, Computer Physics Communications **220** (2017) 319.

[67] E. Urban et al., *Observation of Rydberg blockade between two atoms*, Nature Physics **5** (2009) 110.

[68] J. Kumlin et al., *Quantum optics with Rydberg superatoms*, Journal of Physics Communications **7** (2023) 052001.

[69] V. Leu, *A Glued Ultra-High Vacuum Cell Using Titanium and Fused Silica and a High Resolution Optical Setup for Ultracold Atom Experiments*, Bachelor's Thesis: University Bonn, 2023.

[70] F. Engel, *Entwicklung eines FPGA basierten Pulsgenerators mit Nanosekunden-Aufl ¨osung f ¨ur schnelle Rydberg-Experimente*, Bachelor's Thesis: Universit ¨at Stuttgart, 2013.

[71] A. Paris-Mandoki et al., *Free-Space Quantum Electrodynamics with a Single Rydberg Superatom*, Phys. Rev. X **7** (4 2017) 041010.

[72] *Swabian Instruments Time Tagger User Manual, Release 2.17.4.0*, 2024, URL: https://www.swabianinstruments.com/static/downloads/TimeTagger_User_Manual.pdf (visited on 09/09/2024).

[73] *Swabian Instruments Time Tagger User Manual Measurement classes, TimeDifferences*, 2024, URL: https://www.swabianinstruments.com/static/documentation/TimeTagger/api/Measurements.html#timedifferences (visited on 18/10/2024).

[74] M. D. Lukin et al., *Dipole Blockade and Quantum Information Processing in Mesoscopic Atomic Ensembles*, Phys. Rev. Lett. **87** (3 2001) 037901.

[75] O. Firstenberg, C. S. Adams and S. Hofferberth, *Nonlinear quantum optics mediated by Rydberg interactions*, Journal of Physics B: Atomic, Molecular and Optical Physics **49** (2016) 152003.

[76] L. Components, *Single-photon avalanche diodes*, URL: https://www.lasercomponents.com/fileadmin/gatedcontent/publications/single-photon-avalanche-diodes.pdf (visited on 13/09/2024).

[77] *Laser Components*, 2024, URL: https://www.lasercomponents.com/de/ (visited on 11/09/2024).

[78] *Single Photon Counting Module COUNT®-Series*, URL: https://www.lasercomponents.com/fileadmin/user_upload/home/Datasheets/lc-photon-counter/count-series.pdf (visited on 25/10/2024).

[79] D. Steck, *Quantum and Atom Optics*, 2007.

[80] C. Genes, *Quantum Physics of Light-Matter Interactions, FAU - Summer semester 2019*, URL: https://mpl.mpg.de/fileadmin/user_upload/LectureNotes.pdf (visited on 10/10/2024).

[81] M. O. Scully and M. S. Zubairy, *Quantum Optics*, Cambridge University Press, 1997.

[82] J. Johansson, P. Nation and F. Nori,
QuTiP: An open-source Python framework for the dynamics of open quantum systems,
Computer Physics Communications **183** (2012) 1760.

[83] J. Johansson, P. Nation and F. Nori,
QuTiP 2: A Python framework for the dynamics of open quantum systems,
Computer Physics Communications **184** (2013) 1234.

[84] J. Pérez-Ríos and A. S. Sanz, *How does a magnetic trap work?*,
American Journal of Physics **81** (2013) 836.

[85] B. W. Shore and P. L. Knight, *The Jaynes-Cummings Model*,
Journal of Modern Optics **40** (1993) 1195,
eprint: https://doi.org/10.1080/09500349314551321.

[86] C. Tresp,
Rydberg polaritons and Rydberg superatoms - Novel tools for quantum nonlinear optics,
PhD Thesis: University of Stuttgart, 2017.

[87] J. Schmidt, *Generation of non-classical light using ultra-cold Rydberg ensembles*,
Master Thesis: University of Stuttgart, 2014.

[88] I. I. Beterov, D. B. Tretyakov, I. I. Ryabtsev, A. Ekers and N. N. Bezuglov,
Ionization of sodium and rubidium Rydberg atoms by blackbody radiation,
Physical Review A **75** (2007).

[89] M. Mack et al., *Measurement of absolute transition frequencies of* ^{87}Rb *to nS and nD Rydberg states by means of electromagnetically induced transparency*,
Phys. Rev. A **83** (5 2011) 052515.

[90] H. Gorniaczyk et al., *Enhancement of Rydberg-mediated single-photon nonlinearities by electrically tuned Förster resonances*, Nature Communications **7** (2016).

[91] M. Lukin, *Modern Atomic and Optical Physics II (Physics 285b)*,
URL: https://lukin.physics.harvard.edu/files/lukin/files/physics_285b_lecture_notes.pdf (visited on 23/09/2024).

[92] 2. P. V. GmbH, *Pfeiffer Vacuum, 1.2.8 Leitwert*,
URL: https://know-how-book.pfeiffer-vacuum.com/de/einfuehrung-in-die-vakuumtechnik/grundlagen/leitwert/index.html (visited on 04/10/2024).

[93] J. Macher, A. Hausberger, A. E. Macher, M. Morak and B. Schrittesser, *Critical review of models for H2-permeation through polymers with focus on the differential pressure method*,
International Journal of Hydrogen Energy **46** (2021) 22574.

[94] K. Jousten, *Handbuch Vakuumtechnik*, 12th ed.,
Springer Fachmedien Wiesbaden GmbH, 2018.

[95] NEXTorr, *NEXTorr Z 200*,
URL: https://www.ferrovac.com/?tool=SysFileFetch&file=CAPACITorrZ200.pdf
(visited on 21/10/2024).

[96] D. M. Brink and C. V. Sukumar, *Majorana spin-flip transitions in a magnetic trap*,
Physical Review A **74** (2006).

[97] V. Gomer et al., *Magnetostatic traps for charged and neutral particles*,
Hyperfine Interact. **109** (1997) 281.

[98] T. Arpornthip, C. A. Sackett and K. J. Hughes,
Vacuum-pressure measurement using a magneto-optical trap,
Phys. Rev. A **85** (3 2012) 033420.

Acknowledgements

I would like to take this opportunity to thank all those who supported me during my master thesis, both professionally and personally. Without you I would not be where I am today.

Sebastian Hofferberth, thank you for the amazing opportunity to be part of such an incredible research group for quite some time now. Thank you for your guidance, support and interesting discussions. I have learnt so much in the past year, which I am extremely grateful for. Thank you so much!

Thank you Daqing Wang for being my second supervisor and with this making this thesis possible.

I would also like to thank my HQO-family, making everyday life such a pleasurable and fun experience. Cedric Wind, thank you for great supervision, support and an amazing time working together in the experiment. I learned so much from you, let it be physics or "Things you should really have seen in life" and it was fun all the way through. Thanks that no matter how stressful things got, I always knew I could count on your support. I would also like to thank Hannes Busche, who is not only an excellent physicist but also amazing to work with. Thank you for countless explanations and fun discussions. Wolfgang Alt, thank you for all your expertise and your tips and tricks that make lab life easier. And thank you for all your time, even though you are always there for all labs. Valerie Mauth, thank you so much for making the last month of being in the lab an amazing time. Even though everything had to work fast, together we made it work and it was fun. Thank you for all the emotional support, the great walks talking about life and physics and just an amazing time. I also want to thank Valerie Leu for not just being an amazing company on the way to uni (I really enjoy going to uni together with you) but just amazing company in general. Thank you for a great time. Sam Germer, with your calm and friendly manner, you know how to de-stress a stressful situation which I was especially grateful for during the last weeks of writing. Also, thank you for always jumping in, when help is needed. Leon Sadowski, thank you for all the fun discussions about medicine that brought a lot of fresh air into the physics world. Thanks also for all the support and help throughout this year. I am super grateful for that. Johanna Popp, thank you for a nice time together in the lab at the beginning of my master thesis, talking about our passion for good books. Aylin Cansiz and Max Reicherd, thanks for nice joined coffee breaks and interesting discussions about physics.

Another big thanks to my RQO-fairies, always helping out and being there when needed or just to have a fun time. Nina Stiesdal, thank you so much for being such a kind and caring person and always helping out when needed - you really are amazing. Thank you so much for all your kind words and all your support. Thank you, Lukas Ahlheit for always making time for questions and no matter how

complex a question is, you manage to answer it in a way that everyone can understand, which I really appreciate. Daniil Svirskiy, thank you for nice conversations about physics, culture and languages which are always fun and make the day better. Jan de Haan, thank you for all the motivating coffee/tea breaks together, especially on the final weekends. Also, thank you for all the coding-related support and for always organizing our theatre-trips which are amazing. Also, thanks to Simon Schroers for dropping by the lab and office occasionally just to say "Hi", which always cheers me up. Theresa Dewey, Hannah Buss and Kimberly Kurzbach, thank you so much for your amazing woman power. May it be presenting our labs to students, taking a nice and long walk or enjoying the time over a nice cup of coffee - you know how to make my day - thank you! Thanks to Matthias Metternich, Chris Nowaczek and Jeremy Binda for nice and interesting discussions which felt good when I was looking for something else in the RQO lab in the first place.

Thanks to my FCO-buddies for a lot of fun when being around. Lukas Tenbrake, Florian Giefer, Jana Blechmann, thank you all for not only fun facts about fibers and optomechanics but also for all the great movie-nights, cologne trips and gossip. Also, Benedikt Beck and Johanna Stein, thanks for nice conversations and insights into the fun world of fiber-optomechanics.

Also, thanks to my YQO-mates for all the great times. Eduardo Urunuela, thank you for providing a good working atmosphere with a delicious coffee and being a great colleague. Wang Xin, thank you for all the evenings we spent together over my seminar paper. Also, thank you for your great advice when it comes to seeing weird features in transmission spectra. Thank you, Ludwig Müller for organizing nice group evenings and having a great time over a nice coffee. Also, thanks to Tangi Legrand for short-notice help when it comes to understanding certain formulas used for evaluation. Florian Pausewang, thanks for nice conversations and coffee breaks talking about the good old HQO-times. Knut Domke, Konrad Beck, and Clara Witte, thanks for a nice time.

Thanks also to the kindest and most supportive administrative team. Tina Naggert, thank you for your casual, kind words and your encouragement, which always make me very happy. Dietmar Haubrich, thanks for all the support with paperwork - I would be lost without you.

Without mentioning any names, I would also like to thank all my amazing friends (that I have not explicitly mentioned above) all over the world. A special thank you to my Board game group, our weekly mensa meet-up round, my zoom-friends and my friends back in Austria - Thank you so much! Thanks to my parents for all the support and always being there for me, might it be an amazing breakfast via zoom or an hour-long phone call. My sister always knows which strings to pull to cheer me up and motivate me - thank you! And thank you Daniel, for always being there for me.